



The  
University  
Of  
Sheffield.

Department  
Of  
Mechanical  
Engineering

PhD Mechanical Engineering

Thesis

**Surface defect evolution analysis  
in high silicon steels during hot  
rolling processes: experimental  
and numerical simulation**

Thesis submitted for the Degree of Doctor of Philosophy

May 2017

**Manuel Nioi**



## **SUMMARY**

Experimental and numerical approaches were used in the current research to investigate the evolution of superficial defects that develop on slabs of High Silicon content during the first stand of hot rolling processes. Understanding the deformation mechanisms of the initial surface features is essential for the prevention of critical defect formation on final products.

Hot rolling experiments were carried out to determine the evolution of superficial cavities when the slabs are subjected to hot rolling. In addition, descaling experiments and hot ring compression tests were carried out to identify the friction coefficient present during the process. A model reproducing the hot rolling experiment was produced and a multilevel modelling approach was used to refine the mesh in the defects zone. The predictions are found in good agreement with the experiments.

The results obtained from hot rolling experiments indicated the buckling of the lateral sides of the cavity to be the main cause of oxide entrapment and consequent defect formation. This is because the oxide inclusions beneath flaps of metal are most likely to resurface during successive slab thickness reductions appearing as surface defects. Experiments demonstrated the importance of depth to width aspect ratio of the initial surface features on the severity of the final defect. With regards to friction, isothermal ring tests demonstrate that friction coefficient increases with temperature and decreases with the thickness of the oxide present on the surface of the slab.

The material models, the contact conditions and the modelling approaches developed are used to reproduce a full scale single rolling stand of a hot rolling process. The full-scale model was used to test the effect of different process parameters on the defects evolution and of different geometries on the deformation mechanisms.

The model developed revealed that the friction is the main process parameter affecting the defect evolution during rolling. Higher friction coefficients facilitate the closure of the defect, increasing the severity of the final features formed.

The geometry of the initial indentation before rolling was identified to be the main parameter which determines its deformation mechanisms. In particular, spherical cavities are easily eliminated during rolling. Conversely, pyramidal and cubical features tend to deform in a more severe way. For a given initial geometry, the initial aspect ratio of the defect was confirmed to play an important role in the final severity. The major limitation of the model was the excessive simplicity of the contact conditions between roll and slab in the defect zone.

Nevertheless, the approaches used to produce the models can be extended to predict the deformation of different initial features presents on the surface of slab subjected to hot rolling processes and to reproduce the behaviour of defects for multistand rolling procedures.

## **ACKNOWLEDGMENTS**

I would like to express my deep gratitude to Dr. Ghadbeigi and Dr. Pinna for their valuable and constructive suggestions during the development of this research work. I would also like to offer my special thanks to Dr. Celotto and Dr. Swart from Tata Steel Europe, for their precious advice and assistance at first in the planning stage, then during the interpretation of the experimental and numerical results.

I am particularly grateful for the suggestions given by Dr. Farrugia during the designing of the modelling approach and descaling experiments conducted.

Finally, I wish to thank my family for their support and encouragement throughout my study.



# CONTENTS

<i>Summary</i>	<i>i</i>
<i>Acknowledgments</i>	<i>iii</i>
<i>Contents</i>	<i>1</i>
<i>Nomenclature</i>	<i>4</i>
<i>Table of figures</i>	<i>6</i>
<b>1 INTRODUCTION</b>	<b>15</b>
1.1 Problem description	15
1.2 Purpose of the research	17
<b>2 LITERATURE REVIEW</b>	<b>19</b>
2.1 Electrical steels	19
2.2 The hot rolling process	19
2.2.1 Types of defects in hot rolling processes	21
2.2.2 Previous experimental research	22
2.3 Numerical modelling of hot rolling operations	24
2.3.1 Material models for high temperature and high strain rates deformation	25
2.3.2 Geometric modelling of the defects in hot rolling processes	28
2.3.3 Heat transfer and friction conditions modelling of hot rolling process.	33
2.4 Measurements of friction coefficient	34
2.5 Oxide scales in electrical steels	36
2.6 Water spray descaling in hot rolling processes	40
2.7 Summary	43
<b>3 EXPERIMENTAL APPROACH</b>	<b>45</b>
3.1 Hot rolling of samples with artificial defects	46
3.2 Descaling	55
3.3 Isothermal hot ring compression	60
3.4 Summary	64

<b>4</b>	<b>EXPERIMENTAL RESULTS</b>	<b>65</b>
4.1	Analysis of deformed defects geometries	65
4.2	Crevice formation behaviour	71
4.3	Deformation severity analysis: side wall buckling	74
4.4	Deformation severity analysis: defect area reduction	76
4.5	Longitudinal displacement measurement	78
4.6	Quantification of longitudinal displacements	80
4.7	Analysis of oxide layer thickness due to the descaling process	82
4.8	Isothermal hot ring compression experiment results	86
4.8.1	Heat treatment of the rings	86
4.8.2	Ring compression test	87
4.9	Summary	90
<b>5</b>	<b>FE MODELLING APPROACH</b>	<b>92</b>
5.1	Developing a constitutive equation for Fe-3% Si steel	92
5.2	Loads, contact interactions and boundary conditions of the model	93
5.3	Geometry, mesh and Multilevel approach	96
5.3.1	Macroscale model	97
5.3.2	Mesoscale model	98
5.4	Material model and strain patterns calibration of the laboratory model	101
5.4.1	Material model	101
5.4.2	Macroscale model calibration of the strain pattern	107
5.5	Macroscale model results	110
5.6	Mesoscale results	111
5.6.1	Mesoscale model quality check	111
5.7	Defect behaviour during rolling	112
5.7.1	Mesh dependence study	117
5.7.2	Validation	118
5.8	Isothermal hot ring compression test: Temperature dependence of friction for a real scale hot rolling process	123



<b>6</b>	<b>HOT ROLLING PROCESS MODEL</b>	<b>128</b>
6.1	<b>Methodology</b>	<b>129</b>
6.1.1	Material model	129
6.1.2	Loads, contact interactions and boundary condition	129
6.1.3	Macroscale hot rolling model	130
6.1.4	Mesoscale hot rolling model	132
6.2	<b>Process parameters study</b>	<b>133</b>
6.2.1	Results	133
6.3	<b>Geometrical study</b>	<b>135</b>
6.3.1	Results	136
<b>7</b>	<b>DISCUSSION</b>	<b>141</b>
7.1	<b>Experimental discussions</b>	<b>141</b>
7.1.1	Defect evolution during rolling discussion	141
7.1.2	Slab distortion dependence on oxide thickness	149
7.1.3	Oxide scale characterization after descaling	151
7.1.4	Temperature dependence of friction	152
7.2	<b>Numerical discussions</b>	<b>156</b>
<b>8</b>	<b>Conclusions and future work</b>	<b>162</b>
<b>9</b>	<b>References</b>	<b>165</b>

## NOMENCLATURE

$\dot{\epsilon}^{pl}$	Plastic strain rate vector ( $s^{-1}$ )
$\theta_{AMB}$	Average surface temperature ( $K$ )
$\theta_{AVG}$	Ambient temperature ( $K$ )
$\theta_a$	Temperature point a ( $K$ )
$\theta_b$	Temperature point b ( $K$ )
$\theta^z$	Absolute zero temperature ( $K$ )
$q_s$	Heat generated by friction ( $kJ$ )
$r^{pl}$	Heat generated per unit of volume due to plastic deformation
$\dot{\gamma}$	Slip rate ( $s^{-1}$ )
$\dot{\epsilon}$	Strain rate ( $s^{-1}$ )
$\sigma_{S-B}$	Stefan-Boltzmann constant
$\sigma_s$	Ultimate tensile stress ( $MPa$ )
$\tau_c$	critical shear stress! ( $MPa$ )
$\tau_{lim}$	Shear limit ( $MPa$ )
$\Delta H$	Activation energy for plastic deformation ( $\frac{kJ}{mol}$ )
$k$	Gap conductance ( $\frac{kW}{m^2 \cdot K}$ )
$q$	Computed heat flux ( $\frac{kW}{m^2}$ )

$\alpha$	Material constant ( $MPa^{-1}$ )
$A$	Material constant ( $s^{-1}$ )
$Pfr$	Rate of frictional energy dissipation
$Q$	Hardening constant ( $MPa$ )
$R$	Universal gas constant ( $\frac{kJ}{mol \cdot K}$ )
$T$	Temperature ( $K$ )
$b$	Hardening constant
$f$	Fraction of converted heat distributed in the surface
$p$	Surface pressure ( $MPa$ )
$\varepsilon$	Strain
$\varepsilon_i$	Emissivity of the surface
$\eta_p$	Fraction of plastic work converted to heat
$\eta_f$	Fraction of frictional work converted into heat
$\mu$	Friction coefficient ( $MPa$ )
$\sigma$	Stress level ( $MPa$ )
$\tau$	Frictional stress ( $MPa$ )
$\sigma$	Stress vector ( $MPa$ )

## TABLE OF FIGURES

Figure 1.1: Graphical abstract of the work.....	18
Figure 2.1: Schematic of the hot rolling process, defects slab before (A), after the rolling (B), and first rolling stand (C). .....	19
Figure 2.2: Bottom surface quality after the tunnel furnace (TATA steel images). .....	20
Figure 2.3: Type of defects encountered in the slab after rolling: mill shearing defect (a); cross section of a sliver defect (b); lap defect (c); scab defect (d); seam defect (e); scratch defect (f). .....	22
Figure 2.4: Model scheme of slab rolling with a surface crack. [45].....	28
Figure 2.5: Classification of defect generated with width and depth. [37].....	29
Figure 2.6: Shape changes of the surface defects during multi-pass rolling. [37] .....	30
Figure 2.7: Schematic drawing of a process of rolling with an inclusion. [48] .....	31
Figure 2.8: Relationship between the shape, dimension and resistance of the inclusion and the matrix after rolling, the inclusions are in the position of 1/4 of the strip thickness. [48].....	32
Figure 2.9: FeO-SiO <sub>2</sub> phase diagram [92]. .....	37
Figure 2.10: Oxides formed at 1000°C for 2 hours for a silicon steel [15], (a) shows the entire oxide layer, (b) shows an enlargement of the FeO-Fe <sub>2</sub> SiO <sub>4</sub> compound. .....	38
Figure 2.11: Oxides formed at 1250°C for 2 hours for a silicon steel [15]. (a) and (b) show a lower and higher magnification respectively.....	39
Figure 2.12: Oxide scale hardness at 1000 °C after oxidation at 1000°C for different silicon contents [93]. .....	40
Figure 2.13: Typical SWI, IP set-up for different steel composition [97]. .....	41

Figure 2.14: Descaling energy required for C-Mn Steel [96].	42
Figure 2.15: Impingement area scheme [96].	43
Figure 3.1: 3D scan of a transfer bar before the rolling (A), section scheme used to identify the dimension of the slab (B), and the measurement scheme adopted (C).	46
Figure 3.2: Normal distribution of (a) length and (b) width of the defect present in the slab before the rolling process.	47
Figure 3.3: Parameters used to describe the defect geometry	48
Figure 3.4: Machined defects on the surface of slabs before the hot rolling operation. Pins are highlighted in yellow.	50
Figure 3.5: Non defected slab used to measure the strain distortion pattern; pins and front side are highlighted with yellow and red narrows respectively.	51
Figure 3.6: Rolling mill (a) and furnace (b) used for the rolling experiment.	52
Figure 3.7: Transverse and longitudinal section scheme of one defect.	54
Figure 3.8: Slab condition before the test: milled slab (left side), slab containing cylindrical cavities (right side).	56
Figure 3.9: Descaler rig used to carry out the experiment.	57
Figure 3.10: Descaling scheme used for the experiment, 3D view (a), top view (b), and longitudinal section (c).	58
Figure 3.11: Electrical oven (left side) and the box containing argon (right side) used for the heating and cooling of the slabs respectively.	59
Figure 3.12: Sample used for the ring compression test, and sections used to measure diameter variations (indicated in red)	60
Figure 3.13: TMC machine used for the ring tests.	61
Figure 3.14: Heating and compression test timeline scheme used for the experiment.	62

Figure 3.15: Oxide thickness growth rate at different temperatures for 3% Silicon Steel.....	63
Figure 4.1: Typical top and bottom surface of a slab after the rolling. ....	65
Figure 4.2 part 2: Optical photographs of the cavities and deformed defects (highlighted by red rectangles) on the surface of the rolled slabs.....	68
Figure 4.3: Depth and width measurement scheme .....	69
Figure 4.4: Graphical representation of the defects dimensions after rolling for different initial cavities.....	71
Figure 4.5: Micrographs of selected defects B3 (a, e), D3 (b, f), B2 (c, g) and G2 (d, h) showing the deformed geometry at the transversal and longitudinal sections as indicated by the respective arrows.....	73
Figure 4.6: Buckling deformation measurement .....	74
Figure 4.7: Buckling effect measured for different initial depth/ width (D/W) aspect ratio and initial width (W).....	75
Figure 4.8: Final defect depth for different initial depth/width ratios and respective trend line. ....	76
Figure 4.9: Percentage cross-sectional area reduction of the cavities during the rolling for different initial widths and depths and the mean value of length.....	77
Figure 4.10: Percentage cross-sectional area reduction for different initial D/W aspect ratio and initial W.....	78
Figure 4.11: Oxide profile present on the slab surfaces after the rolling for different initial heating temperatures: A, B and C represent the slabs heated at 1200°C, 1150°C and 1100°C respectively (oxide thickness is highlighted with red arrows).....	79
Figure 4.12: Example of a distorted pin after the rolling.....	80
Figure 4.13: Pin measurement scheme after rolling. ....	81
Figure 4.14: Pin distortion pattern for different heating temperature of the slabs .....	81

Figure 4.15: 3% silicon steel slabs after the descaling and cooling, the highlighted regions shows a narrow band with some oxide scales still attached to the surface .....	83
Figure 4.16: Oxide condition before (a) and after the descaling (b, c) for a Fe-3%Si Steel (slab 1).....	84
Figure 4.17: Slabs containing cylindrical holes after the descaling for 2%Si steel and 3 %Si steel.....	85
Figure 4.18: effect of the descaling inside cylindrical holes for a Fe-3%Si steel	86
Figure 4.19: Oxide scale present on the surface of the ring after the heat treatment in different points of the ring.....	87
Figure 4.20: Ring before and after the compression, top view (a) and transversal section (b). .....	88
Figure 4.21: Top view of the ring after the compression for each test conditions applied: rings a,b,c,d,e and f are the rings related to the tests 1, 2, 3, 4, 5 and 6 respectively (test condition are presented in chapter 3.3). .....	89
Figure 4.22: Internal diameter and height reduction ratio measurement of rings for different experimental temperatures.....	90
Figure 5.1: a) Macroscale model, b) element dimension in the contact. ....	98
Figure 5.2: Sub-model and boundary conditions applied.....	100
Figure 5.3: Evolution of the standard deviation of the apparent stress exponent, n, with the variation of $\alpha$ .....	103
Figure 5.4: Experimental data plotted with hyperbolic sine stress law for different temperatures and strain rates.....	104
Figure 5.5: Temperature dependence of saturation stress for different strain rates.....	105
Figure 5.6: Stress dependence of LnZ for different strain rates. ....	105

Figure 5.7: Sellars & Tegart model comparison with the experimental data for different strain rates and temperatures (A, B, C stand for hardening curves obtained at strain rates of  $25 \text{ s}^{-1}$ ,  $10 \text{ s}^{-1}$  and  $1 \text{ s}^{-1}$  respectively).....106

Figure 5.8: Longitudinal displacement comparison between distorted experimental pins, and model mesh run at different friction coefficients..... 108

Figure 5.9: Deformed pin after rolling, longitudinal RD-ND section, a small gap between pin and housing is highlighted in red.....109

Figure 5.10: Roll force comparison between experiments and simulations .....110

Figure 5.11: (a) Temperature ( $^{\circ}\text{K}$ ) and (b) Stress fields (Pa) of the slab in the contact zone.....111

Figure 5.12: Temperature ( $^{\circ}\text{K}$ ) field comparison between a) Macroscale model and b) Mesoscale model; Mises stress (Pa) comparison between c) Macroscale model and d) Mesoscale model, next to the boundary surfaces. ....112

Figure 5.13: Mises stress (Pa) field for the cavities  $C_2$  (a),  $H_2$  (b),  $D_2$  (c) during the rolling.....114

Figure 5.14: Temperature ( $^{\circ}\text{K}$ ) field for the cavities  $C_2$  (a),  $H_2$  (b),  $D_2$  (c) during the rolling. ....114

Figure 5.15: Mises stress (Pa) field longitudinal sections for defects  $C_2$  (a),  $H_2$  (b),  $D_2$  (c), and transversal sections for defects  $C_2$  (d),  $H_2$  (e),  $D_2$  (f). ....115

Figure 5.16: Vertical displacement of a transversal section of the slab containing the defect .....116

Figure 5.17: Vertical displacement field in a longitudinal cross-section of the slab containing a defect during rolling..... 117

Figure 5.18: Defect evolution mesh dependence for different mesh refinement. The letters indicate different mesh refinements..... 117

Figure 5.19: Quantitative mesh dependence analysis.....118

Figure 5.20: Measurement scheme used for a generic defect to estimate the defect dimensions, transversal (left), and longitudinal (right) sections. ....118



Figure 5.21: Comparison between measured and predicted values of (a) final width, (b) final depth and (c) final length, the error of the prediction is indicated with a black cross. ....	119
Figure 5.22: Transversal section of defect C2 comparison between, the initial cavity shape (dashed line), the predicted (red line) and the observed (continuous black line) defects. ....	120
Figure 5.23: C2 defect, longitudinal back section (a) simulated and (b) observed with the microscope; transversal section (c) simulated and (d) observed with the microscope.....	121
Figure 5.24: H1 defect, longitudinal back section (a) simulated and (b) observed with the microscope; transversal section (c) simulated and (d) observed with the microscope.....	122
Figure 5.25: H2 defect, longitudinal back section (a) simulated and (b) observed with the microscope; transversal section (c) simulated and (d) observed with the microscope.....	122
Figure 5.26: D2 defect, transversal section observed with the microscope (a) and simulated (b). ....	123
Figure 5.27: Axisymmetrical model used to reproduce the hot ring compression test. ....	124
Figure 5.28: Friction calibration curves and experimental measurements for an isothermal compression test done at 1050 °C. ....	125
Figure 5.29: Friction calibration curves and experimental measurements for an isothermal compression test done at 950 °C. ....	125
Figure 5.30: Friction calibration curves and experimental measurements for an isothermal compression test done at 850 °C. ....	126
Figure 5.31: Friction coefficient measured at different temperatures. ....	127
Figure 6.1: Hot rolling macroscale model.....	132

Figure 6.2: Hot rolling mesoscale model, (a) boundary surfaces, and (b) submodel detail mesh scheme. .... 133

Figure 6.3 Effect of different friction coefficient on the final transversal section of the defect. .... 134

Figure 6.4 Effect of different reduction ratios on the final transversal section of the defect. .... 135

Figure 6.5 Effect of different slab initial temperatures on the final transversal section of the defect. .... 135

Figure 6.6: Spherical, pyramidal and cuboidal defect cavities before (A), during (B) and after (C) hot rolling. .... 136

Figure 6.7 Pyramidal defects of different aspect ratio before (longitudinal section) and after rolling (whole defect). .... 137

Figure 6.8 Transversal section comparison of pyramidal defects of different initial aspect ratio. .... 138

Figure 6.9 Mesh scheme used to study the effect of different fillet radius on the final defect conformation. .... 139

Figure 6.10 Effect of different fillet radius on the final transversal section of the defect. .... 140

Figure 7.1: Transversal sections of the defects (a) B2 and (b) B3 showing effect of the initial depth on the evolution mechanism. The black dashed line represents the initial cavity shape, the solid line is the final shape after rolling. .... 142

Figure 7.2: Transversal section of the defects D3 (a), and B3 (b). The black dashed line represents the initial defect shape, the continuous line represents the final defect section after the rolling and the red dashed lines represent the theoretical 40% thickness reduction. .... 143

Figure 7.3: Buckling effect of the lateral sides (red arrows), and spreading effect of the material from the bottom of the defect (blue arrow). The continuous and the dashed lines represent the defect before and after rolling respectively. .... 144

Figure 7.4: Experimental measurement and prediction of the final length for defects with different initial depths and widths.....	147
Figure 7.5: Left) final width prediction, for different initial depths and lengths, Right) final depth prediction, for different initial widths and lengths.....	148
Figure 7.6: Friction coefficient dependence on temperature and oxide scale thickness [50]. .....	150
Figure 7.7: Mechanism of scale formation and descaling in Si steel, before (a) and after (b) descaling [94].....	151
Figure 7.8: Variation of friction coefficient with temperature for different steels, and chemical analysis of the tested steels: St20 (1), A20 (2), 30HGSA (3), H18N9 (4), EJ94 (5) [64]. .....	155
Figure 7.9: Theoretical effect of sticking between the roll and back side of the defect. White pointed line present the case where no sticking is present, the red line present the hypothetical case where sticking between slab and roll is present the longitudinal back end of the cavity.....	159
Figure 0.1: Transversal section of the defect with an initial width of 3mm. ....	173
Figure 0.2: Transversal section of the defect with an initial width of 11mm.....	174
Figure 0.3: Transversal section of the defect with an initial width of 7mm.....	174
Figure 0.4: Pin distortion pattern for slabs heated at 1100°C for different slabs and pins.....	175
Figure 0.5: Pin distortion pattern for slabs heated at 1150°C for different slabs and pins.....	176
Figure 0.6: Pin distortion pattern for slabs heated at 1200°C for different slabs and pins.....	176



# 1 INTRODUCTION

Hot rolling is a key metal forming process that converts cast or semi-finished material into finished products. This research is focused on the hot rolling process of a high silicon steel alloy widely used in the electrical industry because of its superior electrical properties. The surface quality of the final product is extremely important as superficial defects are sources of poor magnetic properties. Therefore, it is essential to detect, reduce, and when possible, eliminate the surface defects to produce high-quality electrical steels.

## 1.1 Problem description

Nowadays, the presence of surface defects remains one of the problems in the hot rolling process, this is because they interfere with the performance of the final product. During the process, multiple factors simultaneously play a role in the generation of defects including imperfections of the surface due to shearing against a guide or collar, impurities in the billet during solidifications and contractions due to excessive cooling.

In the rolling of silicon steels, the oxide growth on the transport rolls surfaces that transfer the slabs during the process is stimulated by the high temperatures of the furnace. This results in surface irregularities and protrusions on the surface of the transport rolls in contact with the slabs.

The surface irregularities present on the transport rolls are identified to be an important cause of defect generation during rolling [1], in fact, slabs bottom surfaces can be easily indented during the contact as the mechanical resistance of the slabs is reduced due to the high temperature of the process. The size and the aspect ratio of these initial features are crucial parameters determining whether they can be eliminated during the rolling deformation. For this reason, an appropriate study on the effect of the geometry of the initial cavities on the final defect feature is needed to understand how to reduce the defects in the final product.

The problem of the defect generation is further complicated by the continuous exposure of the metal to air, and the high temperature at which the slabs are

subjected to (this is about 1250 °C) [2-5] that produces oxide scales on the surfaces of the slabs and inside the indentations formed during the transport. Although high-pressure water spray is used to remove oxide scales just before the rolling [6], where the irregularities of the transport rolls have generated dents or sufficiently deep depressions, the oxide is trapped under a flap of metal. Therefore, it is impossible to be removed after the first rolling stand.

Moreover, the surface defect deformation is influenced by the material properties of the slab involved in the process; the high strain rates and the temperature variations of the slabs affect the response of the material during the rolling procedure

Important factors that affect the generation and the evolution of defects are the process parameters of the rolling process, in fact, parameters as friction and heat transfer coefficients are expected to strongly affect the defect behaviour during rolling. These parameters are strictly related to the thickness and composition of the oxide scales formed at the interface of the contact between the slab and rolls. For this reason, oxide scales play a crucial role in the deformation behaviour of the defects. The formation of oxide scales on carbon and silicon steel at high temperatures was found to influence both friction and heat transfer [5, 7-15]. In terms of friction, the scale layers can act as a lubricant or abrasive depending on its thickness, temperature and chemical composition. With regards to the heat transfer, as the scale layer has a lower thermal conductivity compared with the steel [2, 13, 16], scales act as thermal barriers reducing the heat transfer coefficient between the roll and the slab where thicker scales are present.

Consequently, the main factors that generate and affect the evolution of the initial surface indentations in hot rolling processes are varied in nature, including geometry, mechanical properties of the material, frictional and thermal conditions of the contact zone, rolling parameters (as reduction ratio or rolling temperature). Investigation on the effects of the initial geometry and process parameters on the final defect severity is necessary to improve the quality of the final product. As the interactions between these factors influence and

complicate the process, they must be considered simultaneously in any experimental or numerical investigation.

## **1.2 Purpose of the research**

Several variables are involved in the hot rolling operations of metals and their interactions are extremely complex. The Finite Element modelling methods are effective to simulate processes where multiple variables are involved. Furthermore, computer calculation speeds have evolved much in recent years making this approach more efficient than the physical experiments.

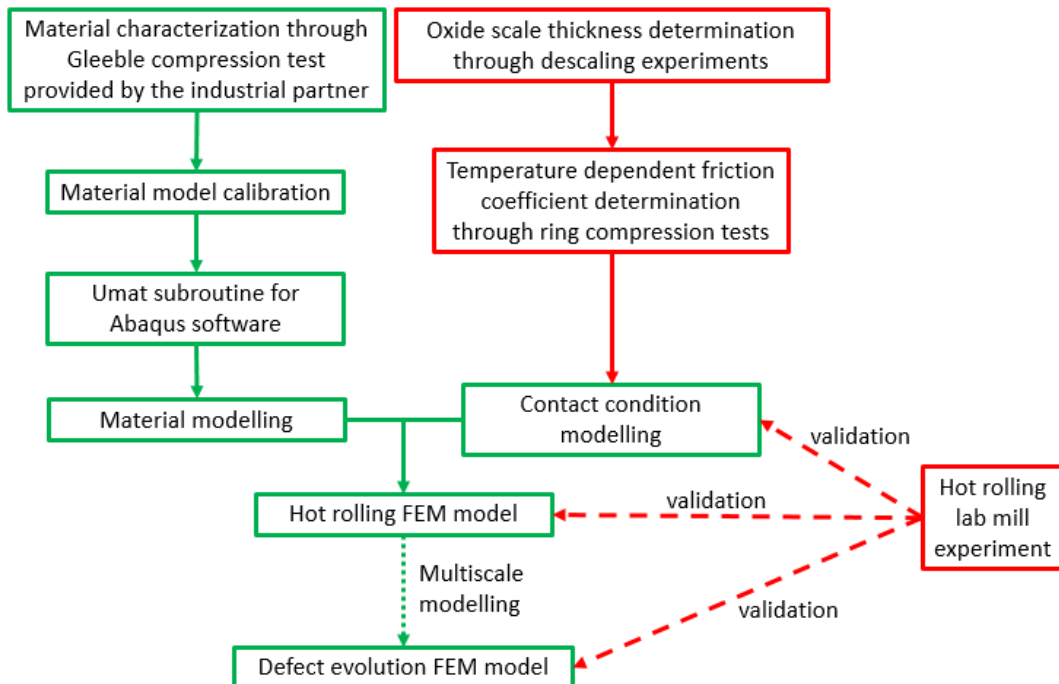
This research aims to develop a predictive finite element model (FEM) to simulate the deformation and evolution of predefined surface defects during a hot rolling operation of high silicon content electrical steel and to determine a list of different geometric parameters of defects that can be eliminated through the rolling process, for different process conditions. This could help the industry in understanding how they need to reduce the defect before the rolling process to be completely eliminated after. The project is focused on the first rolling stand only; this stand is considered the most important because the slab is rolled for the first time and high reduction in thickness is applied. Abaqus finite element package was used for developing a Three-dimensional model of the process, in particular, a user subroutine was developed to simulate the specific behaviour of the material at different strain rates and temperatures. The novelty of this research was related to the development of the adequate material model and comprehensive modelling approach for prediction of surface defects evolution in the rolled material for Si-content steels. The novelty also includes a new and flexible methodology that can be used to predict the evolution of defects of different geometries for different process parameters and materials.

The project is focused on the defects present before the rolling, in particular, on those generated by pressed oxides scales irregularity of the transport rolls to the slab. Initial sets of defects with different shapes and initial dimensions were analysed (no previous studies were conducted for three-dimensional defects of

different aspect ratio), and their behaviour during different process conditions was simulated.

Hot rolling and ring compression experiments were performed for the first time for 3% Si steel in collaboration with the industrial partner of the project to evaluate specific coefficient of friction for different thickness of oxide scales and temperatures. The oxide layer was not modelled in this study; it is assumed having a negligible thickness and mechanical resistance and to affect only the thermal and frictional conditions during the contact. Descaling experiments were conducted to estimate the final oxide thickness during the process after the descaling, and the effectiveness of the descaling in the cleaning of initial cavities of different dimensions.

A 3D thermo-mechanical model was finally developed where the temperature and the strain rate dependence of the material model were taken into account through a user defined subroutine. Finally, the model was validated against lab scale rolling experiments and then used to reproduce the process in real scale, and the defect evolution during rolling. A graphical abstract is presented in Figure 1.1 to describe the work carried out, the modelling activities and the experimental activities are highlighted in green and red respectively.



**Figure 1.1: Graphical abstract of the work.**



## 2 LITERATURE REVIEW

### 2.1 Electrical steels

Silicon steels (or electrical steels) are widely used in electrical applications because of their superior magnetic properties compared to other grades of steels. The material properties of this steel are achieved through the combinations of three precautions: the high content of silicon in the alloy, the final thin gauge of the coils produced and the specific grain orientations of the steel. Those precautions are obtained through a hot rolling process wherein slab thickness is gradually reduced. A total of seven mills are used for the whole process.

A large thickness reduction of about 40% is carried out by the first roughing mill and it is sufficient to generate irreversible defects since the first rolling stand. If defects are formed, they could be carried out and deformed for all the next stages. Elongated defects on the surface of the final product may form and in very extreme cases, defects as long as few meters originated from small defects carried out in the process can be found on the surface of the final products.

### 2.2 The hot rolling process

During rolling, slabs with a thickness of about 70 mm are reduced in thickness down to 2 mm. The key processing steps of the rolling process considered for this research are summarised in Figure 2.1.

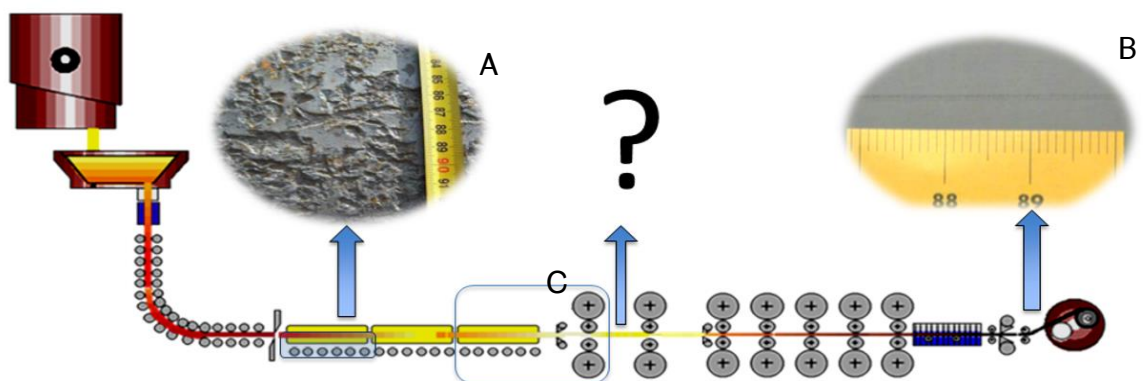


Figure 2.1: Schematic of the hot rolling process, defects slab before (A), after the rolling (B), and first rolling stand (C).

After casting, the slab enters a tunnel furnace where it is homogenised at a temperature of 1100-1160 °C; the strip width is 1120 mm. The rolling operation is performed continuously on two roughing stands followed by further five finishing rolling stands. The first and the second roughing mills with a diameter of about 1000 mm are used reduce the slab of 37% and 51% in thickness respectively. The remaining mills further reduce the thickness to the final thick gauge. To remove the oxide from the slab surfaces before the rolling two water-jet descaling systems are installed: the first one is positioned just before the first roughing mill; the second one is positioned just before the first finishing mill.

The defects taken into account for this research are generated in a tunnel furnace, where the transport mills guide the slab to the first roughing mill. The irregularities of the transport rolls surface indent the bottom of the slab (Figure 2.1A). The most critical indentations containing oxides and are roll closed during the first rolling stand. These are sub-surfaces defects and are not visible until further rolling reductions are done (Figure 2.1B). The most defected surface is the bottom surface; this is because of the continuous contact with the transport rolls of the furnace. Figure 2.2 shows a typical bottom slab surface just before the first roughing stand.



**Figure 2.2: Bottom surface quality after the tunnel furnace (TATA steel images).**

This project is focused on the first roughing mill (Figure 2.1C). This stand is the most critical because here the first deformation of the defect is done.

### **2.2.1 Types of defects in hot rolling processes**

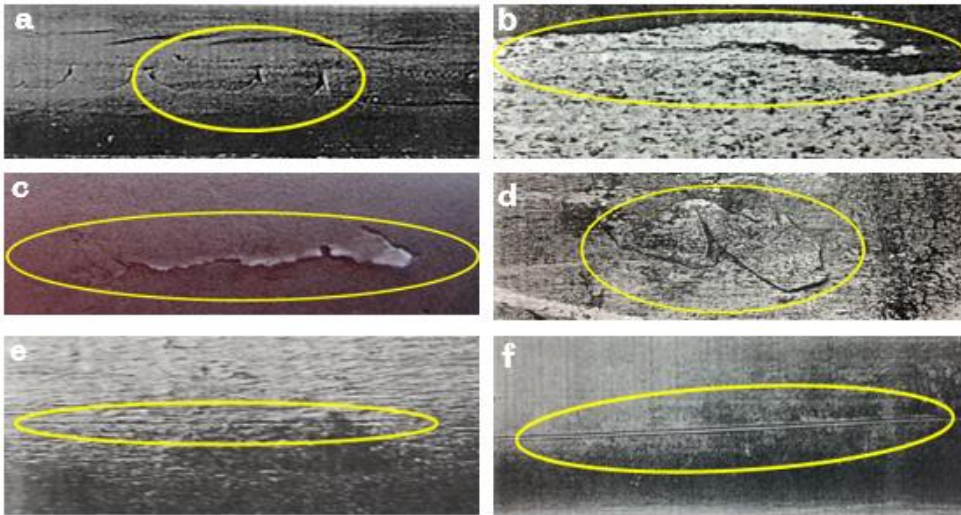
Surface defects on strips are generated in two different ways [17]:

- Initial defects were present on the slabs before the rolling, whose shape and dimension will then be altered during the rolling process. This is, in general, the case of Slivers and Scabs.
- Defects appear on the surface after the rolling process due to various reasons like mill shearing.

The main defects occurring during the hot rolling process are listed below. Their definitions are provided by “AISI Technical Committee on Rod and Bar Mills, Detection, Classification, and Elimination of Rod and Bar Surface Defects” [18]:

- Mill shearing: Longitudinal strips of material that are torn off and reattached subsequently not necessarily in the same bar (Figure 2.3a). The reattachment and the detachment are both considered mill shearing. The acknowledgement that the attached material is a foreign material, can help distinguishing it from another type of defects.
- Slivers: Elongated pieces of the material attached at one end in the slab after the rolling. Slivers (Figure 2.3b), may be caused either by bar shearing against a guide or collar, incorrect entry into a closed pass, or a tear due to other mechanical causes. Also, they may be the result of a defect that carries through the process. Non-metallic inclusions are formed and trapped under the slivers; this is, therefore, one of the most dangerous defects.
- Laps: Crevices (Figure 2.3c) created by folding over and not welded material. It is usually generated at the mill, although initial longitudinal crevices may exist before to be rolled.
- Scabs: Protrusions caused by different causes (like splash, boiling, teeming reasons) which are flattened during the rolling process (Figure 2.3d). Scabs are always present before the rolling, they are ductile and this differentiates them from the mill shearing.

- Seams: Longitudinal crevices that are closed during the process, without material welding (Figure 2.3e). Seams can be confused with scratches because of the longitudinal direction.
- Scratches: Indentations caused by rubbing of the work-piece with protrusion during the process (Figure 2.3f).



**Figure 2.3: Type of defects encountered in the slab after rolling: mill shearing defect (a); cross section of a sliver defect (b); lap defect (c); scab defect (d); seam defect (e); scratch defect (f).**

### 2.2.2 Previous experimental research

In the past decade, a large body of research have investigated the origin and the evolution of the defects in order to reduce or prevent their occurrence.

With regards to the defects generated during rolling, two are the landmark studies reported in this review. Hong Xiong [19], conducted a study on longitudinal cracks and their origins on thin slabs. Analysing the forming reasons, he concluded that the control of the surface quality of the slab, quality of the water used in the process, and the maintenance of a good relationship between the temperature and the velocity of the casting, was effective to reduce and prevent the formation of cracks. Similar results were obtained in a study by Genzano [20] who worked on the minimization of the surface defects on wire

rods and bars. Genzano concluded that cracks are generated by tensile stresses during strengthening as temperature decrease or due to sticking with the borders of the guides when they are located in the corners. The solution proposed was to use thermal modelling to determine a proper cooling set up of the bars in order to avoid dangerous temperature ranges in the corners.

Studies related to defects generated by impurities present in the slab before the rolling report useful information regarding causes of defects. Zhou [21] studied the surface of defected thin rolled strips concluding that impurities and iron scales present on the surface were the main source of defects. A further demonstration of this phenomenon is presented in another study [22], where rolled slabs with surfaces containing defects were collected and cold rolled. A comparison of the condition of the defects before and after the cold rolling was carried out. It was concluded that the initial impurities generated defects of different nature. In particular, spherical powder mould marks resulted in final black marks, and surface linear mould powder marks resulted in slivers of different severities.

A number of authors have studied defect evolutions of initial features using experimental approaches. Tripathy [23] developed a combination of numerical and experimental techniques to simulate the rolling of slabs containing embedded defects at different depths from the contact surface between slab and roll in order to evaluate the movement of these defects and their behaviour during rolling. This was done through a step machining procedure where slabs were subsequently cut and machined in steps of 1 or 2 mm, and the internal defects were detected in term of size, position and shape. The numerical methods consisted in a FEM study of the hot rolling process, in order to evaluate the movement and the size variations of the defects during the process. It was concluded that defects with certain initial size and depth can be completely removed during the rolling process. Furthermore, it was observed that size and number of defects are inversely correlated with depth (from the surface) for a given set of conditions. The effect of the initial defect size on its elimination was also analysed by Merwin [24] on a tin-grade steel. It was concluded that the initial

depth of the imperfections plays an important role on the severity of the final defect. This was done by applying artificial surface imperfections to casted slabs and studying their behaviour during hot and cold rolling. With this procedure, deeper defects with an initial depth of 20 mm and 30 mm were not eliminated during rolling, and the percentage of eliminated defects with the depth of 10 mm and 5 mm were 67% and 75% respectively. Oxide particles were found in the vicinity of every defect for the hot rolling case. The physical appearance of the defect was found to be different in hot and cold rolling operations. Defects appeared as elongated lines after the hot rolling experiments while they evolved to isolated spots for and the cold rolling case. These results are in agreement with Suresh [25] experiments, in which it has been demonstrated that with an exception for light cracks or indentations, any other defects have to be reduced or completely eliminated to prevent the formation of slivers during the rolling process.

### **2.3 Numerical modelling of hot rolling operations**

During the past 30 years, many researches have been conducted on the modelling of hot rolling processes [26-33]. The selected approaches differ in different aspects:

- Type of analysis (mechanical, thermal, coupled or uncoupled thermo-mechanical);
- Constitutive laws of the material model for roll and slab (rigid or elastic rolls; rigid-plastic, elastoplastic or visco-plastic slabs);
- Contact conditions (different pressure and temperature dependencies of friction and heat transfer);
- Type of discretization (3-D or 2D).

Hot rolling processes has been widely modelled, however, there is a relatively small body of research concerned with the modelling of the evolution and generation of defects during rolling. In recent years, more attention has been focused on this type of simulations as computer calculation have evolved [17, 34-40] leading to more efficient and more computationally cost effective analyses than the traditional experimental approaches. Nevertheless, experiments

cannot be avoided completely, as they are necessary to understand the behaviour of the material to be modelled as well as being an essential requirement for the validation of the models.

### 2.3.1 Material models for high temperature and high strain rates deformation

As the material is subjected to large deformation at high temperatures, adequate modelling strategy is required to predict their behaviour at such extreme deformation conditions. There are, currently, several models developed which take into account strain rate and temperature dependence on the material. Some of the most relevant models used to simulate general rolling processes and defect evolution during rolling are presented in this section.

#### 1. Johnson-Cook model

The Johnson and Cook model [41] is a purely empirical model (Equation 1) and is widely used because of the relatively easy process to calibrate the parameters as only three tests are needed. In this model, the mechanical behaviour of the material is obtained through the multiplication of the effects of strain, strain rate and temperature. The first term  $(A + B(\epsilon^p)^n)$  represents a reference hardening curve and it is usually obtained at room temperature and in quasi-static conditions. Parameter  $A$  represents the yield stress at reference strain rate and temperature and  $B$  and  $n$  represent the hardening parameters of the reference hardening curve. The second and the third terms in the right hand side of Equation 1 represent the sensitivity of the material to strain rate and temperature on the flow stress, respectively. The parameters  $C$  and  $m$  are material constants which represent the coefficient of strain rate hardening and temperature softening.

Equation 1

$$\sigma = (A + B(\epsilon^p)^n) \left(1 + C \cdot \log\left(\frac{\dot{\epsilon}^p}{\dot{\epsilon}_0}\right)\right) (1 - \hat{T}^m)$$

$$\hat{T} \begin{cases} 0 & \text{for } T < T_f \\ \frac{T - T_f}{T_m - T_f} & \text{for } T_f \leq T \leq T_m \\ 1 & \text{for } T > T_m \end{cases}$$

The terms  $\dot{\epsilon}_0$  and  $T_f$  represent the strain rate reference and the temperature reference of the model respectively. The term  $T_m$  represents the melting point of the material.

## 2. Sellars-Tegart model

The material model for deformations at high temperatures proposed by Sellars and Tegart[42] based on the Garofalo Hyperbolic sine law [43] is widely used (Equation 2 and Equation 2). This model offers a good representation of the effect of temperature on the mechanical resistance for wide ranges of stress, strain rates and temperatures.

The model equations are:

**Equation 2**

$$\dot{\epsilon} = A \cdot (\sinh(\alpha\sigma_s))^n \cdot e^{\left(-\frac{\Delta H}{RT}\right)}$$

**Equation 3**

$$\sigma_s = \sinh^{-1} \sqrt[n]{\frac{\dot{\epsilon} \cdot e^{\left(\frac{\Delta H}{RT}\right)}}{A}} \cdot \frac{1}{\alpha}$$

Where  $A$  ( $s^{-1}$ ),  $\alpha$  ( $MPa^{-1}$ ),  $n$  are material constants;  $R$  is the universal gas constant;  $T$  ( $^{\circ}K$ ) is the absolute temperature;  $\sigma_s$  ( $MPa$ ) is the ultimate tensile stress;  $\dot{\epsilon}$  is the strain rate;  $\Delta H$  ( $\frac{KJ}{mol}$ ) is the activation energy for plastic deformation at high temperature.

The four parameters  $A, \alpha, n$  and  $\Delta H$  can be calculated through a least square technique or by means of a numerical technique proposed by Uvira [44]. Both approaches adjust the parameters to better fit the ultimate tensile stress levels



at different strain rates and temperatures obtained from experimental compression tests.

### 3. Generic empirical models

Hai-Liang [45] used an isotropic bilinear temperature and strain rate dependent model (Equation 4) to simulate the behaviour of defects on the surfaces of slabs subjected to hot rolling. In Equation 4,  $\sigma_0$  is the initial yield resistance at specific strain, strain rate and temperature. It is evaluated by means of the Equation 5 where  $A, B, C, D$  and  $F$  are constants of the material and  $\varepsilon, \dot{\varepsilon}$  and  $T$  are the strain, the strain rate and the temperature respectively.  $E_p$  is the plastic modulus of hardening;  $\varepsilon_p^{eff}$  is the equivalent plastic strain.

**Equation 4**

$$\sigma_y = \sigma_0 + E_p \varepsilon_p^{eff}$$

**Equation 5**

$$\sigma_0 = A \cdot \varepsilon^B \cdot \dot{\varepsilon}^{C \cdot T + D} \cdot e^{F \cdot T}$$

The model shows a good fitting of the stress for different temperatures and strain rates and it was also used to simulate the material behaviour of inclusions in the slab. A bilinear hardening was also used by Galantucci [31] to simulate a rolling process. At low temperatures, the yield strength and the slope of the linear hardening have been considered as a function of the temperature only, the equation used at low temperature was not provided. For high temperatures, a perfect plastic stress–strain relation is assumed and the flow stress is obtained from Equation 6:

**Equation 6**

$$\sigma = C(T) \cdot \dot{\varepsilon}^{m(T)}$$

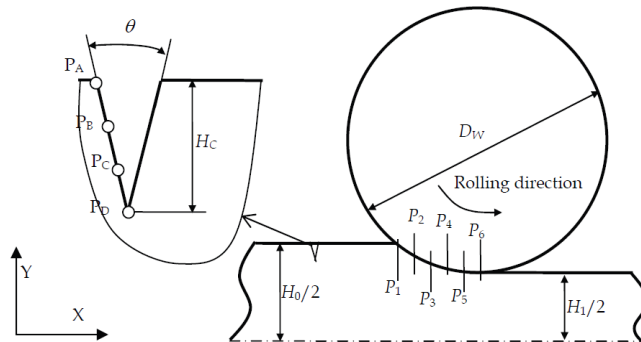
Where  $C(T)$  and  $m(T)$  are parameters that depend on the material and the rolling temperature.

In general, most of the authors utilise models which take into account the temperature and the strain rate dependency of the material. With regards to the modelling of rolls, they are usually assumed rigid to simplify the calculations.

### 2.3.2 Geometric modelling of the defects in hot rolling processes

The defect behaviour during rolling has been investigated with finite element modelling techniques and laboratory monitoring of the rolling processes parameters like dimension, evolution and movement of the defects. The defects have been characterised and many of the initiation mechanisms were understood.

Hai-Liang [45] has proposed a model with 2D V-shaped defects where the depth of the V-shaped crack ( $H_c$ ) and the angular opening of the crack ( $\theta$ ) was used as the distinctive parameters (Figure 2.4):



**Figure 2.4: Model scheme of slab rolling with a surface crack. [45]**

The effect of the friction on  $H_c$  and  $\theta$  parameters was investigated. The evolution of the defect geometry was also studied along with the stress distribution around the crack. The final open-angle and the final height of the crack after rolling were predicted under various initial conditions. The results of the study indicate that after rolling the crack open-angle increases with reducing the initial

crack height, and the crack height after rolling is directly related to the initial crack height. The evolution of v-shaped cracks in the corners and in the upper surface of a slab have also been analysed using 3D FE model [45, 46] to study how the friction affects the contact pressure and the width of the crack. The results showed that for friction coefficients up to 0.35 the cracks close during the rolling. However, for friction higher than 0.35, the final cracks width increase gradually with the friction coefficient.

In another study, Lee and Choi [37], generated a series of 2D simulations by classifying defects according to their initial ratio of width to depth. Figure 2.5 shows the classification of the defects after experimental tests as a function of width and depth for defects with thin oxide scale or thick oxide scale.

The three types of defects found were:

- A: Sliver-type, FeO type sliver.
- B: Two-line, defect with two very thin parallel lines.
- C: Band-type; defect whose width to depth ratio is larger than the one of the A-type.

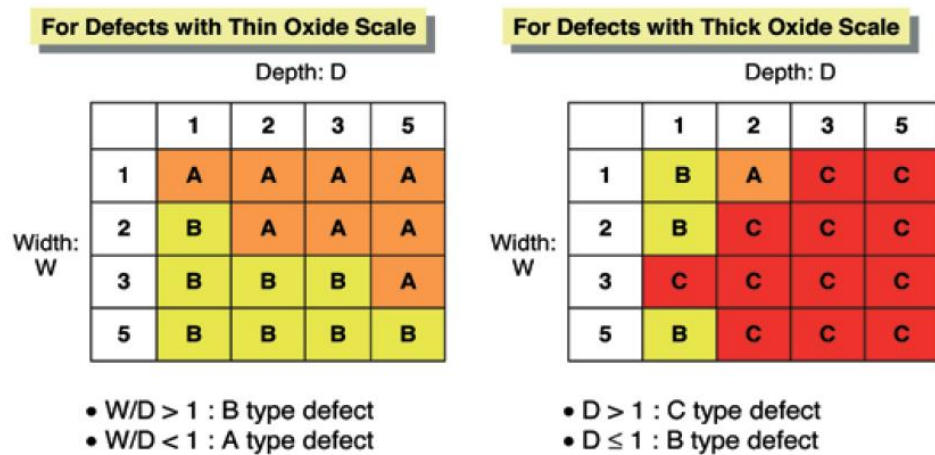
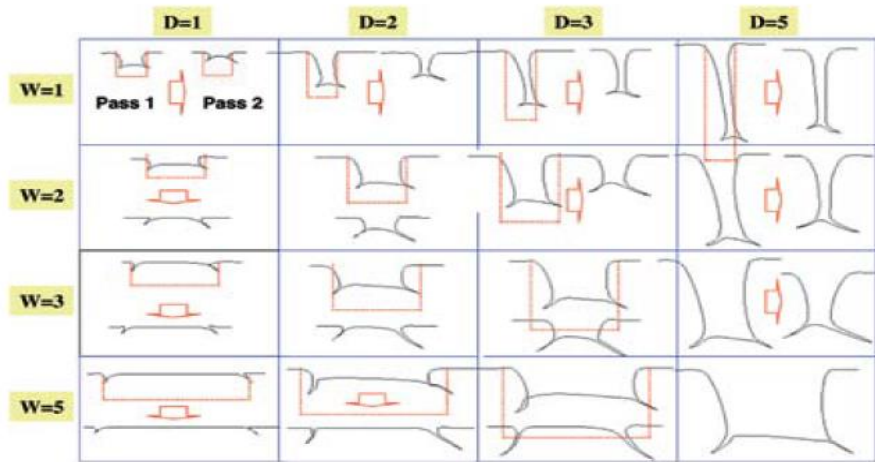


Figure 2.5: Classification of defect generated with width and depth. [37]



**Figure 2.6: Shape changes of the surface defects during multi-pass rolling. [37]**

**(W: width; D: depth; unit: mm).**

The cross-section of the defect of the experimental results was compared with the 2D model, and the defects generated during the hot rolling process were analysed based on this ratio before the rolling. The final severity of the defect was effectively determined in function of different initial aspect ratios. The severity of the final defects was found to decrease with the width to depth aspect ratios (WDR). Although the findings are interesting, the assumption of plain strain condition of the 2D model may not represent the three-dimensional nature of the defects deformation during rolling. As shown in Figure 2.6 crevices between the bottom and the lateral sides of the pinholes are formed during rolling as a result of the high deformations.

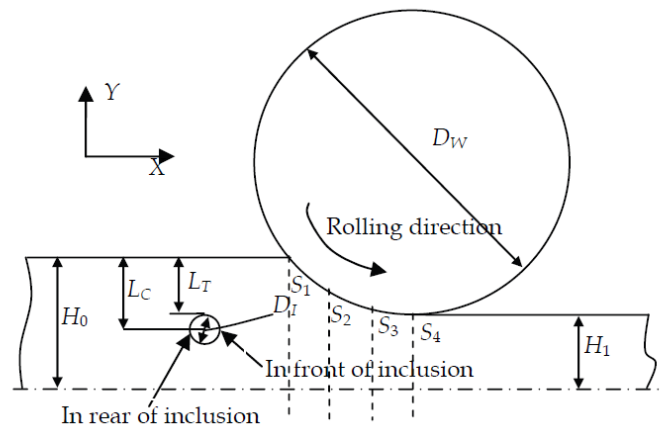
The three-dimensional deformation of surface defects is better represented in a recent study of defect evolution in cold rolling [47], where cylindrical dents and conical pinholes deformations on slabs subjected to cold rolling were simulated. A positive role of friction was noticed, in fact, it was found that higher friction coefficients are more effective to flatten the defects. However, no considerations about eventual crevice forming phenomena (as the crevice shown in Figure 2.6 [37]) were mentioned. This can be due to the nature of the cold rolling process where less deformation is expected because of the higher

strength of the material. However, only a few shapes and different dimensions of defects were considered, in addition, the research was limited to cold rolling. Deformation is expected to be more critical in hot rolling condition, therefore further investigations are needed.

Movement of defects during the rolling have also been studied with modelling approaches, Moir [38] studied the movement of the defects in the slab during the rolling using a tracking tool of the defect in an FE model. He concluded that the movement of the surface defect is strictly related to the magnitude of the lateral spread of material during the process and that the modelling could be very helpful to further investigate surface defect problems.

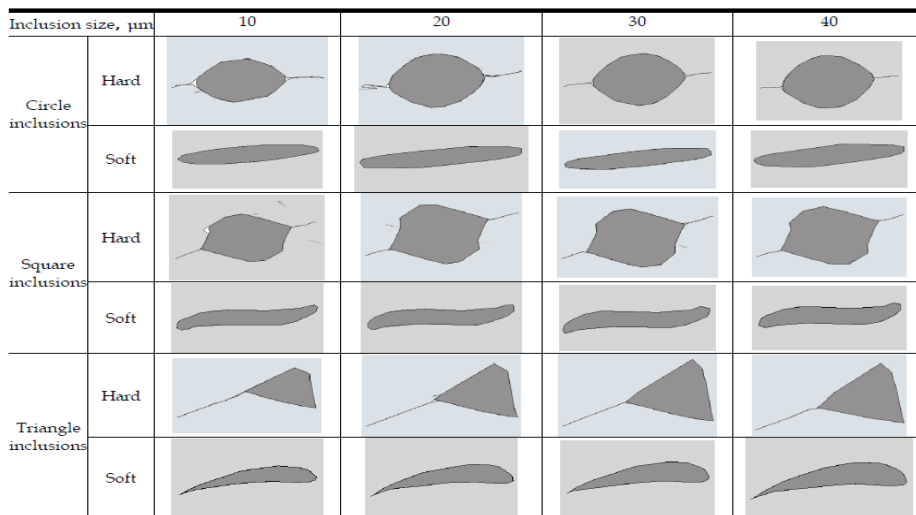
The effect of the inclusions in the materials has also been studied using Finite Elements [48]. The study was carried out for different initial positions and stiffness of the inclusion; in addition, the shape of the inclusion was modified.

Figure 2.7 shows the scheme used:



**Figure 2.7: Schematic drawing of a process of rolling with an inclusion. [48]**

The results showed that less distance between the inclusion and the strip surface was observed for hard inclusions after the rolling compared with the soft inclusions. Figure 2.8 shows the relationship between the inclusions and the strip matrix for various inclusion sizes and resistance when the inclusions are positioned at 1/4 of the strip thickness before the rolling.



**Figure 2.8: Relationship between the shape, dimension and resistance of the inclusion and the matrix after rolling, the inclusions are in the position of 1/4 of the strip thickness. [48]**

The model showed (Figure 2.8) that when the inclusions were soft, no cracks appeared around the inclusions under various inclusion sizes, shapes and dimensions and in general, a little rotation occurred for all elements. When soft inclusions were present, the material is deformed inside the crevice formed and this is more noticeable for triangle inclusion shapes. In the same study [48], inclusions with a layer of transition that separates them from the steel slab were simulated during rolling. A strain failure condition was defined for the transition layer elements. Cracks formed when strains on the layer reached the failure conditions. It was also observed that for failure strains limits lower than 0.1, cracks appeared on the transition layer with a direction of about 45 degrees with the rolling direction. Longer cracks were generated for lower failure strains values.

Concluding, it is worth to notice that most of the research involving in the modelling of defect deformation during rolling was focused in the two-dimensional analysis of crevices or holes deformations. Friction is found to play a role in the deformation of crevice but further research is needed to understand the effect of this parameter on different defect geometries and dimensions. In addition, other process parameters including temperature and reduction ratio are expected to play a role in the defect deformation, there are

not previous studies concerning the parametrical analysis of the effect of different process parameters on the defect deformation. In terms of model discretization, plain strain cannot be assumed in the defect zone, for this reason, three-dimensional models of the defect are needed to obtain further insight of the defect deformation.

### **2.3.3 Heat transfer and friction conditions modelling of hot rolling process.**

The modelling of the interaction between the mill and roll is a crucial issue for the simulation of hot rolling processes. The main boundary conditions that affect the process are the friction and the heat transfer between slab and mill. Both are strictly dependent on the oxide scale present between roll and slab [49, 50].

The sensitivity of the model behaviour to the friction coefficients is considerable, Roberts [51] describes friction to be the most important variable associated with rolling, for this reason, its control is considered essential to simulate each process. According to the literature [52, 53], the friction in hot rolling processes is usually modelled with the coulomb model as shown in the Equation 7:

**Equation 7:**

$$\tau_{crit} = \mu \cdot p$$

In this model, slipping is prevented as long as the frictional stress are lower than a critical value defined as the product of the pressure applied on the surface ( $p$ ) and the coefficient of friction ( $\mu$ ). In case of a large pressure (compressive stress) in the contact zone (e.g. rolling processes), frictional forces may exceed the flow resistance of the material. For this reason a limit on the  $\tau_{crit}$  is usually defined. The definition of the friction coefficient and its dependence on variables such as temperature and pressure is crucial for the contact definition. The next subchapter is focused on the experimental determination of friction coefficient in the rolling process.

Thermal history of the slab during the hot rolling process has a profound influence on the final properties of the product. During rolling, radiation to the environment, convection to descaling, backwash sprays, and heat conduction to the work rolls are main reasons of heat loss [52]. The complex thermal behaviour in the contact zone during the rolling makes the measurement difficult. Moreover, the parameters affecting interactions are numerous [54], and include temperature; speed; reduction ratio; rolling mill dynamic response; surface roughness; cooling systems; mechanical properties of rolls and workpieces; thermo-physical properties; oxide scale influence. For this reason, the heat transfer is often modelled with average values of HTC (heat transfer coefficient) assumed constant along all the contact zone [52]. Dissimilar values of HTC are proposed in the literature by different authors [55-60], confirming the difficulties of this kind of measurement in situ and the strong dependence on different oxide scale composition and thickness.

In determining a proper HTC between slab and roll, oxide thickness and pressures play an important role. As oxide works as a thermal barrier, the HTC decrease with the thickness of the oxide scale present. Conversely, higher pressures lead to higher HTC [59], because of the higher true contact area between slab and roll due to the superior pressures on the contact. According to this assumption, a recent publication [61] proposed an inverse engineering procedure to predict the heat transfer coefficients for a carbon steel in function of 3 oxide layer present, (wüstite, magnetite, hematite), and the contact pressure.

## **2.4 Measurements of friction coefficient**

Different authors have attempted to determine precise values of friction coefficient, or equations representing the dependence of the coefficient on temperature and pressure [54, 62-66] in a rolling process. The review of the literature show contrasting results; friction is found to increase or decrease with temperature depending on the research case. The most likely explanation



proposed by Lenard [63] is that chemistry plays a fundamental role in determining the friction coefficient between strips and roll; as tests were conducted on widely different materials, the different chemical composition and material properties could have affected the coefficient of friction measured. For this reason, when aiming to simulate a hot rolling process of specific materials, the best solution is to estimate the coefficient friction experimentally for the condition and material involved. There two different approaches to evaluate the friction coefficient: direct measurements; and inverse calculations.

In the direct measurement methods, shearing and normal forces are monitored and an average of friction coefficient is obtained from their ratio. An example of this approach is the embedded pin-transducer technique conducted for the first time by Siebel [67], and then adapted by other authors as Al-Salehi [68], Lenard [69] Rooyen [70]. With this approach measurements of contact pressure and frictional shears are used to determine the coefficient of friction. These approaches are very elaborate and costly.

In inverse calculations methods, parameters of the process are determined experimentally. The same parameters are calculated with a model reproducing the process where the friction coefficient is adjusted to match the experimental measurements. The quality of the friction coefficient estimated depends on the robustness of the model [71], and on the numbers of measured or calculated parameters [52]. This type of approaches usually involves measurement of deformation including longitudinal displacement measurements and grid distortion measurements of the strain pattern of slabs subjected to rolling, and deformation measurement of samples subjected to compression. Measurements of longitudinal displacement through embedded pins were criticised because of the contamination between the pins and their housing [71]. However, the method was used in different studies [68, 72-76] and remains a practical procedure if it is associated with a proper inverse modelling comparison and if the pins are proved not to disturb the strain pattern. Another technique used distortion patterns of grids to estimate the friction [77]. With this technique, a piece of metal previously manually carved obtaining a grid was

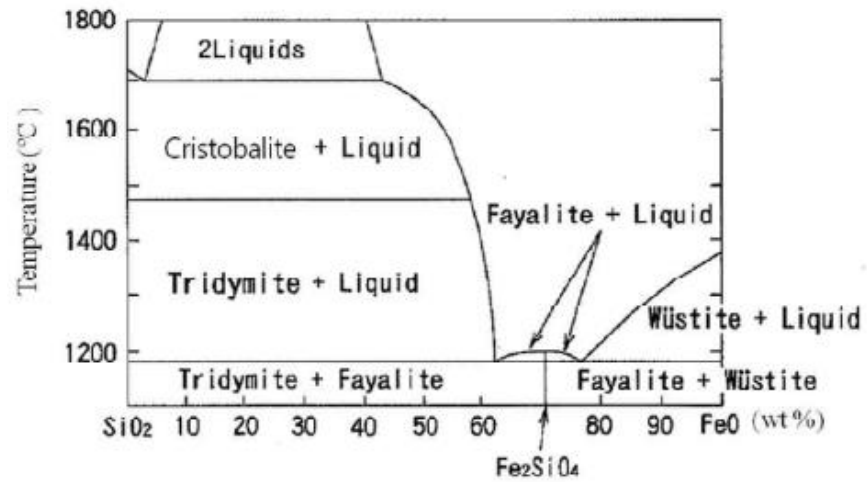
inserted normally into a slab; some pins were used to prevent the relative motion between the insert and the whole slab. The comparison between a model that reproduce the process for different friction coefficients and the grid obtained from the experiment allowed a successful evaluation of the friction coefficient of the process. The ring compression test approach, introduced for the first time by Male and Cockcroft in 1964 [78], has been widely used for friction determination purposes [65, 79-88]. In this test, a ring of the material is compressed, and the change of its geometry is related to the friction coefficient. Special care must be taken for the heat transfer conduction to obtain a realistic deformation in the simulations [89] for non-isothermal conditions.

## 2.5 Oxide scales in electrical steels

In general, when steels oxidise, three oxide scales forms on the surfaces: wüstite ( $\text{FeO}$ ), magnetite ( $\text{Fe}_3\text{O}_4$ ) and hematite ( $\text{Fe}_2\text{O}_3$ ). The scales are formed in increasing order of oxide content, which is lower in the substrate and higher in contact with the air. It is reported that at higher temperature the wüstite: magnetite: hematite thickness ratio is about 95:5:1. [90].

In steels containing silicon, as electrical steels, the oxide scale generation is more complicated. In general, the presence of silicon reduces the oxidation rates of the steel. In fact, as silicon is less noble than iron, a silicon rich oxide layer is formed at the interface ( $\text{SiO}_2$ ). This effect is more evident for higher contents of silicon as 3% or more [11]. In low alloy steel, the  $\text{SiO}_2$  formed at the surface interacts with the  $\text{FeO}$  to form fayalite  $\text{Fe}_2\text{SiO}_4$ . The presence of fayalite slows the diffusion of iron through the layer, as the diffusion of iron is higher on wüstite. The diffusion is slower for higher silicon contents [91]. Different behaviour is noticeable for temperature above the melting point of the fayalite ( $1170^\circ\text{C}$ ).

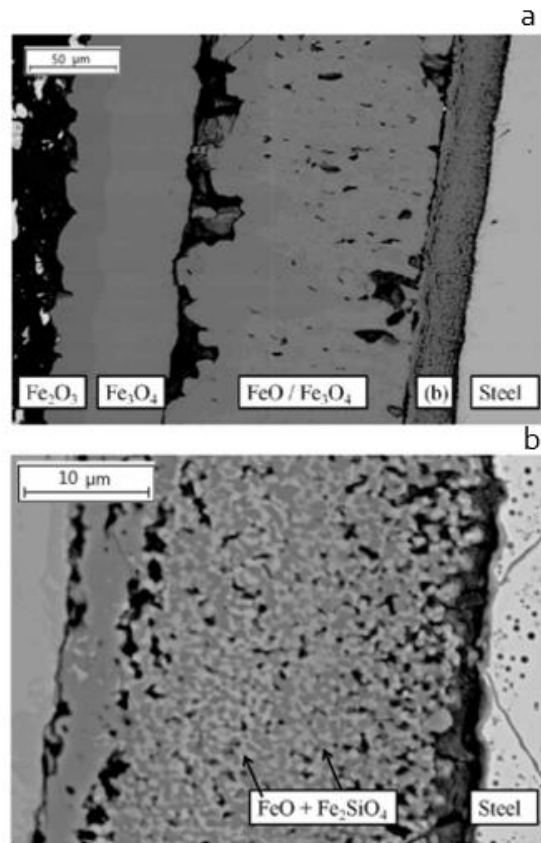
To understand the oxide generation at higher temperatures a phase diagram of  $\text{FeO-SiO}_2$  is needed (Figure 2.9).



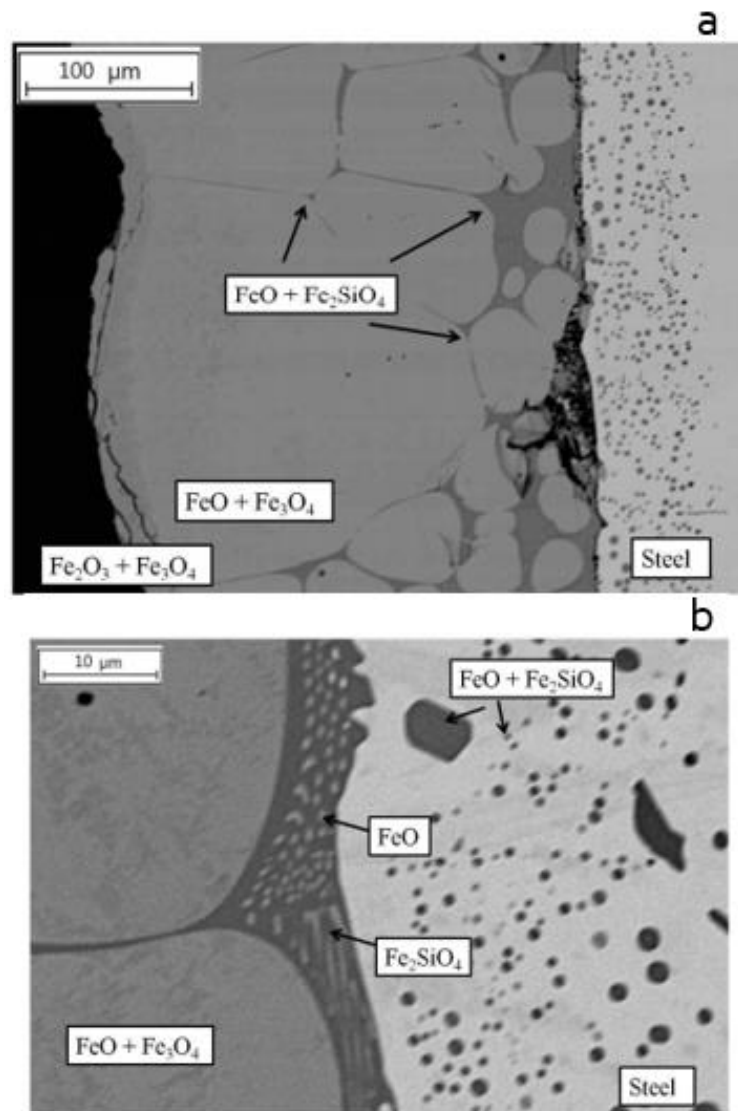
**Figure 2.9: FeO-SiO<sub>2</sub> phase diagram [92].**

As noticeable from the diagram, for temperature higher than 1170°C, fayalite starts to melt. The liquid phase can then penetrate the FeO, and after the cooling, the FeO-Fe<sub>2</sub>SiO<sub>4</sub> compound is formed. The penetration of fayalite is found to be higher for higher silicon contents.

Oxide scales generated under and above the fayalite melting temperature are presented in Figure 2.10 and Figure 2.11 respectively.



**Figure 2.10: Oxides formed at 1000°C for 2 hours for a silicon steel [15], (a) shows the entire oxide layer, (b) shows an enlargement of the FeO-Fe<sub>2</sub>SiO<sub>4</sub> compound.**



**Figure 2.11: Oxides formed at 1250°C for 2 hours for a silicon steel [15]. (a) and (b) show a lower and higher magnification respectively.**

It is worth to notice that the diffusion of fayalite at high temperature as highlighted by the arrows in Figure 2.11a. This behaviour is not noticeable at lower heating temperatures, and only a thin fayalite layer is formed (Figure 2.10).

The eutectic compound FeO-Fe<sub>2</sub>SiO<sub>4</sub> is demonstrated to be harder than the FeO scale [93]. This was demonstrated through a micro-Vickers hardness measurement, the Figure 2.12 shows the hardness of different oxide scales for different silicon content.

Oxides	Hardness (GPa)		
	Fe	Fe-1.5 wt% Si	Fe-3.0 wt% Si
Fe <sub>2</sub> O <sub>3</sub>	-	0.32	0.53
Fe <sub>3</sub> O <sub>4</sub>	0.08	-	-
FeO+Fe <sub>3</sub> O <sub>4</sub>	0.05	-	-
FeO	0.05	-	-
Fe <sub>2</sub> SiO <sub>4</sub> +FeO	-	0.50	-
Fe <sub>2</sub> SiO <sub>4</sub>	-	-	0.63
Substrate	0.12	0.04	0.03

**Figure 2.12: Oxide scale hardness at 1000 °C after oxidation at 1000°C for different silicon contents [93].**

It is worth to notice the higher resistance of fayalite compared to the others oxide scales formed.

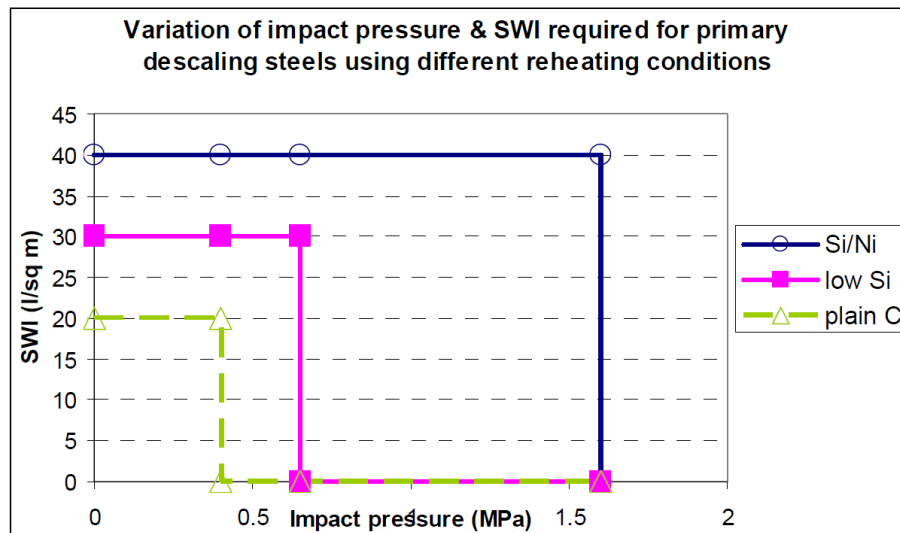
## 2.6 Water spray descaling in hot rolling processes

High-pressure water spray is a technique which involves in subjecting continuous sprays of water on surfaces to clean them. This technique is largely used in hot rolling operations to remove oxide scales from the surfaces of the material before being rolled. This is an essential procedure to obtain a good surface quality final product especially for difficult to descale steel grades as electrical steels. The oxide resistance to descaling of electrical steel is due to the very high strength of the FeO/Fe<sub>2</sub>SiO<sub>4</sub> compound at high temperatures present between the steel and the FeO layer [94]. In-depth understanding of the mechanism of the oxide scale descaling is necessary to determine the specific optimum descaling set up for steels difficult to descale.

There are four main mechanisms of descaling reported in the literature [95]: mechanical impact; delamination due to shear; differential thermal expansion; and breakage due to steam, and boiling effects. The first two may be described

as mechanical mechanisms while the latter two mechanisms are thermally dependent.

The impact pressure (IP in MPa) and the specific water impingement (SWI in  $l/m^2$ ) are the key parameters which determine the effectiveness of the descaling. The impact pressure is usually calculated in function of the flow rate, stand-off distance and spray angle, and system pressure. It represents the force of the water impacting the surface. The specific water impingement is defined as the area of the feedstock covered in terms of volume of water per unit area and depend on the flow rate, descaling width, and product speed. The two parameters are not independent as both depend on the flow rate of the water spray. However, higher impact pressures clearly favour the mechanical mechanisms, while higher impingements induce the thermally based mechanisms. Experimental trials on laboratory rigs were carried out by different authors to determine combinations of IP and SWI which lead to satisfactory descaling [96, 97]. As an example, Figure 2.13 shows a SWI and IP set up for different steel composition [97].

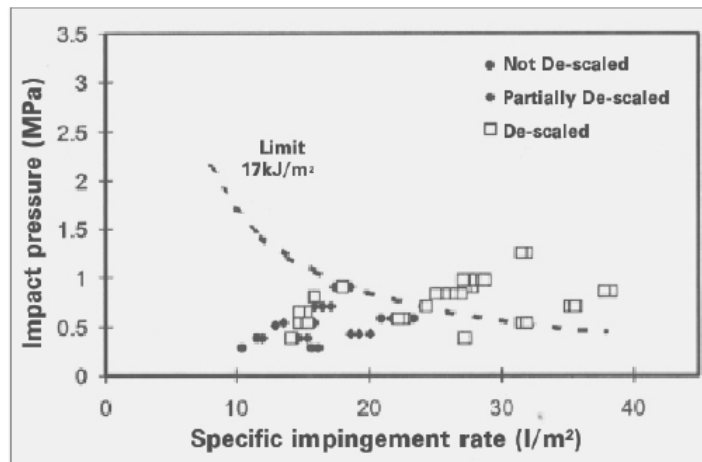


**Figure 2.13: Typical SWI, IP set-up for different steel composition [97].**

It is worth to notice the higher IP required for Si steel grades. The combination of SWI and IP above the limits defined in the graph represent safe set-up of the

descaling. However, the limits do not represent the optimum set-ups for the descaling.

The product of the IP and SWI defines the impact energy (IE)(KJ/m<sup>2</sup>) or descaling energy. The concept of impact energy [96] proposed that a limit energy must be exceeded to ensure the descaling of a specific oxide scale. According to this concept, iso-energy curves (combinations of IP and SWI whose product is constant) can be represented in an X-Y plot of IP function of SWI. Figure 2.14 present an example of the impact energy approach for a C-Mn steel [96]. According to the graph, an energy of 17 KJ/m<sup>2</sup> is required to remove the scale. The curves are defined based on experimental observations.



**Figure 2.14: Descaling energy required for C-Mn Steel [96].**

Depending on the material and reheating, specific set-up are usually studied, however the descaling usually requires [95]: sufficient overlap of adjacent nozzles spray, necessary to overcome the lower pressures at the ends of the spray widths; a reduced spray thickness which can be obtained varying the depth angle (few mm); a small stand-off (about 100 mm), very important to guarantee a laminar flow and a small spray angle (max 30°). Figure 2.15 represent a scheme of the parameters previously mentioned.



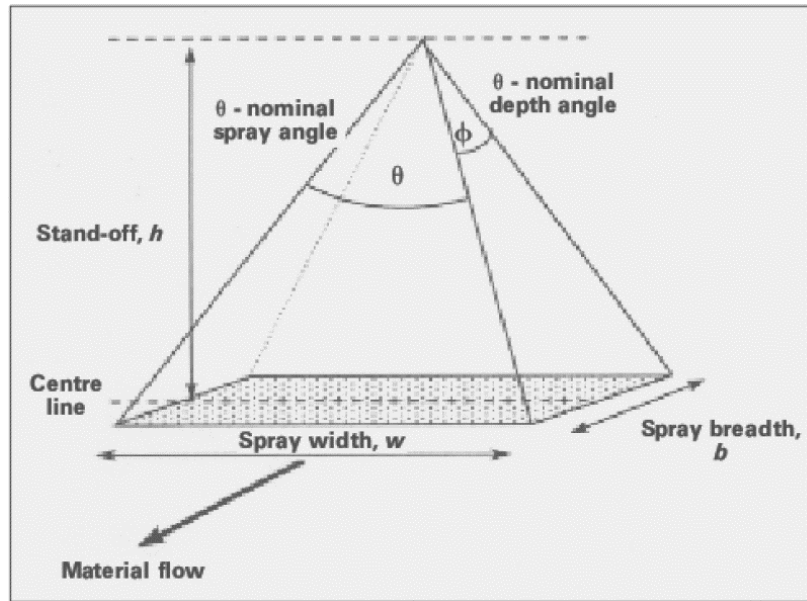


Figure 2.15: Impingement area scheme [96].

The descaling application results in temperature drops of the metal. On one hand, reduced temperatures at the surface are beneficial with regards to the secondary oxide growth after the descaling as lower temperatures reduce the oxide growth rates. On the other hand, slabs excessively cooled may result in high roll forces and increased roll wearing. The effect of cooling is found to be proportional to the water flow rate, and inversely proportional to the speed and the thickness of the block. For this reason, lower impingement minimises the cooling effect.

## 2.7 Summary

In summary, the results of previous studies show that the final defect shape and dimension depends on several factors. With regards to the geometrical aspect of the defect, it has been shown the importance of the initial geometry on the final defect state.

It has been also reported the importance of the initial position of the defect, in fact, defects near to the free lateral sides of the slabs behave differently compared to the defects present in the central band of the slab. This is because of the lateral spread of material.

The behaviour of defects is also found to be strongly affected by process parameters as friction and heat transfer coefficients; velocities of the process; initial temperatures; roll dimensions; thickness reductions ratios.

Despite being mentioned at the end, the mechanical properties of the slab and the defect is crucial in determining the behaviour of the defect, for this reason, a good understanding of the mechanical behaviour of the material at different strain rate and temperatures is essential for the modelling of the process.

It is demonstrated that final defects can be reduced or eliminated if the initial surface indentations are minimised enough before being rolled as the final state of the defect is strictly dependent on its condition before the rolling. Process parameters like temperature, reduction ratio and velocity can also affect the quality of the final surface. The FE modelling is proved to be a very helpful approach for surface defect problems, in particular, the software Abaqus is very effective for this type of simulations involving in contact. A three-dimensional model is necessary to take into account the three-dimensional nature of the defect deformation during rolling, and an accurate evaluation of the friction coefficient is essential to obtain precise results. However, experiments are necessary to support the model in terms of validations and inverse modelling calculations.

### **3 EXPERIMENTAL APPROACH**

This chapter focuses on the methodology adopted for the experiments conducted. The experiments aim to provide insight into the evolution of the initial indentations present on slabs during rolling and to evaluate the friction at workpiece/roll interface. The friction dependence on temperature and oxide thickness was also investigated.

The indentation evolution study was conducted by machining initial cavities of different dimensions on the surface of a particular electrical steel and applying a single thickness rolling reduction to the obtained slabs. The results of this experiments are essential outputs for the validation of the model reproducing the defect behaviour during the hot rolling. Pins were inserted in the slabs to measure the longitudinal strain distortion pattern present during rolling, these data were used in the modelling stage to calibrate the model to achieve the similar strain patterns produced during the experiment.

Friction coefficient is a crucial parameter which definitely affects the defect evolution during rolling. Oxide thickness and temperature are the main parameters affecting friction. Descaling experiments were carried out to estimate the oxide thickness present in the slab during the rolling and the effectiveness inside holes of a different dimension.

The oxide thickness determined was then reproduced on ring samples through specific heat treatments and tested at different temperature conditions through a hot ring isothermal compression tests to estimate the effect of temperature on the friction coefficient.

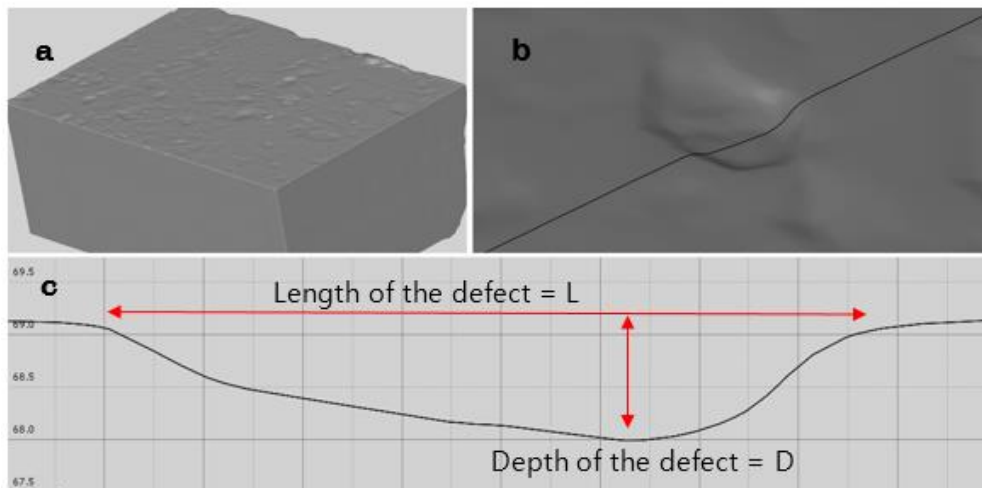
The effect of different oxide thicknesses on the final longitudinal strain pattern formed after rolling was tested inserting pins on slabs heated and rolled at different temperatures.

### 3.1 Hot rolling of samples with artificial defects

The hot rolling experiment of slabs containing defects was conducted in IJmuiden (Tata Steel Europe, Netherlands), the material and the equipment used for the experiment was provided by the industrial partner of the project (Tata Steel Europe). The sample preparation was carried out in the facilities of the University of Sheffield.

Two electrical steel casting slabs with a 3% Si content were carefully selected from the continuous-cast slabs of a roughing mill stand. A 3D optical scanning of the initial surface indentations was provided by the industrial partner. The 3D scan of the slab was analysed through the “GOM inspect 3D” software, and all the defects were characterised with respect to their size, and distribution in the rolling (RD) and transverse (TD) directions. This was done by sectioning each defect longitudinally and transversally from the 3D scan provided.

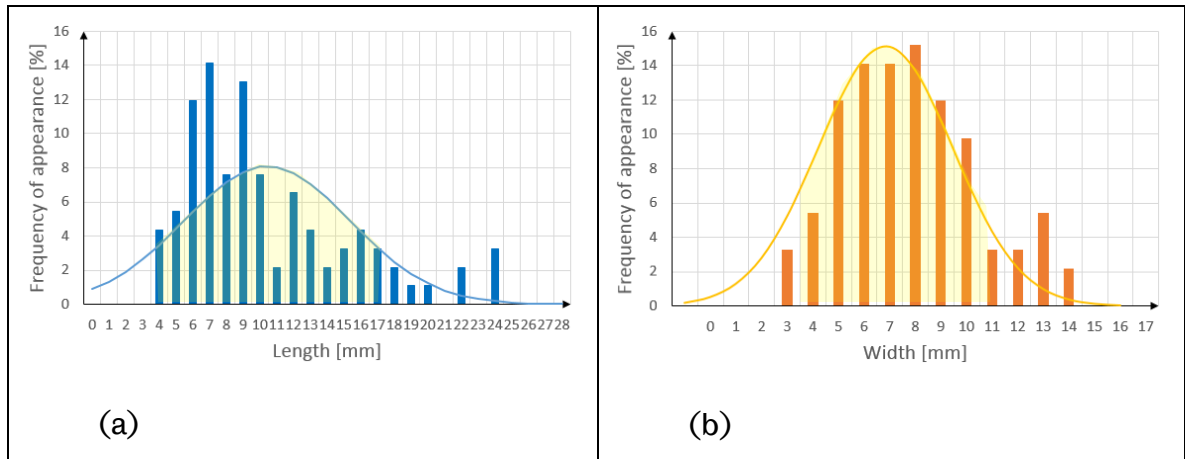
Figure 3.1 shows an example of a 3D scanned slab provided (Figure 3.1a). The top view of the defect sectioned by means of the software “GOM inspect 3D” (Figure 3.1b), and the measurement scheme used to evaluate the defect length, width and depth dimensions (Figure 3.1c):



**Figure 3.1: 3D scan of a transfer bar before the rolling (A), section scheme used to identify the dimension of the slab (B), and the measurement scheme adopted (C).**

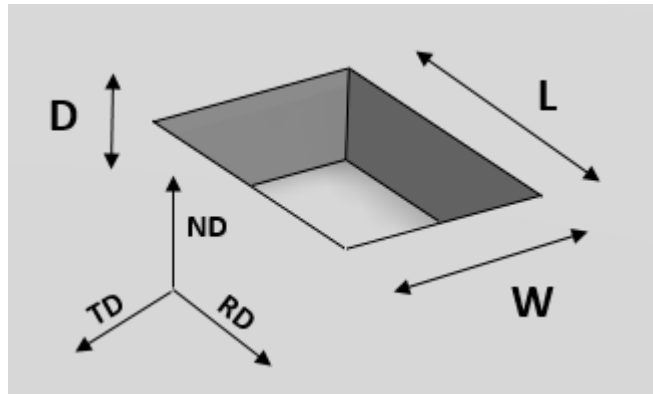
The measured values were analysed with respect to their frequency of occurrence. Figure 3.2 shows the analysed results for about 100 defects

identified at the surface of the selected sample. The bar charts represent the measured length (Figure 3.2-a) and width (Figure 3.2-b) dimensions and the solid lines are the normal distribution curves fitted to the experimental measurements. The latter is used to determine size and number of defects to be manufactured in order to be the most representative of the actual surface conditions in the laboratory rolling experiments.



**Figure 3.2: Normal distribution of (a) length and (b) width of the defect present in the slab before the rolling process**

Eleven sections with a size of 115mm x 85mm x 25mm were cut from the initial casting slabs. Cavities with different parametric dimensions (Figure 3.3) were designed to resemble the surface defects prior to the rolling process, the rolling, transversal and normal direction are indicated with RD, TD and ND respectively. The length (L), width (W) and depth (D) dimensions were used as the control parameters to represent different aspect ratios of the designed cavities. It is important to note that the current approach by using 3 parameters (i.e. D, L, and W) provides a better insight into the defects evolution in three dimensions compared with the previous studies where cylindrical holes with two control parameters were used [37].



**Figure 3.3: Parameters used to describe the defect geometry**

The normal distribution of the defect dimensions presented in Figure 3.2 was used to identify three levels of the control parameters length (L) and width (W) of the cavities. The mean values for length (11mm) and width (7mm) were selected as a mid-value, then, a low and a high value for both length and width were selected ensuring that the 80% of the most frequent defect were considered. The area which accounts the 80% of the most common defect dimensions is highlighted in yellow in Figure 3.2. The low and high values of width chosen were 3mm and 11mm respectively. The length low and high values were chosen to be 4mm and 17mm respectively.

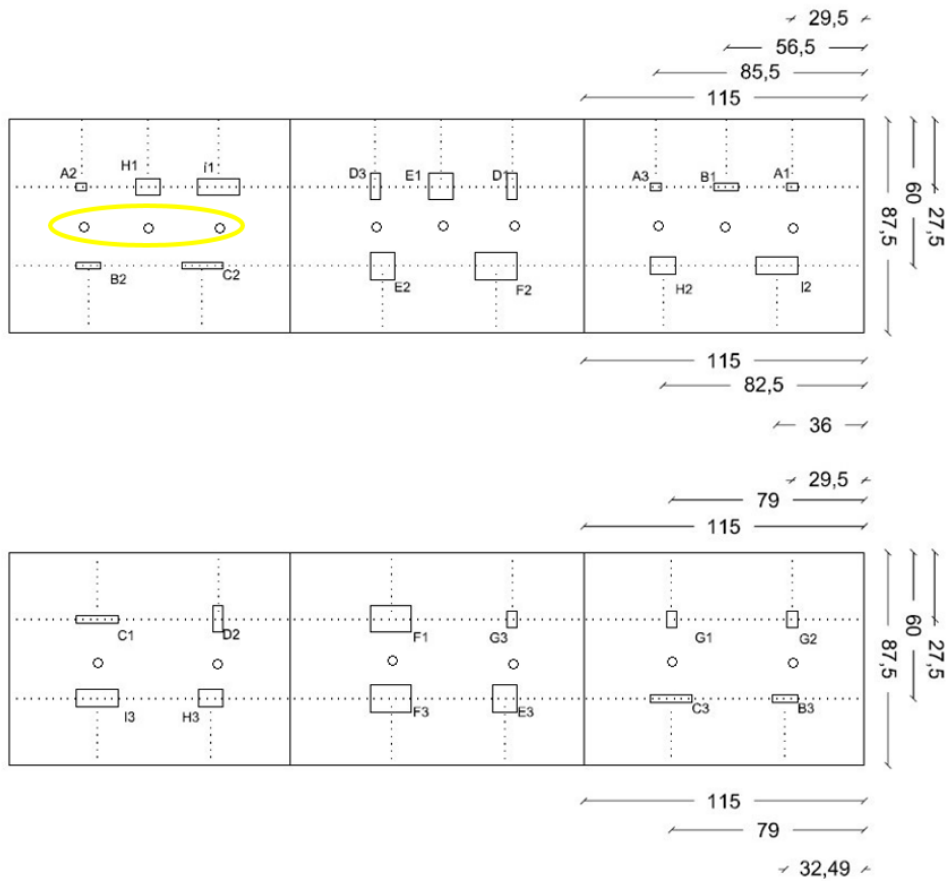
The analysis of the defect depths revealed a very small average depth value with only a few deep protrusions found in the slabs. Therefore, the largest measured values were used to ensure the worst case conditions have been considered. Hence, cavities with a depth value of 1mm, 3mm and 5mm were designed to represent the depth parameter (D). The designed defects with the associated parameters are shown in Table 3.1.

**Table 3.1: Cavity identification code list and corresponding dimensions**

DEFECT		A 1	B 1	C 1	D 1	E 1	F 1	G 1	H 1	I 1	A 2	B 2	C 2	D 2	E 2	F 2	G 2	H 2	I 2	A 3	B 3	C 3	D 3	E 3	F 3	G 3	H 3	I 3	
D (mm)	1	X	X	X	X	X	X	X	X	X																			
	3										X	X	X	X	X	X	X	X	X										
	5																			X	X	X	X	X	X	X	X	X	X
W (mm)	3	X	X	X							X	X	X							X	X	X							
	7							X	X	X							X	X	X							X	X	X	
	11				X	X	X							X	X	X							X	X	X				
L (mm)	4	X			X			X			X			X			X			X			X			X			
	10		X			X			X			X			X			X			X			X			X		
	17			X			X			X			X			X			X			X			X			X	

The cavities were positioned to maximise the distance between adjacent cavity boundaries and the block edges to minimise interactions between the deformation fields (Figure 3.4).

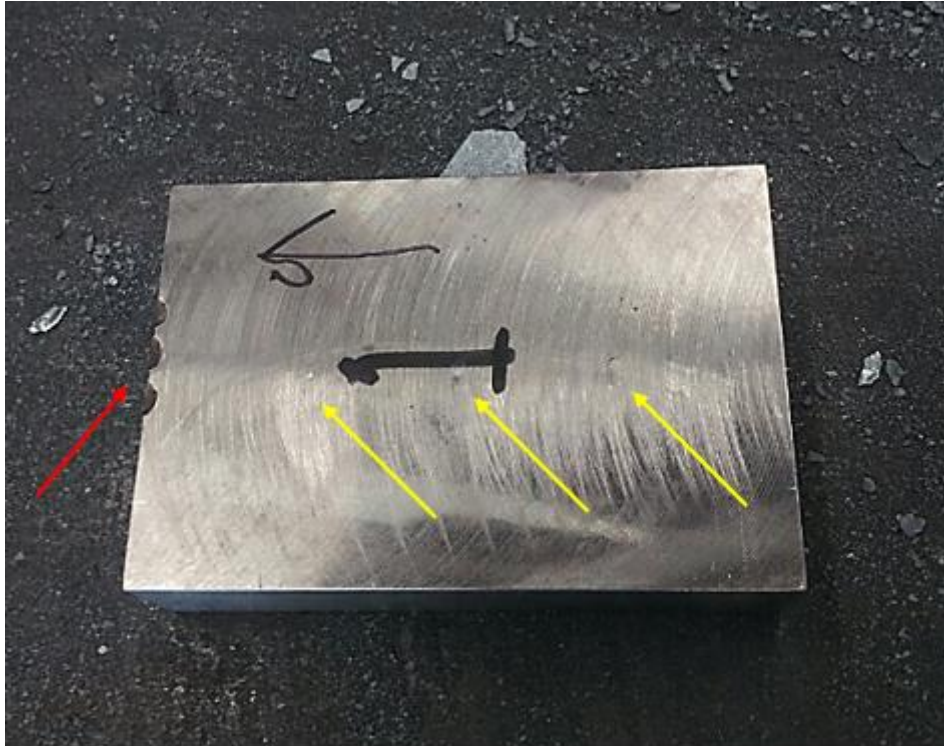
Stainless steel pins with a diameter of 3.5 mm and a length of 25mm were inserted in the centre plane of the slabs, to analyse the strain pattern in the rolling direction. Figure 3.4 shows the six slabs containing the cavities used for the experiment; three pins are highlighted.



**Figure 3.4: Machined defects on the surface of slabs before the hot rolling operation. Pins are highlighted in yellow.**

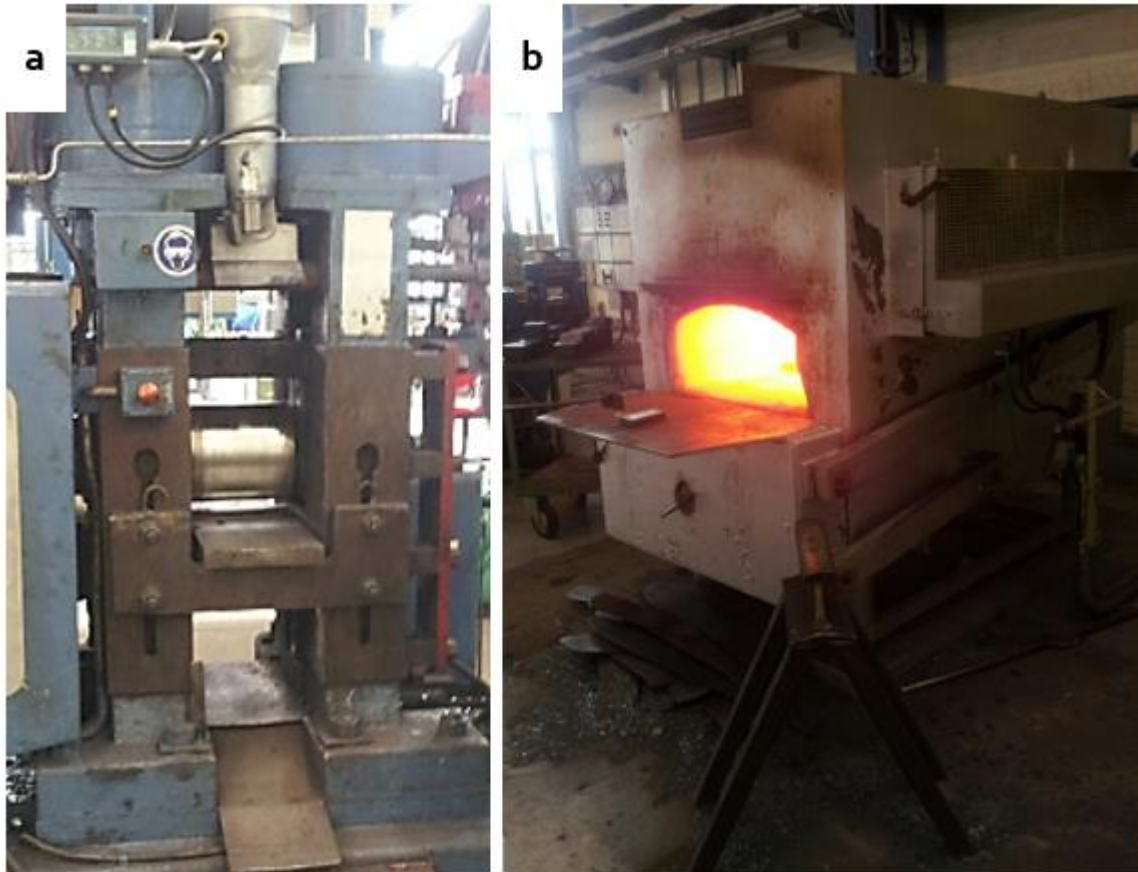
The remaining five slabs were only used to evaluate the strain pattern distortion of the inserts. Similar stainless pins used in the previous samples were inserted in the remaining 5 slabs. Figure 3.5 shows one of the specimens used for the experiment; three yellow arrows are used to identify the three pins inserted. The red arrow indicates the indentation created prior the rolling by the technicians to recognise the front side of the specimen after the heating:





**Figure 3.5: Non defected slab used to measure the strain distortion pattern; pins and front side are highlighted with yellow and red narrows respectively.**

A laboratory mill with roll diameters of 223mm (Figure 3.6a) was used to roll the samples after the heating. A muffle furnace capable of reaching temperatures of 1400°C placed in the close vicinity of the roll was also used to heat the samples (Figure 3.6b).



**Figure 3.6: Rolling mill (a) and furnace (b) used for the rolling experiment.**

The slabs containing cavities were heated in the muffle furnace at 1150 °C and held at this temperature for 15 minutes prior to the rolling process. This was to homogenise the temperature and to create a primary oxide scale on the surfaces. The slabs were then cooled down to 1050 °C through radiation to the environment to simulate the heat loss of the slab when it comes out of the furnace moving towards the roughing mill. Afterwards, the oxide layer was removed by a scraper before pushing the sections into the rolling gap in a laboratory mill with a 223mm roll diameter. The rolling operation was then performed at the velocity of 19 rpm to obtain a 40% thickness reduction in a single rolling pass.

The remaining five slabs with no cavities were heated at different temperatures in order to obtain different and controlled oxide thicknesses: Two slabs were heated at 1100 °C; one slab was heated at 1150 °C; the remaining two slabs were

heated at 1200 °C. Once the slabs reached the target temperature, they were held at the respective temperatures for 15 minutes to create a proper primary oxide scale and to homogenise the specimen temperature. The oxide scale was then removed by a scraper, and the slabs were cooled by radiation to the environment down to 100 °C lower than the heating temperature. This was done to reproduce the heat loss of the slab before the rolling. After the cooling, the test temperatures were 1000°C, 1050°C and 1100°C respectively.

All the slabs were then rolled with a velocity of 19 rot/min to a final gauge of 15 mm (40% of reduction) obtained with a single rolling pass and then cooled in air. The following table shows the matrix of the experiment carried out.

**Table 3.2: Hot rolling experiments carried out**

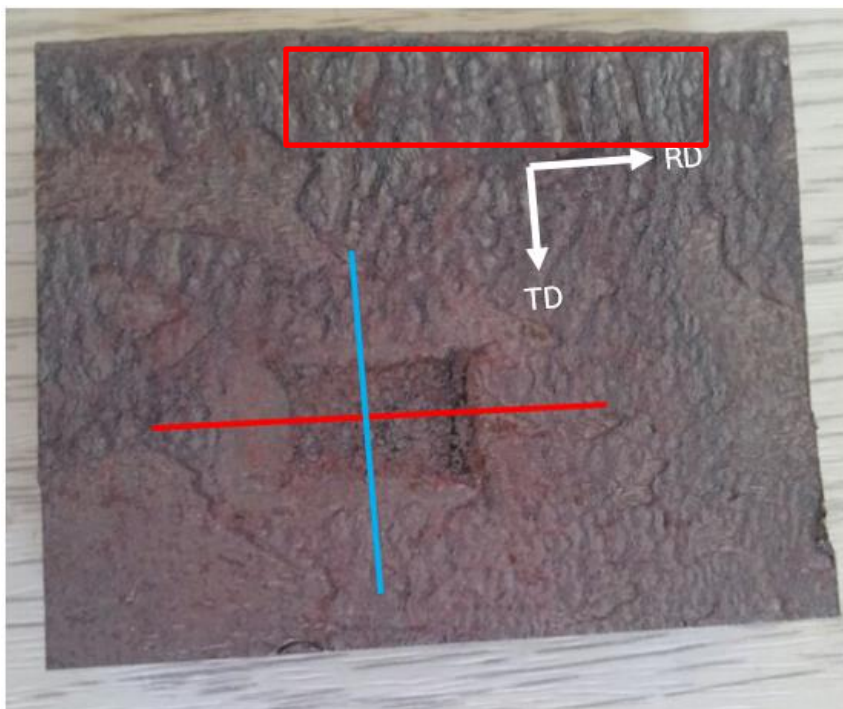
SAMPLE n°	HEATING TEMPERATURE (C°)	HEATING TEMPERATURE (C°)	SAMPLE SURFACE
1	1100	1000	SMOOTH
2	1100	1000	SMOOTH
3	1150	1050	SMOOTH
4	1150	1050	INDENTED
5	1150	1050	INDENTED
6	1150	1050	INDENTED
7	1150	1050	INDENTED
8	1150	1050	INDENTED
9	1150	1050	INDENTED
10	1200	1100	SMOOTH
11	1200	1100	SMOOTH

The term “cavity” will be used to refer to the artificial cavities machined into the slabs before rolling and “defect” will be used to refer to the deformed features after the rolling. The top surface of the rolled sections was analysed after the experiments to characterise final cavity geometries.

Metallurgical cross-sections of longitudinal and transversal profiles of the final defects were prepared in the laboratories of the University of Sheffield. To do this, the slabs were first cut in different sections containing the defects with an abrasive cutter.

A typical section of metal containing the defect obtained after cutting is presented in Figure 3.7. After the first sectioning, transversal and longitudinal

cross-sections of the defect were obtained with the precision cutter. The transversal sections were obtained first, this was done because there was more interest in having a full transversal section of the defect. The transverse and longitudinal sections cut are indicated in blue and red respectively in Figure 3.7. The sections were intentionally out of the centreline of the defect to take into account the successive wearing and consuming of the material during the grinding and polishing procedure. The presence of fractured oxide due to the slab elongation is highlighted in a red box.



**Figure 3.7: Transverse and longitudinal section scheme of one defect.**

Samples were then cold mounted with an epoxy resin followed by standard grinding and polishing procedure using 6 and 3 um diamond paste with a grinding-polishing machine. Similar procedure was carried out to prepare the samples of the deformed pins inserted in the slabs.

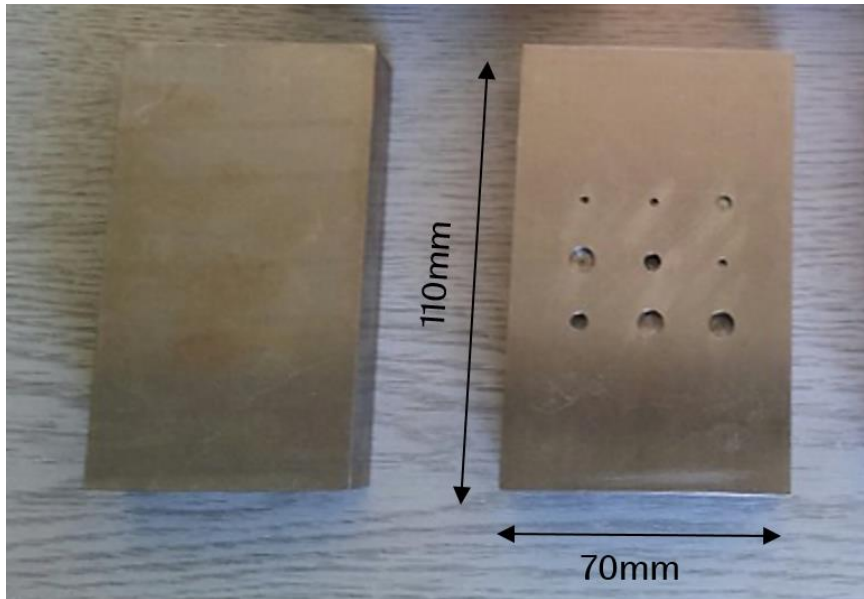
Samples were then analysed using a Nikon optical microscope to study the effects of the initial configuration on the deformed geometries and identify the most critical dimensional parameters.

In order to be able to conduct inverse calculation to calibrate the friction coefficient present during the experiment, a proper FEM model reproducing the experiment was developed (calibration is presented in chapter 5.4.2). Longitudinal strain distortion patterns of the models run at different frictional conditions were compared with the distorted pins. The friction coefficient of the models was adjusted until the strain pattern of the model matched the pin distorted pattern.

### **3.2 Descaling**

The descaling experiment was carried out in the laboratories of the Swinden Technology Centre (Rotherham) by means of a water spray descaler reproducing the descalers used in industry during hot rolling processes.

A total of 3 samples were obtained from cast slabs made of a Fe-3%Si content. Samples were 110 mm long, 26 mm thick and 70 mm wide. Holes of different depth to diameter aspect ratios were drilled in the surface of 2 slabs in order to check the effectiveness of the descaling inside them. This was important as the main cause of defect generation is the embedded oxide beneath the metal deformed surface after rolling, so, an analysis of the cavity after descaling is useful to obtain a further insight into the oxidation state of the cavity before the rolling. Three different diameters (6mm, 4mm, 2mm) and depths (6mm, 4mm, 2mm) were combined to obtain 9 different cylindrical holes. Figure 3.8 presents an example of the 2 different surface conditions of the samples:



**Figure 3.8: Slab condition before the test: milled slab (left side), slab containing cylindrical cavities (right side).**

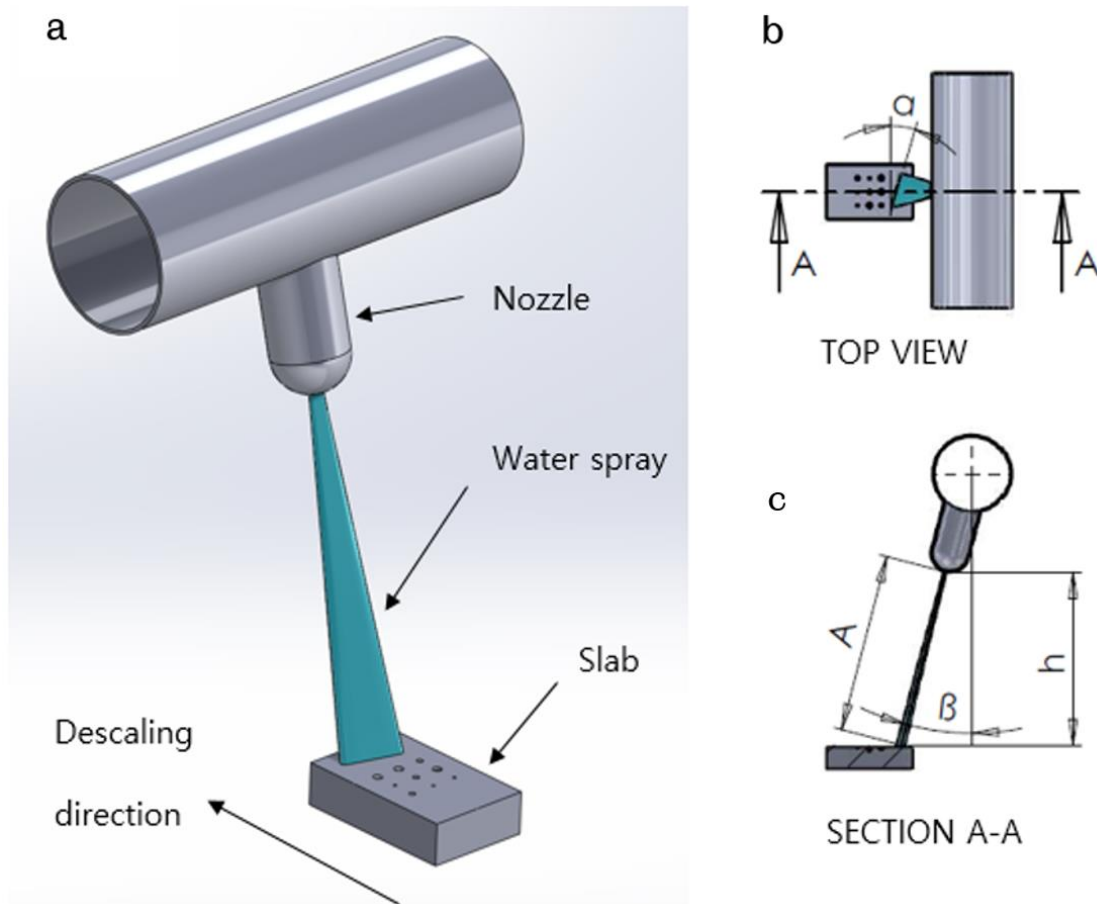
One single spray nozzle was used for the descaling test, Figure 3.9 shows the descaler used for the experiment (the nozzle is highlighted in yellow). The nozzle set up parameters were provided by the industrial partner to reproduce the descaling set up used in the production plant. The nozzle height ( $h$ ) was 93mm, the twist angle ( $\alpha$ ) was  $15^\circ$ , the standoff angle ( $\beta$ ) was  $30^\circ$ , slab velocity was fixed to 2.5 m/s, and flow rate pressure of 290 bar was applied.





**Figure 3.9: Descaler rig used to carry out the experiment.**

The slabs were positioned in such a way that only half of the slab was descaled. The non-descaled band was then used to estimate the oxide thickness before the descaling. Samples containing the drilled holes were positioned in order to guarantee the coverage of all the holes by the water spray. The Figure 3.10 shows a scheme of the descaling set-up and the slab positioning with respect to the water spray nozzle for a drilled slab.



**Figure 3.10: Descaling scheme used for the experiment, 3D view (a), top view (b), and longitudinal section (c).**

Specimens were reheated in air at 1150 °C, for about 40 minutes (oxygen was continuously monitored to make sure the percentage of the oxygen was about 18%), by means of an electrical furnace with controlled temperature and oxygen (Figure 3.11a), this was the time necessary for the slab to reach the target temperature of 1150°C. The oxygen content is an important parameter as it regulates the oxide growth during the heating. Once the slab reached the target temperature, it was held at that temperature for 40 minutes (to simulate the soaking of the slab on the tunnel furnace during the transport). During this period, primary oxide scales are formed. The two slab were then descaled and



slowly cooled in a box in argon environment preventing secondary oxide scale growth after the descaling (Figure 3.11right).

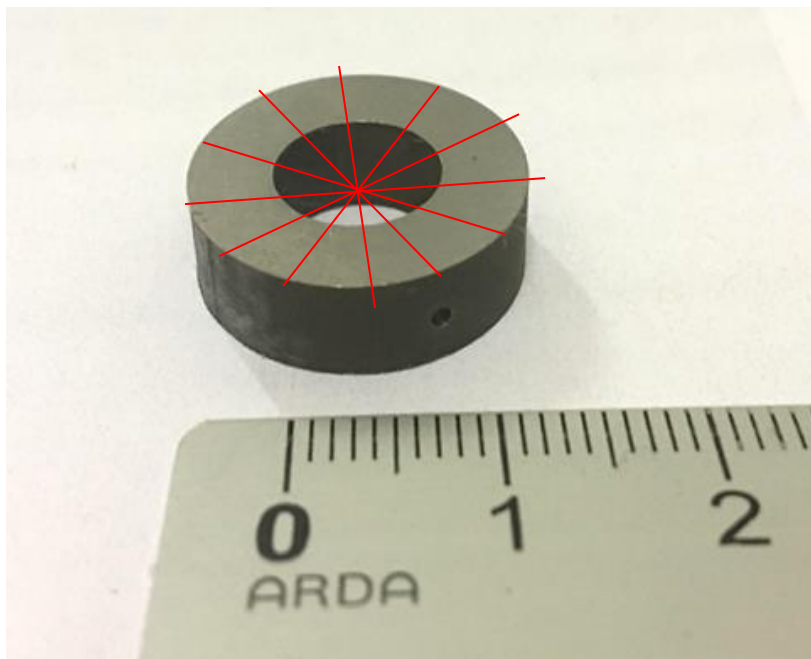


**Figure 3.11: Electrical oven (left side) and the box containing argon (right side) used for the heating and cooling of the slabs respectively.**

After the cooling in the argon box, slabs were cut in different transversal and longitudinal sections to evaluate the oxide thickness. The cylindrical holes were then sectioned longitudinally with the precision cutter machine in order to analyse the effect of the water spray descaling within them. Samples were prepared by cold mounting. This type of mounting is more suitable than hot mounting in this application because no pressures that could alter the oxide scale layer are applied during the preparation.

### 3.3 Isothermal hot ring compression

The Isothermal hot ring experiment was carried out to estimate the friction coefficient between slab and roll during rolling at different isothermal conditions. Ring samples were obtained from a transfer slab of 15 mm thick and were designed to respect the common dimensional ratios of 6:3:2 encountered in the literature [78]. An external diameter of 18 mm, an internal diameter of 9 mm, and a height of 6mm were obtained by machining; a small hole with a diameter of 1mm and depth of 2.5mm was radially drilled in each ring for the thermocouples allowing the temperature measurement during the experiment (Figure 3.12).



**Figure 3.12: Sample used for the ring compression test, and sections used to measure diameter variations (indicated in red)**

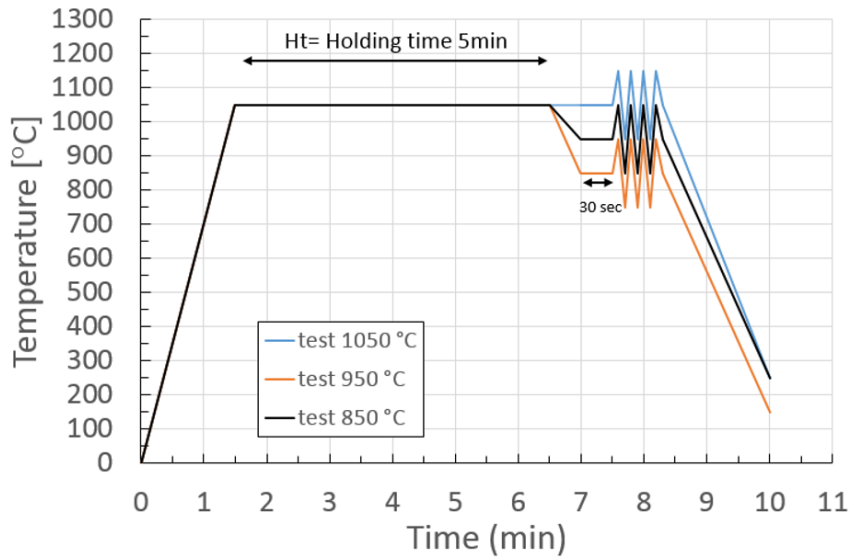
The experiment was performed using the thermomechanical compression machine (TMC) of the University of Sheffield (Figure 3.13).



**Figure 3.13: TMC machine used for the ring tests.**

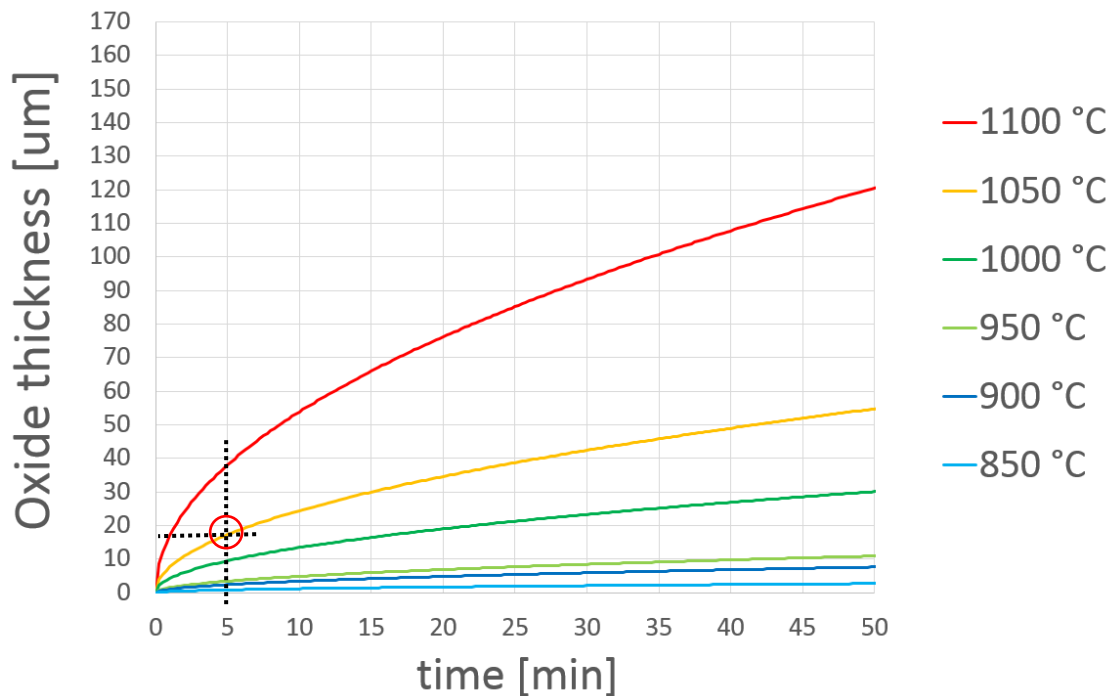
The samples were heated in a controlled environment using a controlled heating cycle to reproduce an oxide layer on the surface of the ring with the same thickness as the layers measured on the slabs subjected to descaling during the descaling experiment previously explained. The replication of the same oxide scale thickness for all the rings is essential for this experiment as friction coefficient is directly dependent on the oxide layer thickness, in fact, the surface oxide layer can act as a lubricant or increase the friction depending on the thickness and composition.

All the samples were heated at the same temperature of 1050 °C; a heating rate of about 10 °C/sec was arbitrarily chosen and guaranteed for all the samples tested during the heating through a continuous monitoring of the temperature of the ring. The oxide thickness target was  $15\mu\text{m} \pm 10\mu\text{m}$  and it represents the scale thickness present in the surface of the slabs after the water spray descaling. Oxide thickness evaluation was carried out through the descaling experiment explained in chapter 3.2; results are reported in chapter 4.7. The test timeline is presented in Figure 3.14.



**Figure 3.14: Heating and compression test timeline scheme used for the experiment.**

The holding time at 1050°C needed for the oxide to grow up to thickness target was obtained by following the oxide grown curves for a 3% electrical steel presented in [10]. Figure 3.15 shows the different oxide grow rates for different temperatures, they are obtained using the parabolic grow regime formulas provided in [10]. As shown, a holding time at 1050°C for 5 minutes generates a final oxide scale of about 15  $\mu\text{m}$ . Samples were subjected to this heat treatment before the experiment to check the final oxide scale thickness generated (results reported in 4.8.1).



**Figure 3.15: Oxide thickness growth rate at different temperatures for 3% Silicon Steel.**

Once the oxide was grown, the ring was cooled down to the test temperature and held again for 30 seconds to homogenise the temperature. Rings were then compressed at a strain rate of 1 s<sup>-1</sup> and cooled to room temperature by quenching in water, the strain rate value was chosen to be in the range of strain rates presents in the slabs in the contact zone during rolling. Three different test temperatures were used, the values were selected to cover the range of temperature of the slab surface in contact with the roll in steady state condition of hot rolling obtained from the simulations carried out to reproduce the process. The test temperature chosen were 1050°C, 950°C and 850°C.

All the tests were isothermal, which means that tools and rings had the same initial temperature. This was intentionally designed to avoid heat transfer between ring and slab, which would have affected the ring deformation behaviour and complicated the modelling of the system to obtain the calibration curves.

A total of 6 experimental conditions were considered at three different temperatures and two different reduction rates. The Table 3.3 shows the matrix of the experiment carried out:

**Table 3.3: Ring test matrix of the experiments**

test type	replications n°	ring / tools temperature °C	thickness reduction %	strain rate s <sup>-1</sup>
1	2	1050	50	1
2	2	1050	30	1
3	2	950	50	1
4	3	950	30	1
5	3	850	50	1
6	4	850	30	1

The final internal diameters and heights of the ring were then measured at 6 different locations (as indicated in Figure 3.12) and the average of the measured values was calculated. The calibration curves necessary to estimate the friction coefficient were obtained by means of modelling of the whole compression procedure. The model used is presented in Chapter 5.8.

### 3.4 Summary

The rolling experiments provided an insight into the effect of defect geometries on evolution and deformation mechanisms in the rolled products. The de-scaling experiments determined the scale thickness of the oxide present on the slab surface. Once the thickness was evaluated it was used as a reference for the ring compression test. An oxide scale with a similar thickness was growth on rings subjected to compression and the effect of temperature on friction coefficient was evaluated. The determination of the friction coefficient was required for the modelling of rolling operation that will be given in the following chapters.

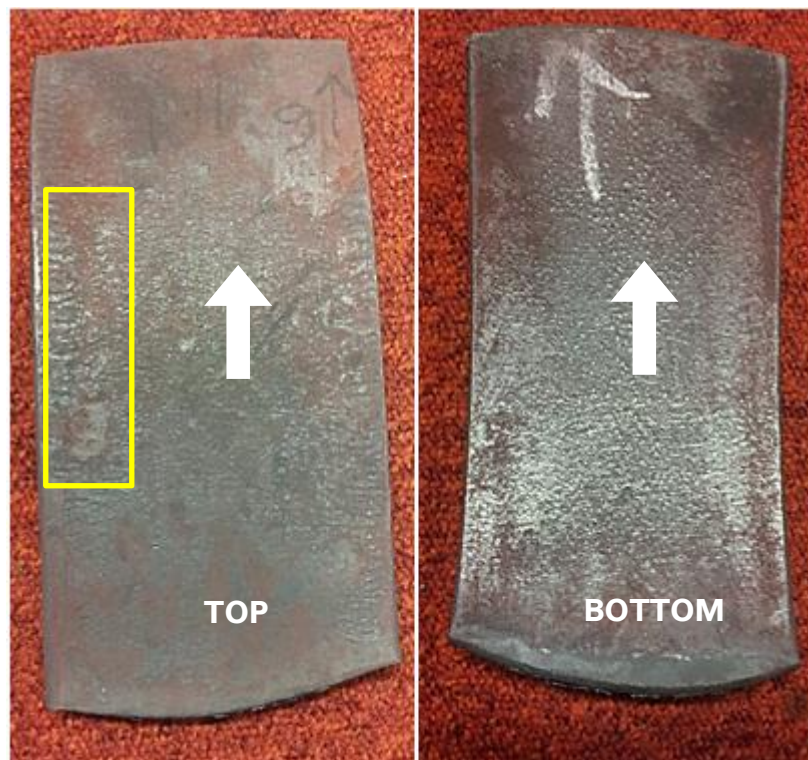


## 4 EXPERIMENTAL RESULTS

The present chapter focuses on the results of the three experiments carried out during the research study. The experiments are presented in separated subchapters.

### 4.1 Analysis of deformed defects geometries

The rolled slabs were visually inspected after the rolling and cooling of the slabs. In Figure 4.1, the top and the bottom surfaces of a slab (identified with respect to the position during heating) after the rolling are compared and the rolling direction is indicated by a white arrow:



**Figure 4.1: Typical top and bottom surface of a slab after the rolling.**


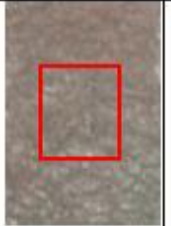





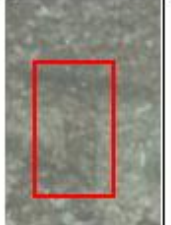





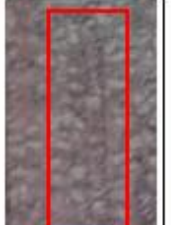










The top surface showed evidence of more oxidisation compared with the bottom surface that is noticeable by a change in colours and by the fracture of the oxide on the left side of the top slab as highlighted in Figure 4.1. The differences in oxide thickness are due to the heating procedure, in fact during the heating, slabs were leant on the furnace in horizontal position resulting in

less oxygen available for the bottom surface to be oxidised because of the direct contact with the bottom surface of the oven.

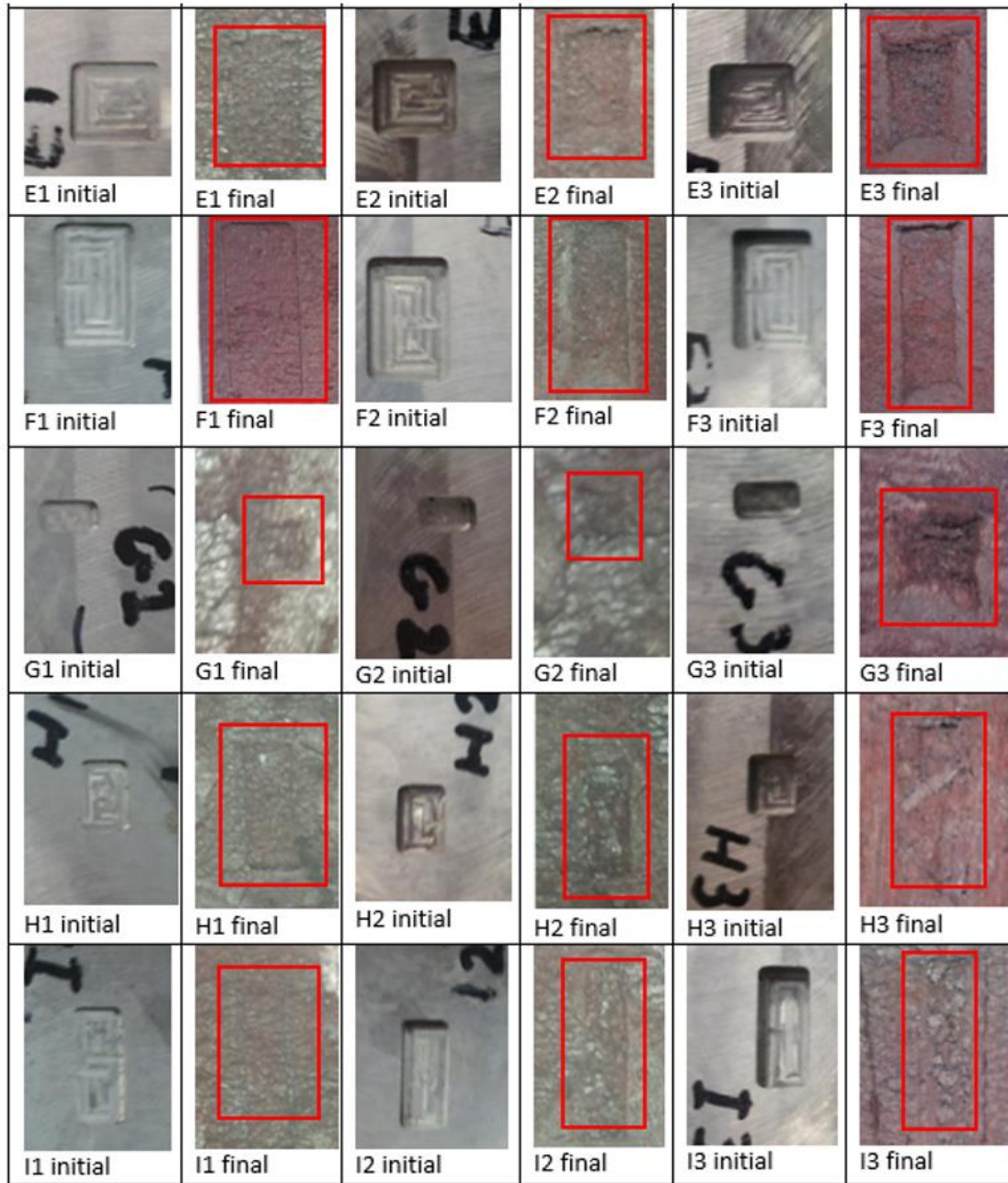
After the inspection, slabs were longitudinally cut and samples were prepared to study the final defects shape, the oxide thickness and the pin distortion patterns.

The defects were analysed to study their evolution mechanisms. A top view of the defects after rolling is presented and compared with the original cavities shape and size before the rolling in Figure 4.2. The arrow in top-left of Figure 4.2 indicates the rolling direction for all the images. In general, it is noticeable that defects were elongated and reduced in width as a result of the rolling operation, this can be observable comparing the initial cavities and the final defects from the top view in Figure 4.2.



Initial defect	Deformed defect	Initial defect	Deformed defect	Initial defect	Deformed defect
					
A1 initial	A1 final	A2 initial	A2 final	A3 initial	A3 final
					
B1 initial	B1 final	B2 initial	B2 final	B3 initial	B3 final
					
C1 initial	C1 final	C2 initial	C2 final	C3 initial	C3 final
					
D1 initial	D1 final	D2 initial	D2 final	D3 initial	D3 final

**Figure 4.2 part one: Optical photographs of the cavities and deformed defects (highlighted by red rectangles) on the surface of the rolled slabs.**

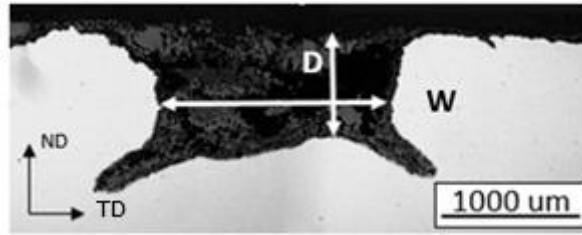


10mm

**Figure 4.2 part 2: Optical photographs of the cavities and deformed defects (highlighted by red rectangles) on the surface of the rolled slabs.**

The length of the rolled defects was measured directly from the surface of the rolled blocks with a calliper while the depth and the width were measured from the micrographs of each defect in the transverse cross-section after the rolling

operation. Figure 4.3 present the schematic of the measurements used for the defect measurement of the final depth and width.



**Figure 4.3: Depth and width measurement scheme**

The depth was measured at the shallowest point and the width measurement was taken from the narrowest section of the oxide-filled deformed defect.

The summary of the measured values for different initial machined cavities is shown in Table 4.1.

**Table 4.1: Cavity dimensions before and after rolling.**

Defect number		A1	B1	C1	D1	E1	F1	G1	H1	I1	A2	B2	C2	D2	E2	F2	G2	H2	I2	A3	B3	C3	D3	E3	F3	G3	H3	I3
Length L (mm)	final	4.5	15	27	7	15	26	6	15	26	4	14	26	6	13.5	27.5	4.5	15	27	6	15	25	4	15	25	4.5	15	24.5
	initial	4	10	17	4	10	17	4	10	17	4	10	17	4	10	17	4	10	17	4	10	17	4	10	17	4	10	17
Width W (mm)	final	2	1.6	1.5	9.8	9.5	9.6	6	7.3	6.6	1.6	1.74	1.26	9	9.33	9.1	5.7	5.8	5.65	1.09	0.79	0.88	8.1	7.3	8.5	3.8	3.76	3.4
	initial	3	3	3	11	11	11	7	7	7	3	3	3	11	11	11	7	7	7	3	3	3	11	11	11	7	7	7
Depth D (mm)	final	0.46	0.48	0.3	0.05	0.08	0.06	0.33	0.24	0.29	0.86	0.87	0.67	0.45	0.32	0.27	0.55	0.66	0.5	1.93	1.88	1.88	0.74	0.4	0.3	0.9	0.7	0.65
	initial	1	1	1	1	1	1	1	1	1	3	3	3	3	3	3	3	3	3	5	5	5	5	5	5	5	5	5

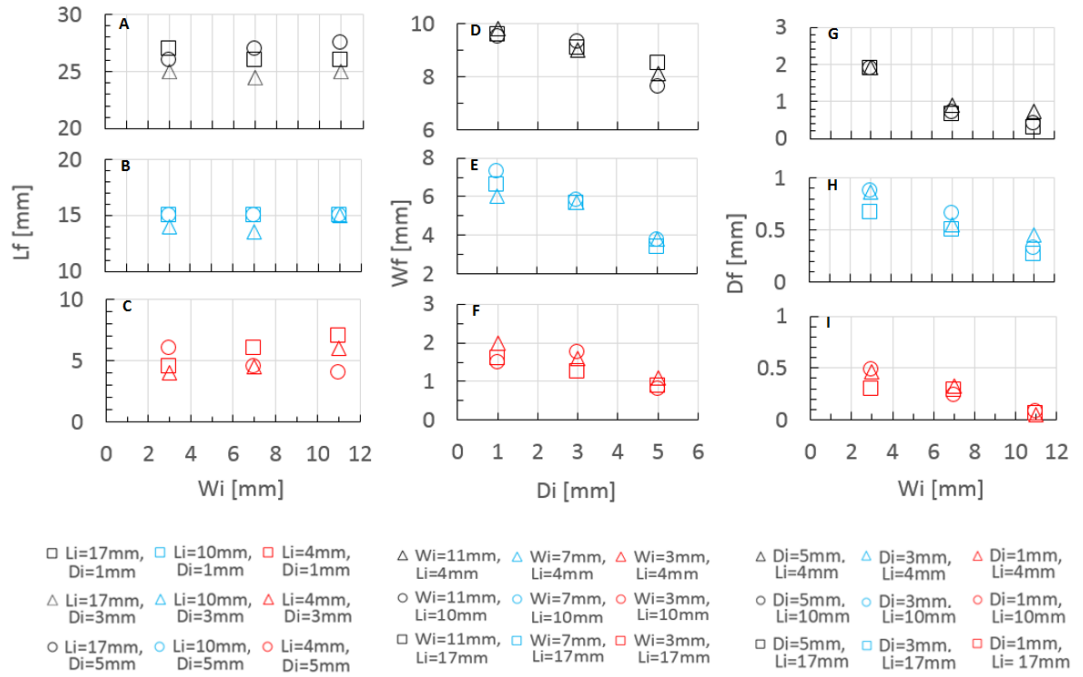
It is worth noting that similar elongation was observed for defects with different initial width or depth values and same initial length, e.g. defects C1 and I2, or G2 and G3. It has been observed that for a constant initial depth (A3, B3, C3, D3, E3, F3) the wider defects (D3, E3, F3) evolve to the shallower deformed cavity and deeper defects are formed when the cavities are narrower. Initial surface

defects with a depth of 1mm were almost flattened during the process (D1, E1, F1).

To better appreciate the relations between initial and final defect dimensions, the measurement of the length, width and depth of defects are graphically presented in Figure 4.4, where  $W_i$ ,  $L_i$ ,  $D_i$  indicate the initial width, length and depth respectively. Selected final lengths (Figure 4.4a-c) of the cavities are colour coded with black, blue, and red representing defects with an initial length of 17mm, 10 mm and 4 mm, respectively. The selected depths of each set of defects are indicated by markers with different geometries. Similar conventions are used in Figure 4.4d-f and Figure 4.4g-l to present the final width and depth, respectively.

According to Figure 4.4, the cavities were elongated in the rolling direction (Figure 4.4a-c) and reduced in depth (Figure 4.4g-i) and width (Figure 4.4d-f) after the rolling operation, as it was expected. The initial length was found to be the main geometrical parameter that affects the elongation of the surface cavities, for the given reduction ratio. This is because most of the reduction in thickness is converted in slab elongation considering the reduced spread of the material in the central zone of the slab where the cavities were machined. In fact, cavities with different depth and width and equal length (Figure 4.4a-c) show similar elongation due to the rolling induced plastic deformation.

With regards to the depth analysis (Figure 4.4g-i), it is worth to notice that for a given initial depth (indicated by different colours), the wider cavities evolve to shallower final defects (Figure 4.4g-i). It was also observed that cavities with depth of 1mm were almost completely flattened during the process for cavities wider than 3mm. This was regardless of the initial length of the surface cavities and it was more pronounced for wider initial features (Figure 4.4i). The dark colour within surface features D3, F3, A3 (Figure 4.2) are due to the presence of thicker oxide layers inside the cavities compared with the oxide layer present on the flat surface of the rolled sections.



**Figure 4.4: Graphical representation of the defects dimensions after rolling for different initial cavities.**

## 4.2 Crevice formation behaviour

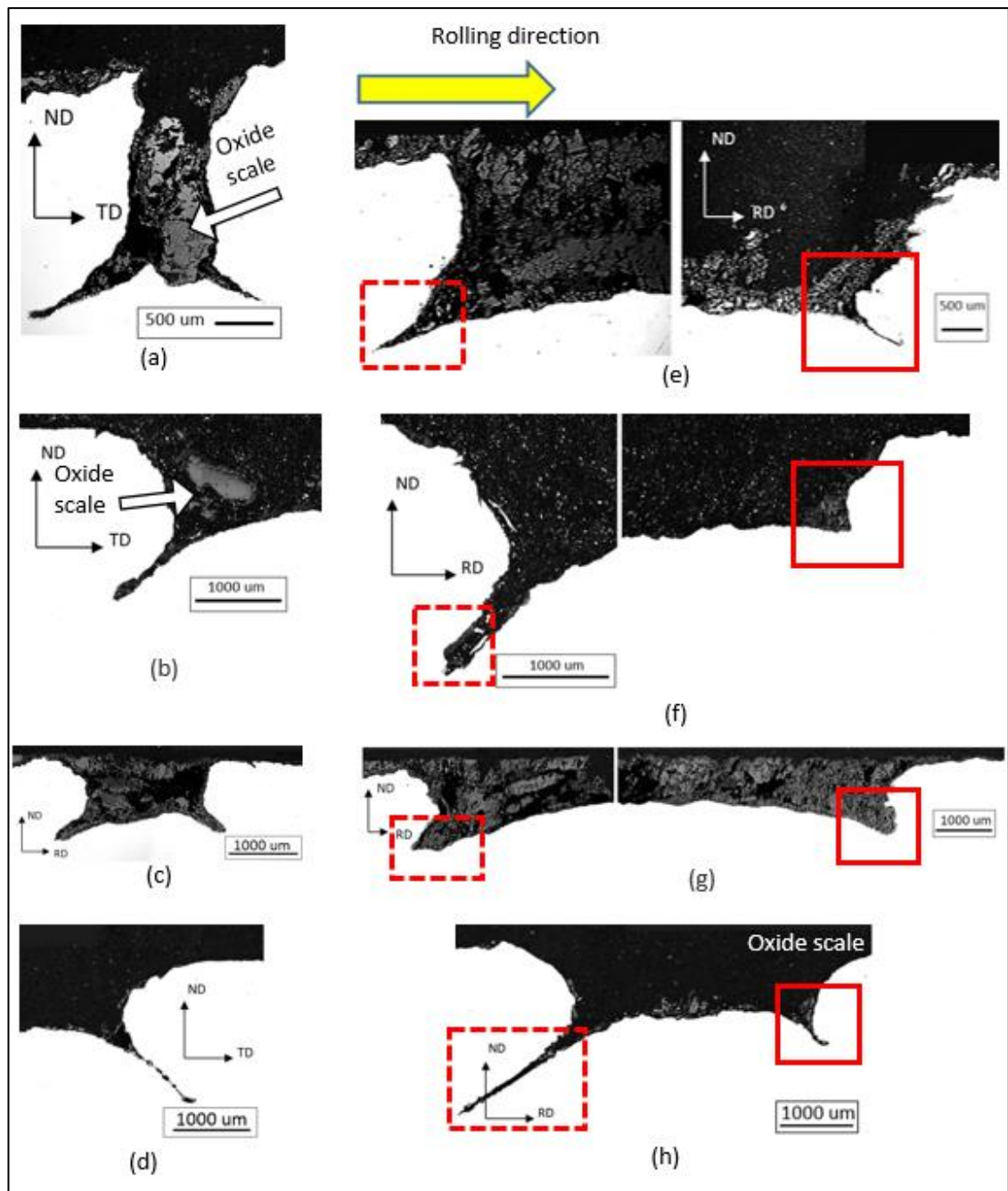
Micrographs of the defects showing the most representative deformation trends (B3, D3, B2, and G3) in the longitudinal and transverse cross-sections are presented in Figure 4.5. The micrographs considered are used as a tool to explain the defect evolution mechanisms in the next chapter. Similar behaviour was observed for all the 27 defects analysed and a complete table of all the micrographs obtained is presented in appendix 1.

Micrographs of Figure 4.5a-d show the transverse section of the defects, while the micrographs of Figure 4.5e-h show the longitudinal cross-section of the same defects. The rolling direction is indicated by the arrow in Figure 4.5e. The defects were found to be partially or completely filled with oxide. The differences are due to the fact that part of the oxide may have fallen out during the preparation and/or handling of the rolled slabs. In fact, even if a precision cutter was used for the sectioning, portions of oxide may have been broken or wore out during the preparation due to the fragile nature of the oxide or due to the pressure of the coolant fluid during the cutting.

The micrographs of the transversal sections show a lateral deformation in the transverse direction together with the buckling of the side walls resulting in substantial width reduction of the cavities, this is noticeable from all the transversal sections of the defects presented.

The micrographs of longitudinal cross-sections show that the back side of the defects (i.e. the last side to exit the rolling gap), as it is highlighted by the broken line at the left-hand side of the figures, are folded followed by excessive buckling due to the friction between the roll and the strip surface. As a result, the remaining oxide scales were entrapped in the crevice formed. On the other hand, the flow of material, as a result of the regions leaving the roll gap, generates further opening of the cavities at the front side shown by the highlighted feature with a solid line. This is sometimes associated with the generation of minor crevices as highlighted by the continuous lines (Figure 4.5e and Figure 4.5h).





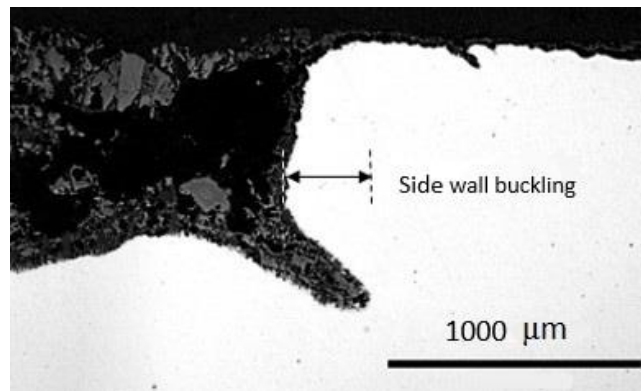
**Figure 4.5: Micrographs of selected defects B3 (a, e), D3 (b, f), B2 (c, g) and G2 (d, h) showing the deformed geometry at the transversal and longitudinal sections as indicated by the respective arrows.**

Micrographs of defects B3 and B2 in Figure 4.5 with initial depths of 5mm and 3mm, respectively, and a width of 3mm, show that cavities with a shallower initial depth show a reduced tendency to create crevices. Conversely, these crevices are more extended for deeper initial cavities (B3 in Figure 4.5). The presence of the crevices is noticeable in both the transversal and longitudinal sections. The

micrographs (Figure 4.5a,c, and g) show that although a scraping technique was used to remove the oxide layer before the rolling operation, there were some oxide scales left inside the cavities (highlighted by white arrows in Figure 4.5).

### 4.3 Deformation severity analysis: side wall buckling

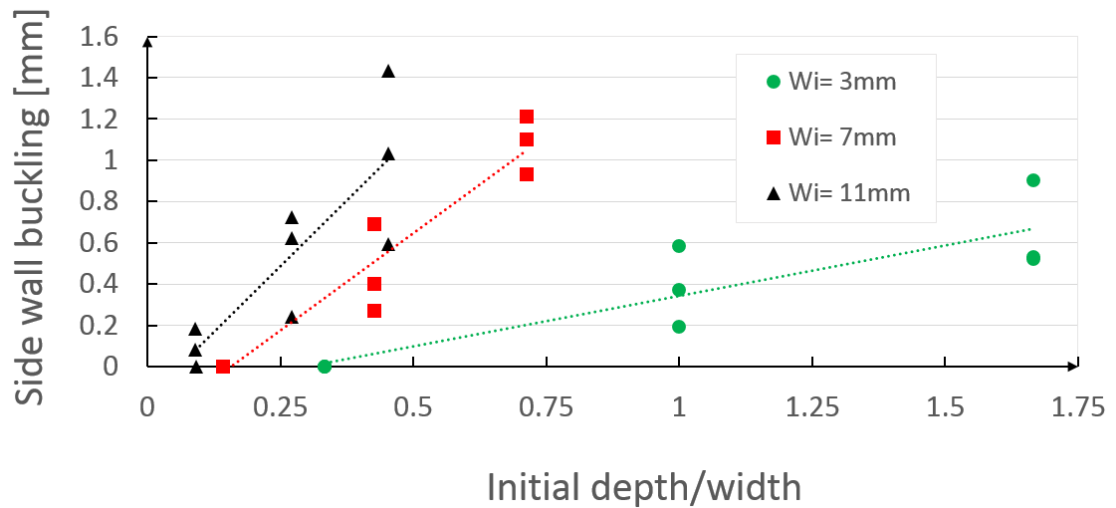
As previously explained, the residuals of oxide scales are buried under the deformed sides' walls of the metal of the cavities. The amount of oxide buried depends on the severity of the buckling of the lateral sides of the cavity. Consequently, the lateral deflection of the side walls, as indicated in Figure 4.6, can be used as an index to assess the severity of the deformation. This is aligned with the observed deformation behaviour for the cavities with smaller initial depth where a negligible buckling or a complete opening occurs, due to the rolling induced deformation.



**Figure 4.6: Buckling deformation measurement**

Figure 4.7 presents the measured side wall deflections in order to assess the severity of deformation in the analysed defects. Selected initial widths of the cavities are colour coded with black, red and green representing defects with an initial width of 11mm, 7mm and 3mm, respectively. The measured values show that, for a given initial width, the buckling effect increases with the  $D/W$  aspect ratio. In addition, observing the different slopes indicated by the dashed lines representing the trend lines, it is noticeable that the side wall buckling is more sensitive to the initial aspect ratio for wider cavities, in fact, the slope of the trend line increases with the initial width of the cavity.

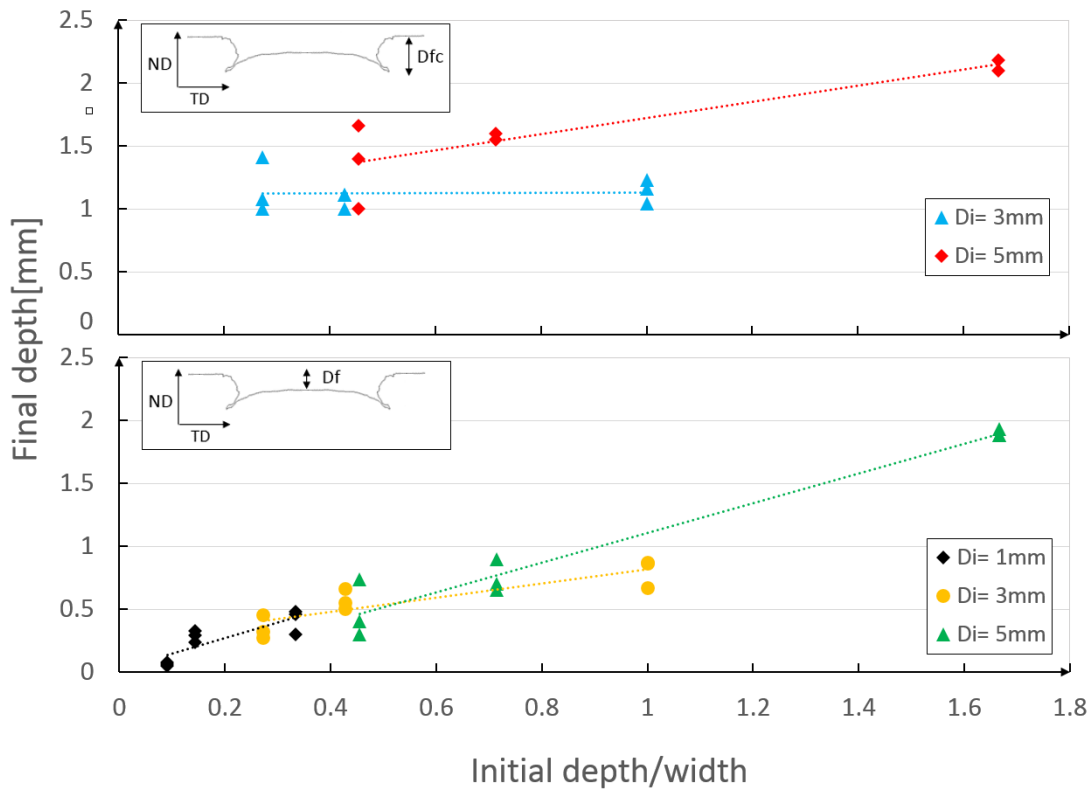




**Figure 4.7: Buckling effect measured for different initial depth/ width (D/W) aspect ratio and initial width (W).**

The final depth of the defects can also be used as an index of defect severity as deeper defects are harder to be eliminated and tend to bury more oxide residuals. To better describe the effect of the initial geometry on the final depth of the defect, it is important to take into account the measured values of depth taken at the shallowest point of the defect as well as the measured values of depth taken at the corners of the defect's crevices. Figure 4.8 presents the final depth measured at the crevice corners ( $D_{fc}$ ), where the red and blue colours representing defects with an initial depth of 5mm and 3mm. In the case of the measured final depth at the shallowest point ( $D_f$ ), black, yellow and green figures represent defects with an initial depth of 1mm and 3mm and 5mm; measurements are presented for different initial D/W aspect ratio.

The graph shows that the depth measured increase linearly with the initial depth to width aspect ratio for the both measurement criteria adopted. In addition, it is observable that this effect is more evident when the depth is measured at the shallower point of the bottom surface.

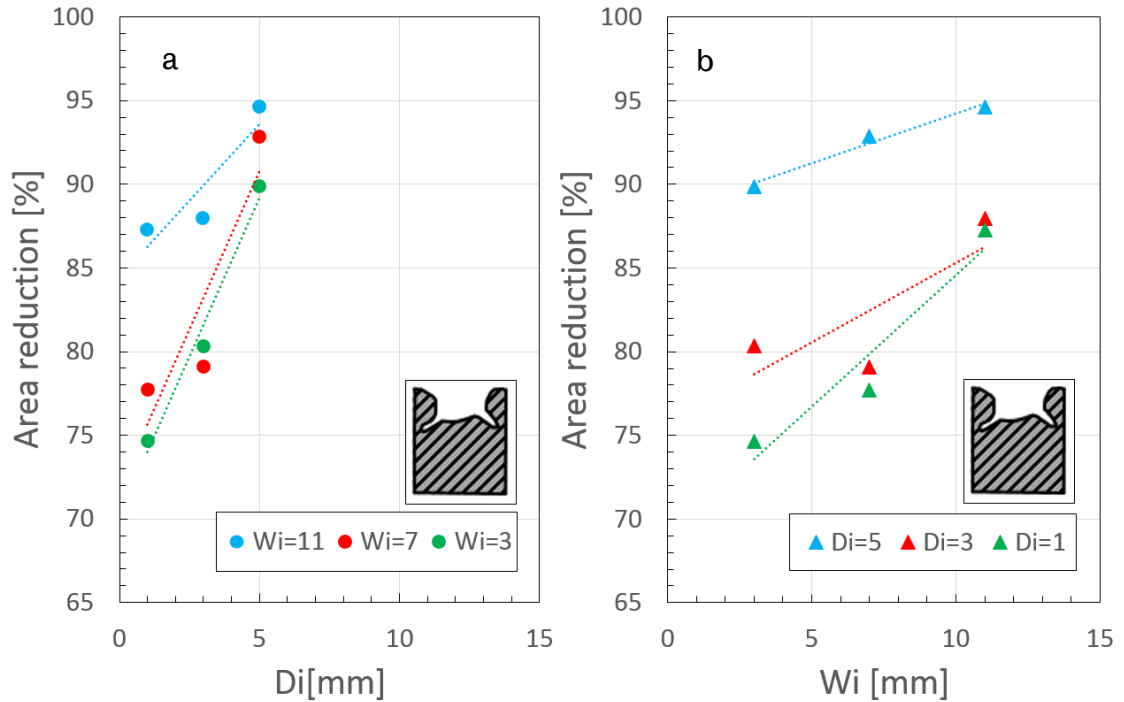


**Figure 4.8: Final defect depth for different initial depth/width ratios and respective trend line.**

#### 4.4 Deformation severity analysis: defect area reduction

The reduction of the cavity area is another indication of deformation experienced by the cavities during rolling. This is calculated as the ratio between the difference in transversal area before and after the deformation, and the initial transversal section area. Figure 4.9 shows the percentage of cross-sectional area reduction of the cavities made with the same initial widths and different initial depths (Figure 4.9a) and for cavities made with the same initial depths and different initial widths (Figure 4.9b). Different coloured markers are used to show the selected values for the initial widths ( $W_i$ ) and initial depth ( $D_i$ ) of the cavities. The graphs presented in Figure 4.9 show that the percentage of area reduction is higher for deeper and wider initial cavities. In particular, for a give initial width of the cavities, the percentage of area reduction increases with the cavity depth (Figure 4.9a). Similar results are found for cavities with same

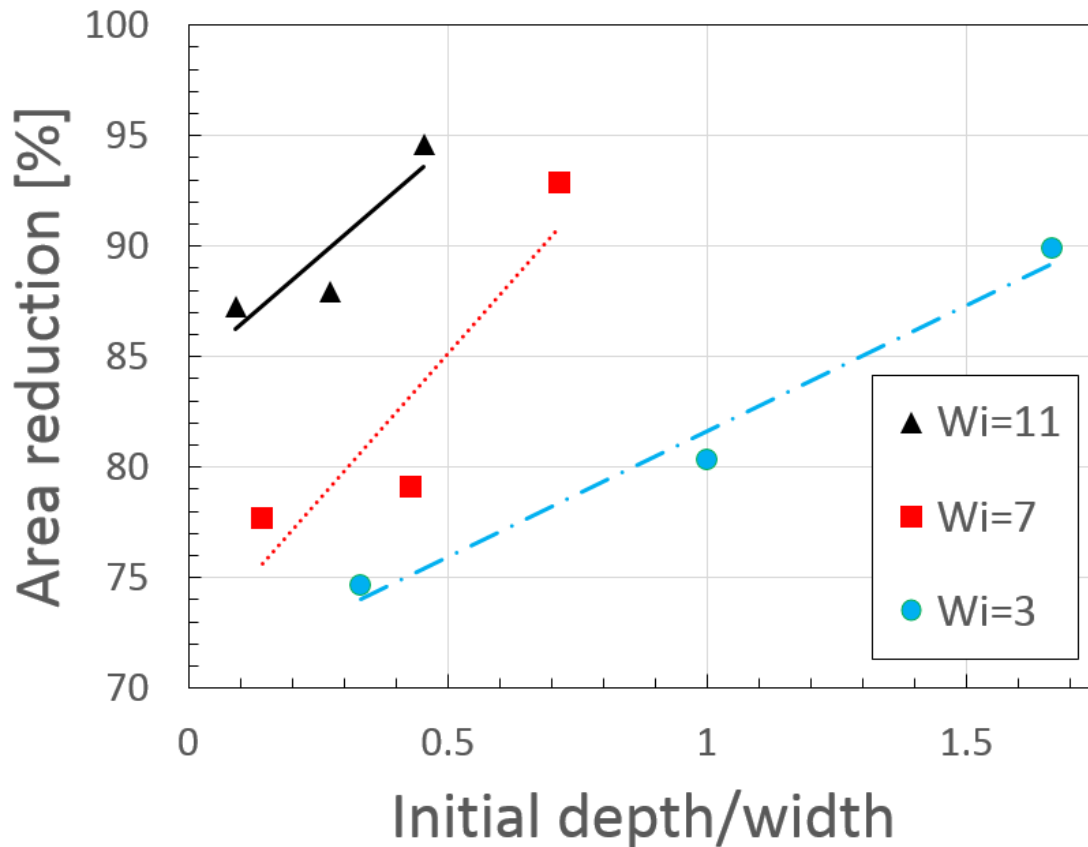
initial depth, they are more reduced in cross-sectional area when wider (Figure 4.9b). The graphs of Figure 4.9 clearly indicates that the percentage of area reduction is more sensitive to variations of the initial depth than variations of the initial width. This is noticeable comparing the different slopes of the trend lines of the two graphs.



**Figure 4.9: Percentage cross-sectional area reduction of the cavities during the rolling for different initial widths and depths and the mean value of length.**

Additionally, for the given initial widths, the percentage of area reduction increases with the D/W aspect ratio as shown in Figure 4.10 where defects with different initial width are presented with different colours and symbols. The slope is larger for wider initial cavities, it means that for a given change of initial D/W aspect ratio, more difference in reduction in area is encountered for wider initial cavities. In fact, a variation of about 0.5 in the D/W aspect ratio, results in an area reduction variation of about 10% for the cavities made with an initial width of 11mm (from 85% to 95%), and an area variation of about 6% for the cavities made with and initial width of 3mm (70% to 75%).

Similar results are found for the buckling effect presented in Figure 4.7, where the buckling is found to be more pronounced for wider initial defects.

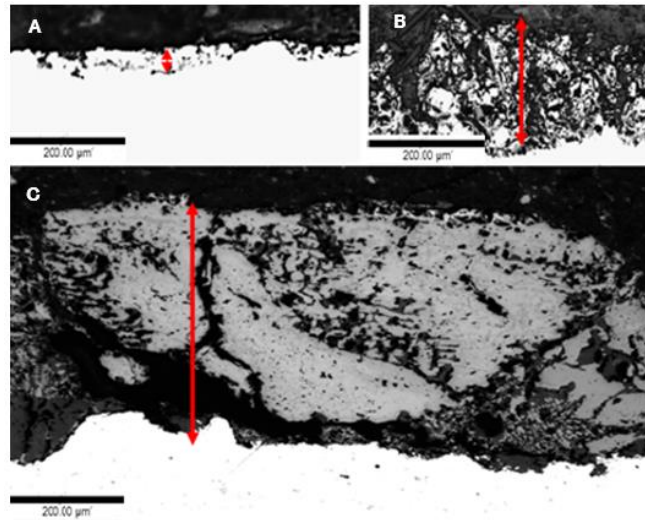


**Figure 4.10: Percentage cross-sectional area reduction for different initial D/W aspect ratio and initial W.**

#### 4.5 Longitudinal displacement measurement

Slab heated and rolled at three different temperatures were analysed after rolling to check the effect of different oxide thickness on the displacement pattern of the slab subjected to rolling, this was done to verify if there is any possible dependence of the friction on the oxide thickness. Figure 4.11 presents three micrographs of the slabs after rolling, heated and rolled at three different temperatures, oxide scale thickness is highlighted with a red arrow. After the heating, a scraper was used to remove as much oxide as possible. However, after the rolling, remarkable differences in thickness were observed. As the temperatures of the slab surfaces after rolling are lower than 900°C, (at this temperatures the oxide grows very slower compared to higher temperatures) the large oxide scale differences cannot be due to secondary oxide growth. Slabs

heated at higher temperature presented thicker final oxide layers because of the higher rates of oxide growth at higher temperatures. The scales were found harder to be scraped, in fact, their final oxide thickness was found very thicker compared to the scales formed at lower temperatures. Slabs heated at 1200 °C, 1150 °C and 1100 °C presented oxide thicknesses of about 40 μm, 230 μm and 450 μm respectively after rolling.



**Figure 4.11: Oxide profile present on the slab surfaces after the rolling for different initial heating temperatures: A, B and C represent the slabs heated at 1200°C, 1150°C and 1100°C respectively (oxide thickness is highlighted with red arrows).**

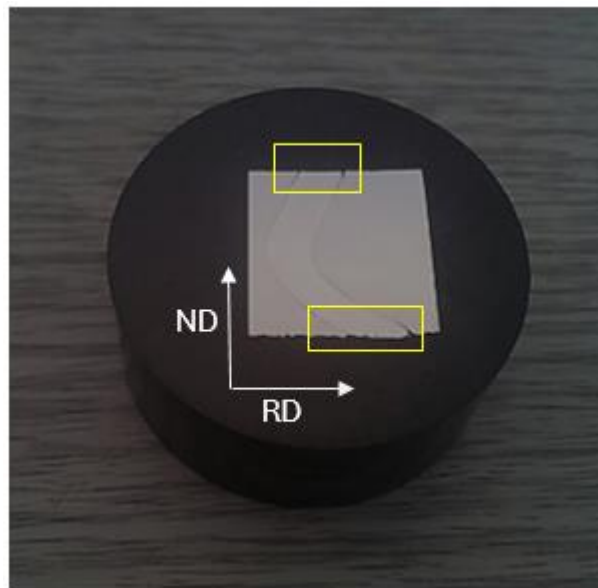
Oxide scale thickness ranges measured on the surface of the slabs after the rolling and cooling are presented in Table 4.2 for different initial and rolling temperatures:

**Table 4.2: Scale thickness measured in slabs heated and rolled at different initial temperatures.**

Heating temperature	Rolling temperature	Oxide scale thickness ranges encountered		
		0 μm	< thickness <	25 μm
1100°C	1000°C	0 μm	< thickness <	25 μm
1150°C	1050°C	80 μm	< thickness <	200 μm
1200°C	1100°C	150 μm	< thickness <	500 μm

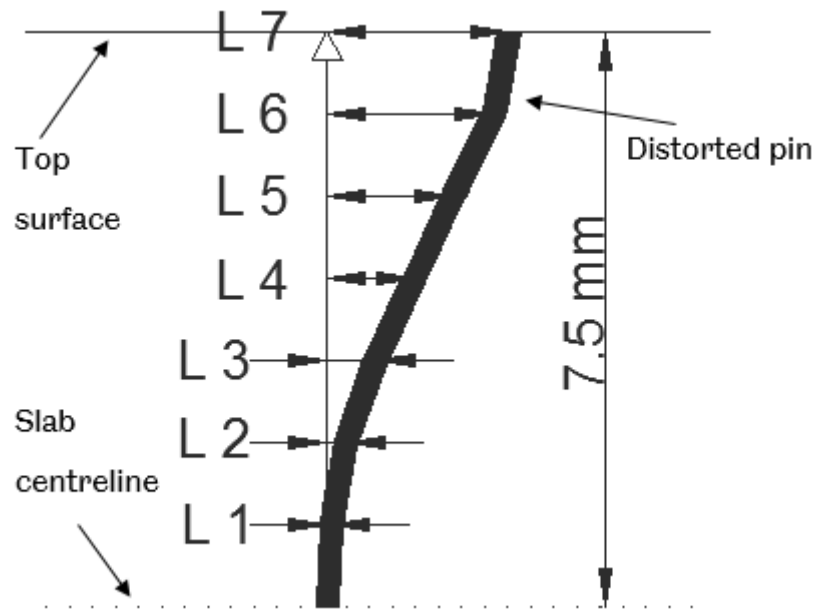
## 4.6 Quantification of longitudinal displacements

For the purpose of longitudinal displacement measurements, slabs were carefully cut at the mid-plane of the pins and samples obtained from the cut were ground to reveal the pin pattern after the rolling procedure. A small gap between pins and slabs was observed at the ends of the pins (highlighted in Figure 4.12), this is due to the fact that different materials were used for the insert and consequently different mechanical properties and relative deformations were experienced between pins and housing. However, the gaps are not considered critical because they were localised at the ends of the pins only. Figure 4.12 illustrates a typical sample containing a distorted pin after the grinding and polishing of the surface.



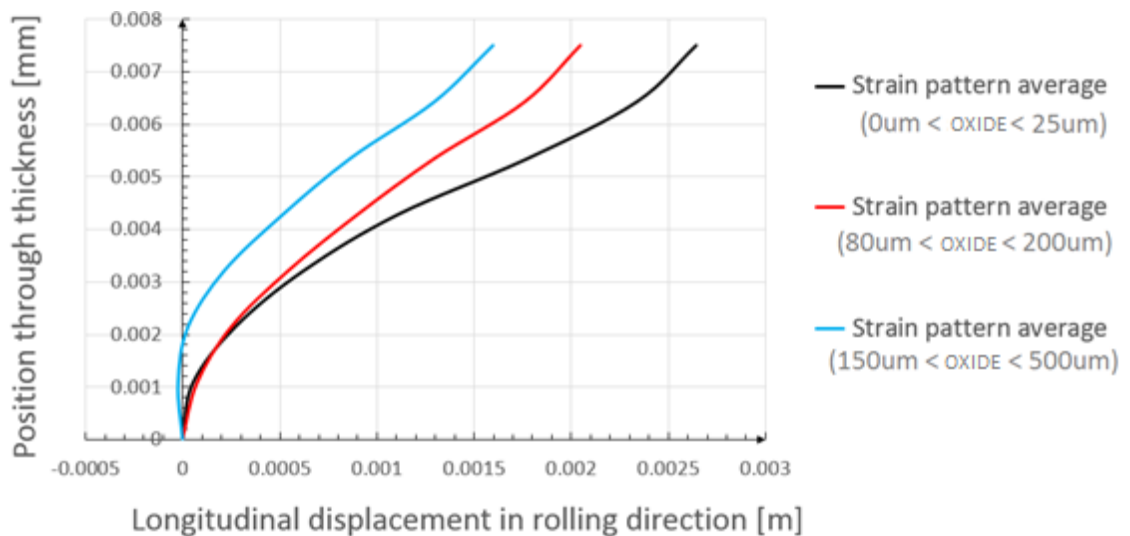
**Figure 4.12: Example of a distorted pin after the rolling.**

The pin distortion patterns were measured and compared, the analysis focuses on the top half of the slab as defects were milled on this side only. The longitudinal relative displacement with respect to the centre of the pin was measured at 7 different pin positions, the measurement scheme is reported in Figure 4.13:



**Figure 4.13: Pin measurement scheme after rolling.**

The average of the longitudinal displacement measurements taken at different positions is presented in the Figure 4.14 for different slab oxide scale thicknesses:



**Figure 4.14: Pin distortion pattern for different heating temperature of the slabs**

It is worth to notice that slabs heated and rolled at lower temperatures (where thinner oxide layers were present) resulted in higher distortion of the pins. In

fact, at the extremities of the pins, longitudinal displacements of about 1.5 mm and 2.5 mm were observed for slabs heated at 1200°C and 1100 °C respectively. Therefore, there is a dependence between oxide thickness and longitudinal displacement measured. In particular, the longitudinal displacement decrease with the scale thickness present on the surface of the slab. As more friction is expected to lead to a higher longitudinal distortion, it is correct to assume that the friction coefficient decrease with the oxide thickness. Further details about the pin distortion analysis are presented in appendix 2.

Slab heated at 1200°C shows a very small negative position of the longitudinal strain, this is due to a slight difference in friction between the bottom of the slab and the top.

#### **4.7 Analysis of oxide layer thickness due to the descaling process**

Considering the strong dependence of friction on the oxide scale present, it was considered necessary to determine the precise oxide scale thickness present during the industrial rolling process. This was done taking several measures of the oxide thickness in different sections of the slab surface. In this case, the oxide estimation carried out was based on a descaling set-up of a specific hot rolling industrial process of silicon steel.

**The oxide scale before the descaling was estimated from the non-descaled band oxide scales, whose thickness was measured in locations of the slab that were not covered by the water spray (as lateral sides or bottom of the slabs).**

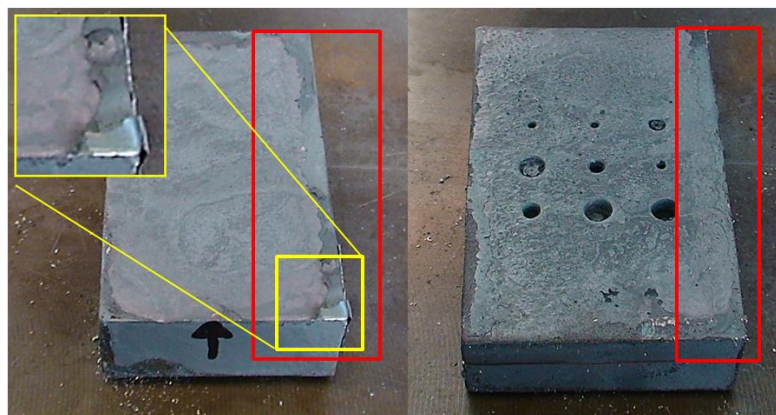
Table 4.3 reports the oxide thickness measurement taken at different points of the surface of the milled surface slab and the slab surface containing cylindrical holes. It is worth to note that negligible differences in oxide thickness were encountered between the slabs surfaces containing holes and the flat surfaces as expected.



**Table 4.3: Oxide thickness measurements taken for all the conditions**

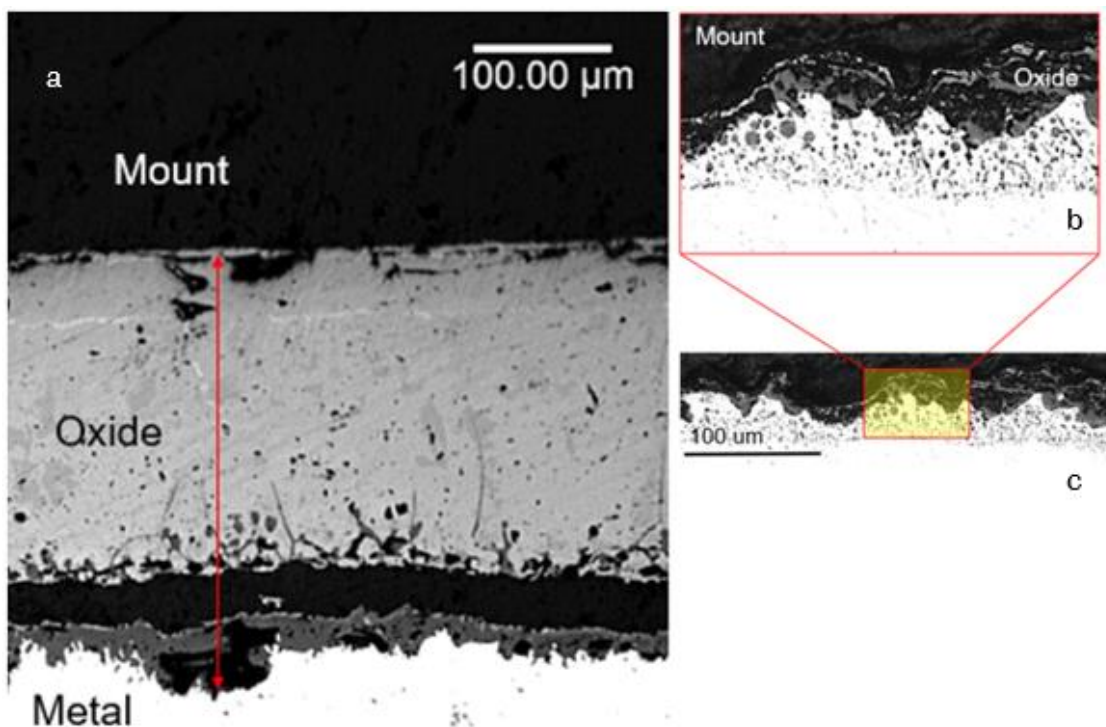
Test n°	Surface condition	Material	Scale before descaling (µm)	Scale after descaling (µm)
1	MILLED	Fe-3%Si	300 µm ±50 µm	15 µm ±10 µm
2	CONTAINING HOLES	Fe-3%Si	300 µm ±50 µm	16 µm ±10 µm

Table 4.3, a great reduction in oxide thickness was obtained through the water spray descaling process. In general, oxide layers thicker than 300 µm were reduced down to about 15 µm. Figure 4.15 shows two slabs of silicon steel after descaling and cooling. The argon environment present in the cooling box prevented the growth of secondary oxide scales. The borders of the top surface (highlighted in red) can be used as a reference to measure the oxide scale before the descaling. Differences in colour are visible, in particular, thicker oxide layers present a darker colour and it can be noticed at the edges of the slabs as highlighted in red in Figure 4.15.



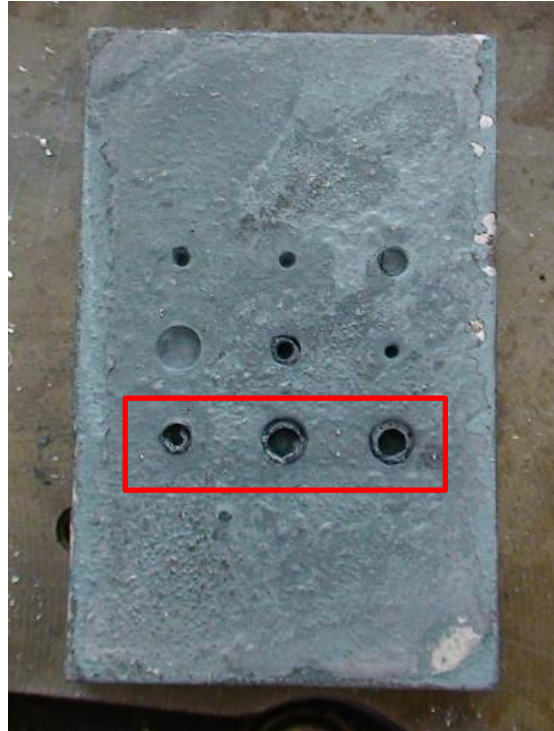
**Figure 4.15: 3% silicon steel slabs after the descaling and cooling, the highlighted regions shows a narrow band with some oxide scales still attached to the surface**

The Figure 4.16 shows the slab surface condition before and after descaling. Figure 4.16a presents the non-descaled band, the oxide thickness is about 260  $\mu\text{m}$  (as highlighted with a red arrow in Figure 4.16a), and a thin air gap of about 40  $\mu\text{m}$  is present. In fact, the thick light grey oxide layer appears detached from the slab in this section. The micrograph observable in Figure 4.16b shows an oxide layer with a thickness ranging from 5 to 30  $\mu\text{m}$ . The descaled final surface quality is not very smooth and the oxide shape profile is similar to the metal's profile conformation.



**Figure 4.16: Oxide condition before (a) and after the descaling (b, c) for a Fe-3%Si Steel (slab 1).**

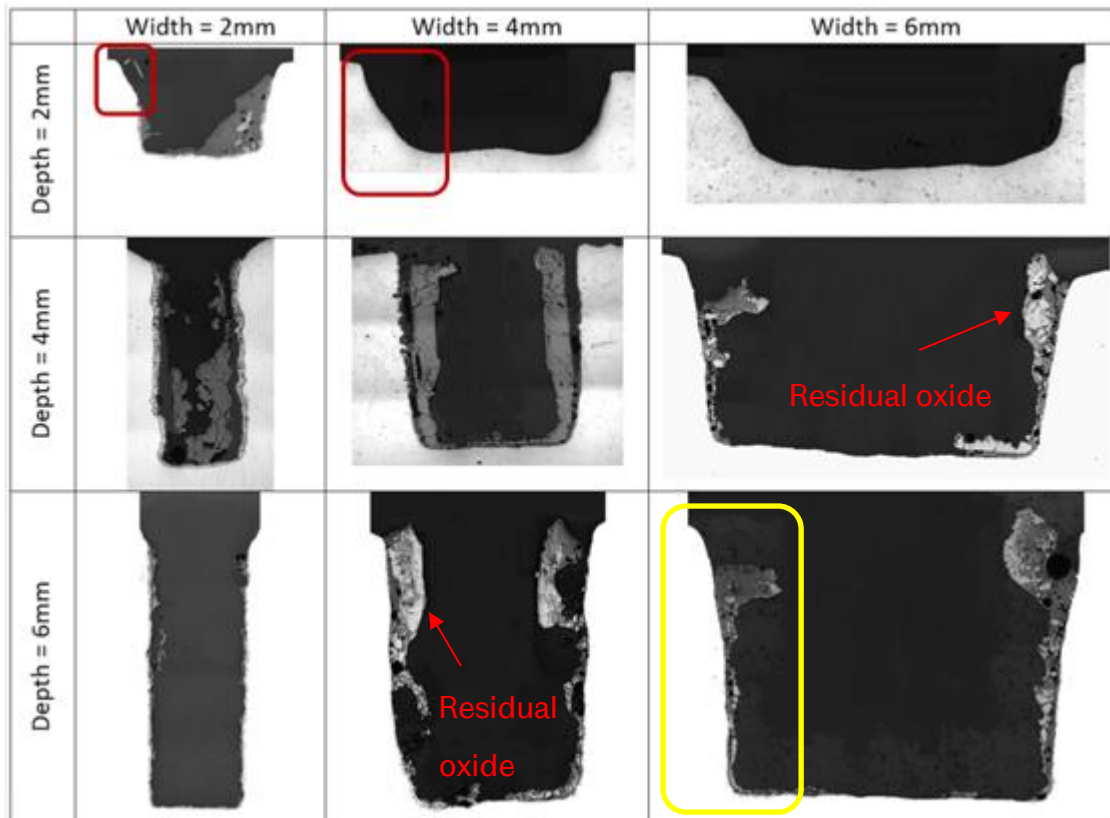
Figure 4.17 presents a top view of the slab containing holes after the descaling. As shown in the figure, the oxide was not completely removed from the cylindrical holes.



**Figure 4.17: Slabs containing cylindrical holes after the descaling for 2%Si steel and 3 %Si steel.**

As highlighted in Figure 4.17, a thick layer of oxide remained inside the holes despite the high-pressure water spray used. Figure 4.18 provides a better representation of the oxide scale residuals after descaling, the figure presents the micrographs of different cross sections of the descaled slabs. The oxide is sometimes indicated with a red arrow as a reference. In addition, it can be observed that thicker oxide layers ranging from 0.1 to 0.8 mm were found in the vertical sides of the holes, on the contrary, bottom surfaces were generally well descaled. An interesting finding was the great consumption of the lateral sides of the shallower holes as highlighted in red the Figure 4.18. The same effect was also present in deeper cavities, however, the effect was less pronounced as highlighted in yellow in Figure 4.18.

In general, shallower holes were better descaled compared to those more profound, and this is noticeable comparing the amount of residual oxide present in cavities with a depth of 6mm compared with the shallower cavities where the depth was 2mm.



**Figure 4.18: effect of the descaling inside cylindrical holes for a Fe-3%Si steel**

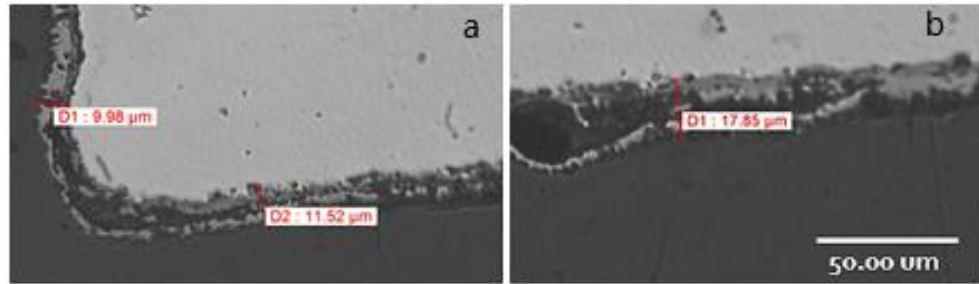
## **4.8 Isothermal hot ring compression experiment results**

### **4.8.1 Heat treatment of the rings**

Before the test, few samples were subjected to a particular heat treatment which is also explained in detail in chapter 3.3. This was done to double check if the oxide thickness that grows on the surface of the rings as a result of the heat treatment was in the range of the scale thickness encountered in the slabs of the hot rolling process after the descaling procedure.

The Figure 4.19 shows the oxide scale formed on the ring surface during the heating, the holding time of 5 min at 1050°C and the cooling of the sample. The image present parts of the ring were the thinner (Figure 4.19a) and the thicker (Figure 4.19b) oxide scales measured were present.

Samples were prepared using the same procedure explained in chapter 3.1 for the defects present in slabs.

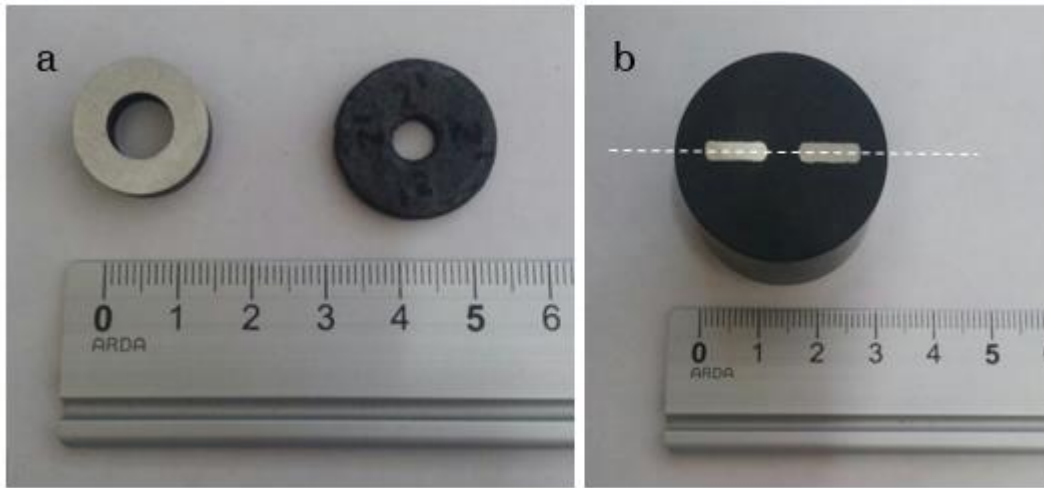


**Figure 4.19: Oxide scale present on the surface of the ring after the heat treatment in different points of the ring.**

According to the figure, oxide scales ranging between 9 to 20  $\mu\text{m}$  were measured on the rings surfaces before the compression. Considering all the instabilities involved during the oxide growth, the precision obtained is good. These values are in accordance with the measurements carried out in slabs subjected to descaling (chapter 4.7). The same heat treatment was then applied to all the rings just before the compression.

#### **4.8.2 Ring compression test**

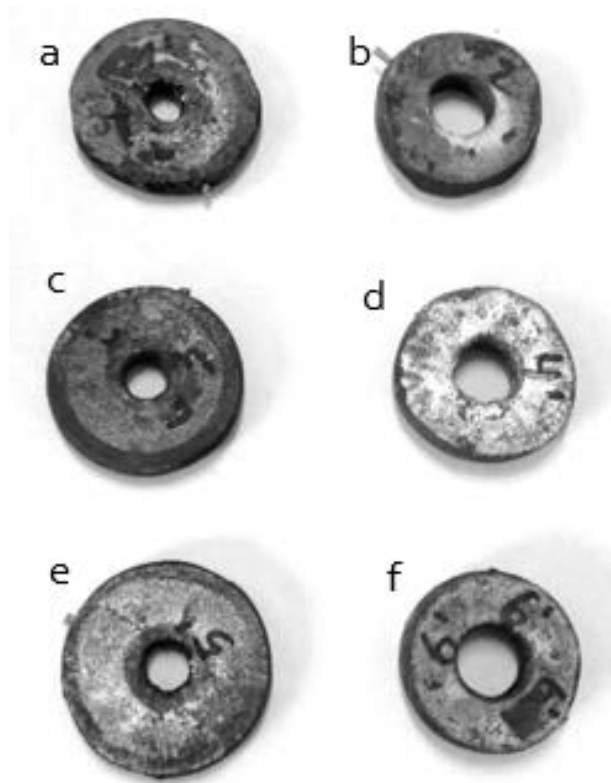
The compression of the ring was successfully done, sometimes the ring remained stuck on the surface of the tool after the compression, in these cases, the sample was easily removed from the oven with some pliers. The Figure 4.20 shows a top view and a transversal section of a typical ring after the compression compared with the ring before the compression. All the rings showed an axial symmetry of the deformation. In addition, the horizontal symmetry of the rings after the deformation was observed for the samples (symmetry plane is indicated by a white dashed line in Figure 4.20b).



**Figure 4.20: Ring before and after the compression, top view (a) and transversal section (b).**

It is worth noting that a radial spreading of the material internally and externally after the deformation is present, this, results in greater outer diameters and smaller inner diameters after the deformation. The internal spreading of material from the ring's inner surfaces during the compression is common for high values of friction.

Figure 4.21 shows six rings selected from each experimental conditions of the matrix of the experiments presented in chapter 3.3:

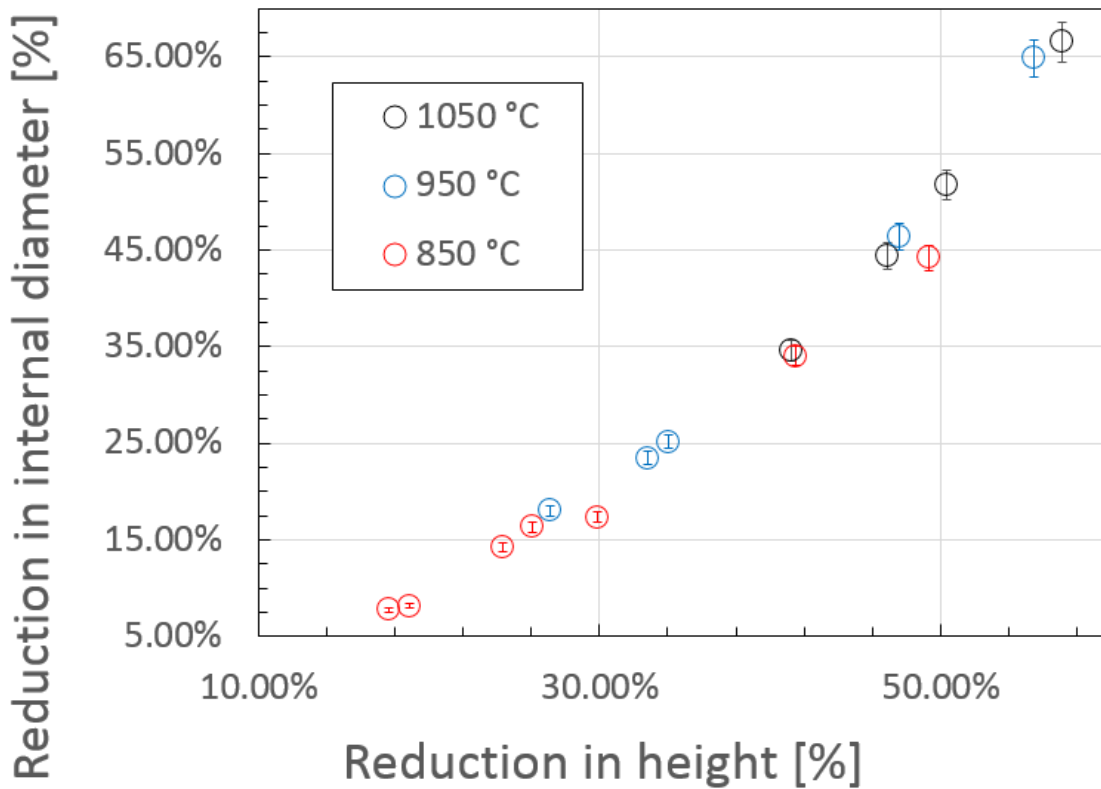


**Figure 4.21: Top view of the ring after the compression for each test conditions applied: rings a,b,c,d,e and f are the rings related to the tests 1, 2, 3, 4, 5 and 6 respectively (test condition are presented in chapter 3.3).**

It is apparent that a larger external diameter and a lower internal diameter of the rings a,c and e are formed during the deformation compared to the rings b,d and f due to the different reduction ratio applied. Additionally, rings internal diameter seem to be larger for lower test temperature (rings e,f compared to rings a,b), this is an index of different friction coefficient present for different test temperatures.

Rings internal diameters and thicknesses were measured at 6 different points, the average of the measurements of thickness and internal diameters were recorded. Measurements are reported in Figure 4.22.





**Figure 4.22: Internal diameter and height reduction ratio measurement of rings for different experimental temperatures**

These measurements were used to identify the friction coefficient by means of the calibration curves created. For the friction evaluation, the experimental points were compared with the calibration curves obtained with the modelling of the ring test process. The ring test model adopted and the friction evaluation is presented in Chapter 5.8.

## 4.9 Summary

The slabs containing cavities of different aspect ratios were successfully rolled, and the main mechanisms of deformation were identified. The results of this experiments were used to calibrate and validate a model reproducing the same process and defect evolution.



The analysis of the distorted pins show the dependence of friction on the oxide scale thickness and highlights the importance of investigating and identifying the specific oxide scale present after descaling in industrial hot rolling processes.

The descaling experiment results identified the oxide thickness present on the surface of the slab during rolling, the same oxide thickness was successfully growth in ring samples subjected to compression. Isothermal ring tests were carried out at different temperatures, the analysis of the samples indicates that there is an effect of temperature on the friction values. The friction evaluation is carried out on Chapter 5.8.

## **5 FE MODELLING APPROACH**

To simulate complex industrial processes like hot rolling, assumptions must be carefully considered to simplify the problem. However, it is essential not to oversimplify the phenomena to avoid unrealistic behaviour of the model. In this context, assumptions are necessary to simplify the material behaviour of the roll and the slab, the contact between slab and roll, and the geometrical representation of the full model as well as the defects.

Before proceeding to the simulations of an industrial hot rolling process, a material model was defined and calibrated based on Gleeble compression test data carried out at different temperatures and strain rates provided by the industrial partner. Therefore, a model reproducing the behaviour of a lab rolling mill process was developed and validated by comparing its predictions with the measurement obtained from the lab rolling process simulated. Once the model was validated, the material, the geometrical and contact assumptions adopted were applied to a full-scale hot rolling model as reported in chapter 6. The next subchapters present the developed material model, the assumption made for the contact and boundary conditions, the multilevel approach adopted and the calibration procedures carried out.

### **5.1 Developing a constitutive equation for Fe-3% Si steel**

The project focused on a silicon steel alloy with a silicon content of 3 wt% and a carbon content of 0.042 wt%. The chemical composition and temperature of the material affect the deformability. At a high silicon content (more than 3.5 wt%) the alloy shows high values of the flow stress that leads to poor deformability and rollability [98]. During the rolling, initial temperatures above the crystallisation temperature are used to reduce the high roll forces. However, when slabs are rolled, temperature losses due to radiation to the environment, water spray and conduction with the rolls are present. Therefore, a temperature dependent material model is required to accurately predict the deformation behaviour of the material during the rolling. In addition, considering the high

deformation velocities at which the material is rolled, the strain rate dependence of the material should also be taken into account.

A user-defined UMAT subroutine was developed to formulate the thermo-mechanical constitutive behaviour of the material. Two different behaviours were taken into account for the mill and the slab. The mill was considered as a rigid body and only the thermal degree of freedom was taken into account. The slab was modelled according to the Sellars and Tegart (S&T) [99] temperature-displacement coupled material model, the model was chosen because of the good quality of the fitting with the compression curves compared with other material model tested (as Johnson-Cook). The Equation 5.1 shows the flow stress predictive equation used. The flow stress is determined for a given ultimate compressive stress ( $\sigma_s$ ) and different strains:

**Equation 5.1**

$$\sigma = (\sigma_s(T, \dot{\epsilon}) - Q) + Q \cdot \sqrt{1 - e^{-b \cdot \epsilon}}$$

where  $Q$  and  $b$  are the hardening calibration terms.

The ultimate compressive stress is a function of temperature and strain rate and is calculated using the calibrated S&T model (Equation 5.2)

**Equation 5.2**

$$\sigma_s = \sin^{-1} \sqrt{\frac{\dot{\epsilon} \cdot e^{\left(\frac{\Delta H}{RT}\right)} \cdot 1}{A}} \cdot \frac{1}{\alpha}$$

where the terms  $A$ ,  $\alpha$ , and  $n$  are material constants,  $R$  is the universal gas constant,  $T$  is the absolute temperature,  $\dot{\epsilon}$  is the strain rate and  $\Delta H$  is the apparent activation energy for plastic deformation at high temperature. Additional description of the terms is presented in the Nomenclature section.

## **5.2 Loads, contact interactions and boundary conditions of the model**

The rolling operation was modelled in three successive steps (initial, first and second). The initial step was used to define the initial conditions of the process.

Initial temperatures of the mill and slab were defined at this stage. In step one, the initial translation velocity for the slab was fixed and a boundary condition simulating a radiation to the environment was applied to take into account the heat losses before the rolling. In step two, a constant rotational velocity for the mill was defined. Radial roll velocity and initial slab velocity were chosen to be equal allowing the slab to enter the rolling gap without bumping, contact is defined in this step.

The interaction between roll and slab is a crucial issue for the defect deformation. Oxide scale present in the slab was not modelled in this research study, but it was assumed to affect the heat transfer and friction coefficient at the point of contact between the slab and the rolling mill.

The conduction between slab and roll was modelled according to the Equation 5.3:

**Equation 5.3**

$$q_c = k \cdot (\theta_a - \theta_b)$$

where  $q$  is the heat flux per unit area that crosses the surface from point  $a$  to point  $b$  with the temperature of  $\theta$  and  $k$  is the conductance in the contact zone, and it is fixed to  $20 \frac{kW}{m^2 \cdot K}$  (this valued was estimated by the industrial partner of the project and it is commonly used for their numerical modelling of heat transfer during hot rolling for electrical steel);

The initial heat loss due to radiation to the environment was also considered through the Equation 5.4:

**Equation 5.4**

$$q_r = \varepsilon_i \cdot \sigma [(\theta_{AVG})^4 - (\theta_{AMB} - \theta^z)^4]$$

Where  $\varepsilon_i$  is the emissivity of the surface, and it is fixed to 0.8, the value was provided by the industrial partner;  $\sigma$  is the Stefan-Boltzmann constant;  $\theta_{AVG}$ ,  $\theta_{AMB}$ ,  $\theta^z$  are the average temperature of the surface, the ambient and the absolute zero temperature, respectively.

During the contact, heat is generated due to plastic deformation and friction between slab and mill. The first contribution was calculated by means of the user Umat subroutine where the heat flux per unit of volume ( $r^{pl}$ ) was evaluated as [100]:

**Equation 5.5**

$$-r^{pl} = \eta \cdot \sigma : \dot{\epsilon}^{pl}$$

where  $\eta$  is the fraction of plastic work converted to heat, and it is fixed to 0.9 [28];  $\sigma$  and  $\dot{\epsilon}^{pl}$  are the stress and strain rate vectors calculated by means of the UMAT subroutine developed.

The second contribution was calculated from the relative velocity between roll and slab [100]:

**Equation 5.6**

$$-q_s = f \cdot \eta \cdot Pfr; \quad q_s = (1 - f) \cdot \eta \cdot Pfr$$

Where  $f$  is the fraction of converted heat distributed on the surface of the slab and it is assumed to be equally distributed between slab and roll, so it is fixed to 0.5;  $\eta$  is the fraction of frictional work converted to heat, and it is fixed to 1;  $Pfr$  is the product of the frictional stress and the slip rate  $Pfr = \tau \cdot \dot{\gamma}$  [100].

The parameters related to the contact between the strip and the roll can greatly affect the defect behaviour during rolling. The interaction between the roll and strip was modelled with a Coulomb friction model (Equation 5.7) [100]:

**Equation 5.7**

$$\tau = \min(\mu \cdot p; \tau_{lim})$$

where  $\tau$  is the shear stress;  $\mu$  is the friction coefficient;  $p$  is the contact pressure. The friction coefficient has been calibrated experimentally and the experimental procedure is explained in the following chapters of this thesis.

According to the model (Equation 5.7), no relative motion between the surfaces in contact occurs when the equivalent shear stress at the contact is less than the critical shear stress values calculated with the model ( $\tau_c$ ). However, due to the high compressive stresses at the contact point, the Coulomb model may provide unrealistic critical shear stress values which exceed the yield stress of the material. For this reason, a shear limit ( $\tau_{lim}$ ) was defined. This arrangement ensures that when the equivalent shear stress value achieves the  $\tau_{lim}$ , slipping between the roll and the slab is permitted.

Hard contact algorithms [100] were used in the contact zone between slab and mill to reduce penetrations, with this model no pressure is present when there is no contact, and any possible pressure can be achieved to prevent penetrations between the master and the slave surface. Soft self-contact algorithms [100] were used to define the contact between the defect surfaces to simplify the convergence, with this model, relationships between clearance and pressure are defined, contact is calibrated to reduce any penetrations between the defect surfaces.

### **5.3 Geometry, mesh and Multilevel approach**

The full model reproduced the laboratory rolling process explained in chapter 3.1, where two parts are in contact with each other, the rolling mills and the slab containing the defect. The lab rolls diameter was 223mm and initial slab thickness was 25mm while the dimension of the defects present on the surface of the slabs was in the order of a few millimetres. Considering the large difference in the order of dimensions between the rolling mill and the defects, a multilevel modelling approach was necessary to produce accurate solutions without the need to the full model for each defect considered. Therefore, two models at different scale were developed.

The first model, called macroscale model, represents the rolling setup containing two rolls and one slab. A vertical symmetry plane (ND-RD) was used and only half of the rolls and the slab were considered. No defects were present in this case.

The second model, meso-model, is a sub-volume of the macroscale model and includes a shorter portion of the slab containing the defect and half of one roll. Defects were located to the top surface of the slab of the mesoscale model.

The particularity of this technique is the fact that the boundary conditions of the meso-model are defined based on the node field results (in terms of displacement and temperature) of the macroscale model. Therefore, defects of different geometries can be analysed without the need of running a full model of the process containing the defect. In addition, better mesh refinements in the defect zone and considerable savings in terms of numerical calculation times and memory space are obtained.

### **5.3.1 Macroscale model**

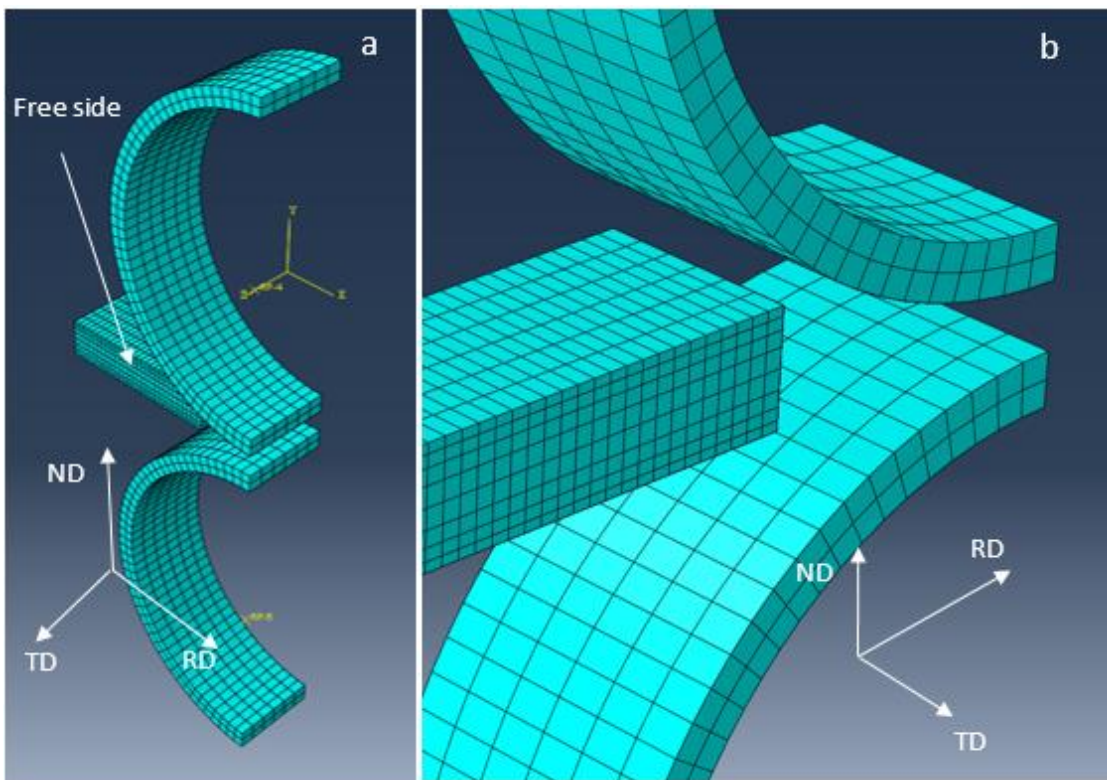
The macro-model was made by two parts that were in contact with each other, the rolling mill and the slab (squared toroidal roll and a rectangular cuboidal slab) as shown in Figure 5.1. The main geometry features of the parts considered are as follows: Roll diameter ( $d$ ): 223 mm; Slab thickness in ( $th-i$ ): 25 mm; Slab thickness out ( $th-o$ ): 15 mm;

The rolling mills were modelled as a half rings meshed with 8-node thermal stress coupled hexahedral first order elements (element code C3D8RT). The element size was 10mm in the transversal direction, 6.5mm in the tangential direction and 5.7mm in the radial direction of the rings. The rolls are rigidly constrained to rotate around its axes. A ratio of 2.5 between the surface area size of elements in the roll and the size of the elements in the strip is guaranteed in the contact zone as shown. A mesh convergence study was carried out to determine the proper elements dimension.

The radial thickness of the toroid is 15 mm, sensitivity tests were carried out to demonstrate that this thickness was enough to guarantee the proper internal heating during the contact considering the rolling velocity and the Heat Transfer coefficient provided. Considering a toroid instead of a full cylinder implies big savings in terms of calculation times as less volume of the roll is modelled. The initial width of the slab was 87.5 mm and the mill was designed to have a width

of 120 mm to ensure enough space for the slab to spread laterally during the rolling procedure.

The slab part was meshed with 8-node thermal stress coupled hexahedral elements (C3D8RT). A light transition in the vertical height of the elements is defined to better acquire the plastic deformation of the slabs in the contact zone. Reduced integration elements with hourglass stiffness were used to avoid the shear locking effect. As the slabs are relatively thin with respect to the defect depths, horizontal symmetry cannot be assumed for the lab mill model because of the presence of the defect on one side.



**Figure 5.1: a) Macroscale model, b) element dimension in the contact.**

### **5.3.2 Mesoscale model**

The multilevel approach is useful to obtain an accurate solution for a local region of a big model avoiding excessive numbers of elements in the model. The application of this technique is acceptable only if the solutions at the boundary of the mesoscale model are not altered substantially by the application of the



different local modelling. In this case, the presence of the defect must have a negligible effect on the stress and temperature field of the macroscale model. There are not any built-in check criteria in the Abaqus software for this. Therefore, it is a user responsibility to check the response and the accuracy of the mesoscale model application. For this reason, the accuracy will be checked through comparison of the stress and temperature fields near to the boundary of the mesoscale model.

A set of different mesoscale models varying in slab length containing the defects were run to find the most suitable sub-volume. The effect of the presence of the defect on the node temperature and displacement fields at the boundary were monitored. The aim was to identify a dimension of the local zone containing the defect which is large enough to guarantee that the presence of the defect did not affect the boundary node field applied.

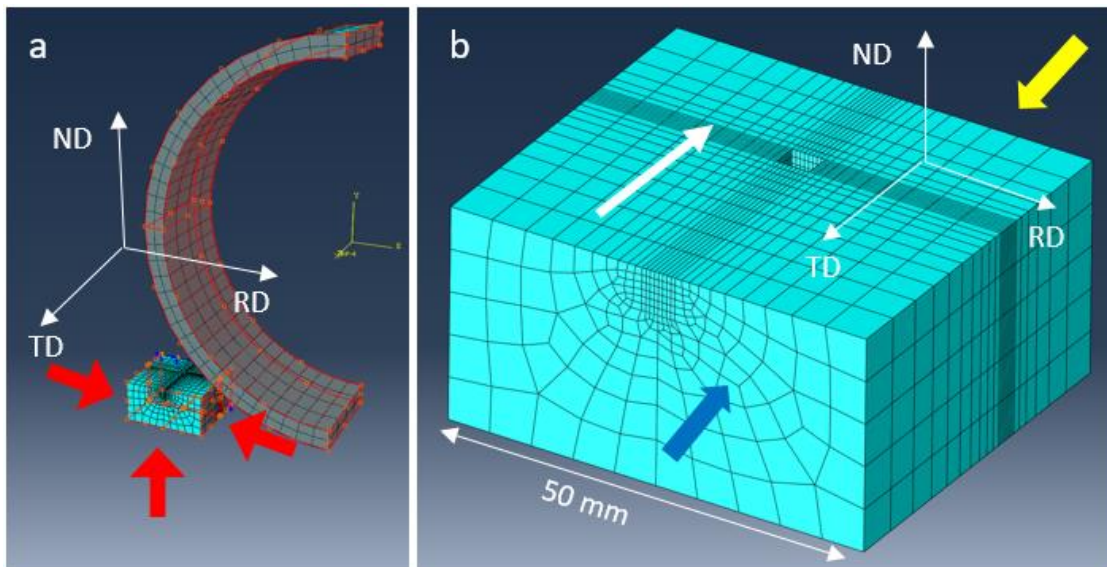
Accuracy was checked through the comparison between the temperature and stress fields calculated near the boundary of the mesoscale model and the same variables calculated on the section surfaces of the macroscale model.

The results of the thermal and displacement field of the nodes of the macroscale model were applied to the boundary faces of the mesoscale model slab. The roll was assumed rigid and only a thermal degree of freedom was considered to reproduce the slab cooling due to conductance between the parts. Since the defects are present on the top surface only, there is no need to simulate the contact of the bottom slab with the roll as the bottom surface of the slab is forced to deform following the nodal solution of the global model. The final mesoscale model is a local model where a portion of a slab containing the defect (having a length of 50mm) is forced to deform accordingly to the boundary node field results of the macroscale model applied and due to the contact with the top rigid mill.

Figure 5.2 presents an example of the final mesoscale models and the detail of the mesh morphology used to represent the defect. Figure 5.2a presents the three boundary surfaces of the mesoscale model where the solutions of the macroscale model were applied (highlighted with red arrows and red surfaces).

As can be noticed by the red surface, the results of the macroscale model were also applied to the roll. The boundary conditions of the mesoscale model (including node temperature and node position) are applied to the selected surfaces, and updated during the calculations in accordance with the results of the macro scale model obtained at the boundaries. A vertical symmetry is also applied to the lateral back surface of the slab (the side is indicated in yellow in Figure 5.2b).

The mesh is extruded in the transversal direction as indicated by a white arrow in Figure 5.2b. Transition meshes are developed in the longitudinal plane to appreciate the small dimension of the defects applied. A mesh convergence study indicated that a minimum number of 6 elements in the vertical direction of the defects was enough to guarantee the proper deformation of the defect sides for all the defects considered (the study is presented in chapter 5.7.1). The element aspect ratio in the zone near to the defect is about 1:1. In Figure 5.2b, the free lateral side and the symmetric plane of the sub-model slab are indicated with blue and yellow arrows respectively.



**Figure 5.2: Sub-model and boundary conditions applied.**

During the deformation, the contact roll surface, the slab contact surface, and the internal sides of the defect interact with each other.

## 5.4 Material model and strain patterns calibration of the laboratory model

To calibrate the Sellars and Tegart material model, the results of a Gleeble compression test carried out at different temperatures and strain rates provided by the industrial partner were used.

The results of defect behaviour experiment (presented in chapter 4) were used to calibrate the contact conditions of the macro-model and validate the meso-model.

### 5.4.1 Material model

The four material constants  $A$ ,  $\alpha$ ,  $n$  and  $\Delta H$  were determined using a numerical technique proposed by Uvira [44]. The model was fitted with the ultimate compressive stresses of the experimental curves obtained with a Gleeble test done at different strain rates and temperatures for a Fe 3%Si alloy. Table 5.1 shows the ultimate compressive stress values measured at different temperature and strain rates.

**Table 5.1: Ultimate tensile stress measured at different strain rates and temperatures.**

		Temperature				
		800 °C	900 °C	1000 °C	1100 °C	1200 °C
Strain rate	25 <i>sec</i> <sup>-1</sup>	220 MPa	170 MPa	125 MPa	100 MPa	75 MPa
	10 <i>sec</i> <sup>-1</sup>	190 MPa	145 MPa	120 MPa	85 MPa	55 MPa
	1 <i>sec</i> <sup>-1</sup>	140 MPa	115 MPa	80 MPa	60 MPa	45 MPa

The following practice in accordance with Uvira [44] was used to determine the most appropriate values for the parameters  $\alpha$  and  $n$ .

Starting from a different representation of Equation 5.2:

**Equation 5.8**

$$\dot{\epsilon} \cdot e^{\left(\frac{\Delta H}{RT}\right)} = A \cdot [\sinh(\alpha\sigma_s)]^n = Z$$

Considering  $\Delta H$  and  $A$  constant, and considering two different stresses, strain rates, and temperature conditions, we can assume that:

**Equation 5.9**

$$\ln\dot{\epsilon}_1 - n \cdot \ln[\sinh(\alpha\sigma_{s1})] + \frac{\Delta H}{RT_1} = \ln\dot{\epsilon}_2 - n \cdot \ln[\sinh(\alpha\sigma_{s2})] + \frac{\Delta H}{RT_2}$$

If the temperature is kept constant the Equation 5.9 can be written as:

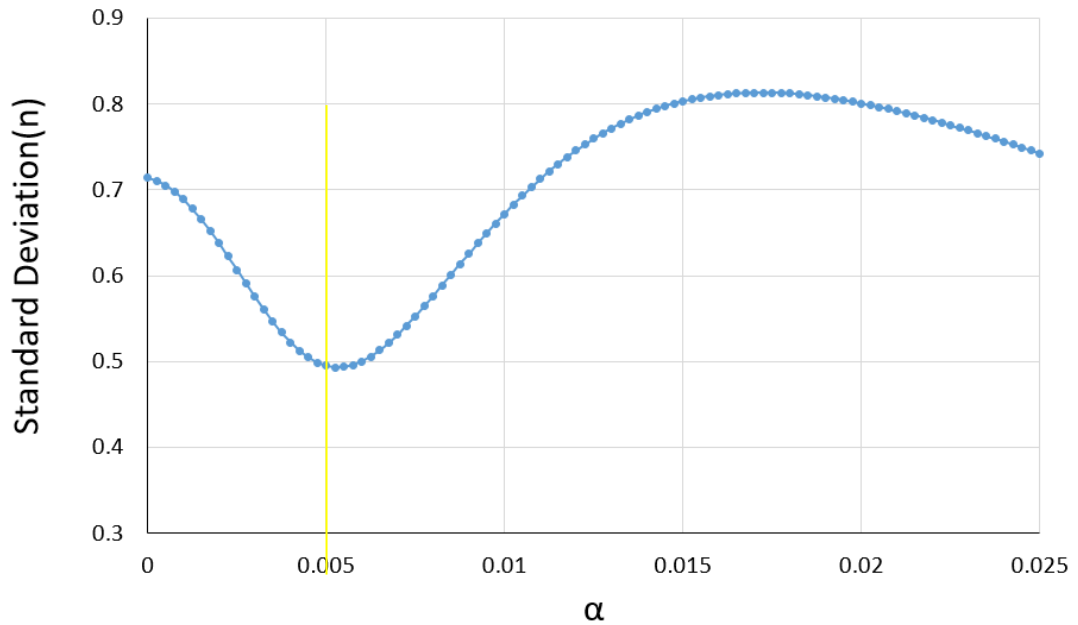
**Equation 5.10**

$$\ln\dot{\epsilon}_1 - n \cdot \ln[\sinh(\alpha\sigma_{s1})] = \ln\dot{\epsilon}_2 - n \cdot \ln[\sinh(\alpha\sigma_{s2})]$$

From the Equation 5.10  $n$  can be expressed in terms of  $\alpha$ , and  $\alpha$  is evaluated to be the one that minimise the standard deviation of the exponent  $n$  for the full range of stress and temperatures considered [Figure 5.3]:

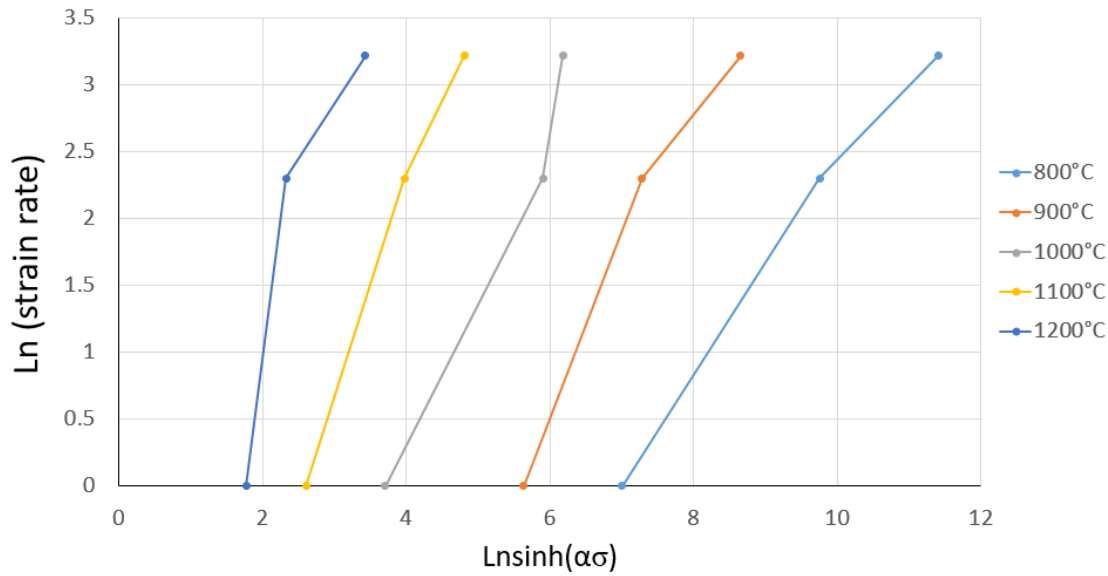
**Equation 5.11**

$$n = \frac{\ln\dot{\epsilon}_1 - \ln\dot{\epsilon}_2}{\ln[\sinh(\alpha\sigma_{s1})] - \ln[\sinh(\alpha\sigma_{s2})]}$$



**Figure 5.3: Evolution of the standard deviation of the apparent stress exponent,  $n$ , with the variation of  $\alpha$ .**

The parameter  $\alpha$  is found to be 0.0055, the value was identified in correspondence of the minimum of the standard deviation curve plotted in Figure 5.3 (as highlighted with the yellow line). The parameter  $n$  is found to be 1.26 and it is obtained from the average of the slopes calculated from the same equation using the  $\alpha$  value identified (Equation 5.11). The plot of the hyperbolic sine law of the experimental data for different temperature is presented in Figure 5.4.

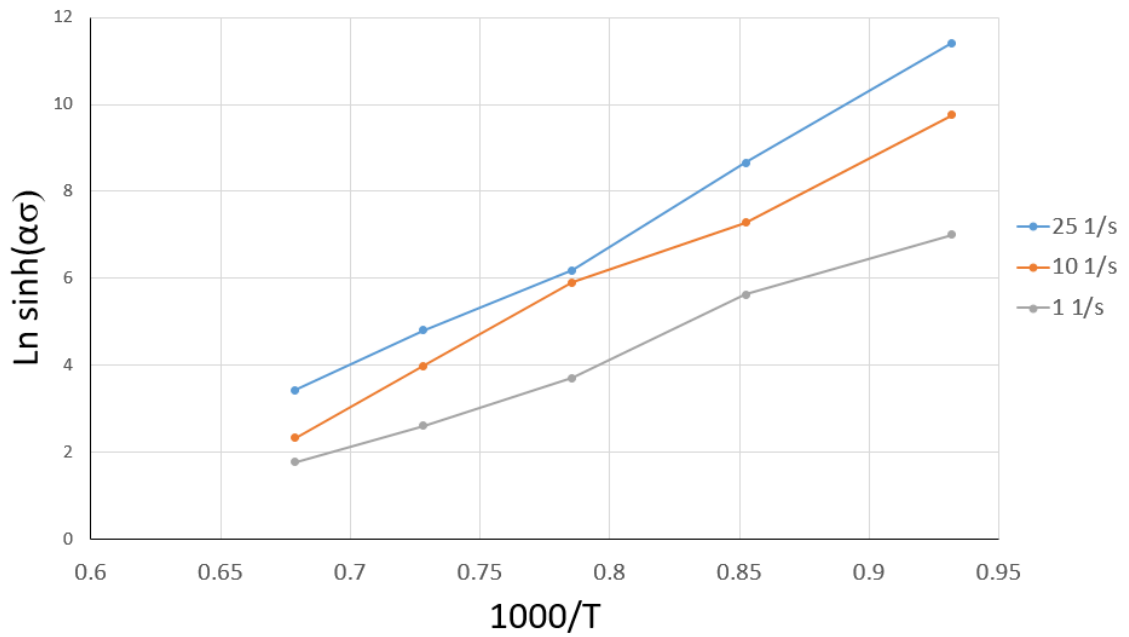


**Figure 5.4: Experimental data plotted with hyperbolic sine stress law for different temperatures and strain rates.**

Considering the average value for  $n$ , its temperature dependence is avoided. Once value of  $n$  is determined, the plot between  $\ln(\sinh(\alpha\sigma))$  and  $(1/T)$  at different strain rates can be used to determine the apparent activation energy through the slope of these curves (Figure 5.5). Similarly, an average value is considered to avoid the dependence of the strain rate [44].

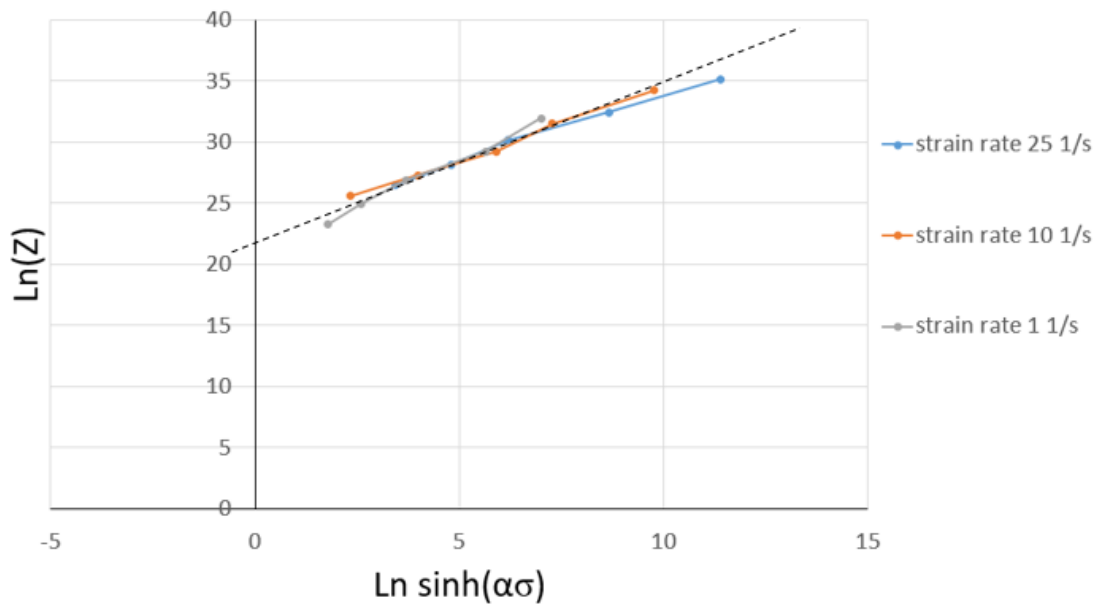
**Equation 5.12**

$$\Delta H = n \cdot R \cdot (\text{slope}_{\text{average}}) = 285 \frac{\text{KJ}}{\text{mol}}$$



**Figure 5.5: Temperature dependence of saturation stress for different strain rates.**

Finally, the parameter  $A$  is determined from a plot of  $\ln Z$  against  $\ln \sinh(\alpha\sigma)$  presented in Figure 5.6. The value of  $Z$  when  $\sinh(\alpha\sigma) = 1$  is taken as  $\ln A$  and it is found to be 22.7. The value was identified as the average of the intercept of each plot.



**Figure 5.6: Stress dependence of LnZ for different strain rates.**

Using the above-mentioned procedure,  $A$  is found to be  $A = 4.7 \cdot 10^9$ .

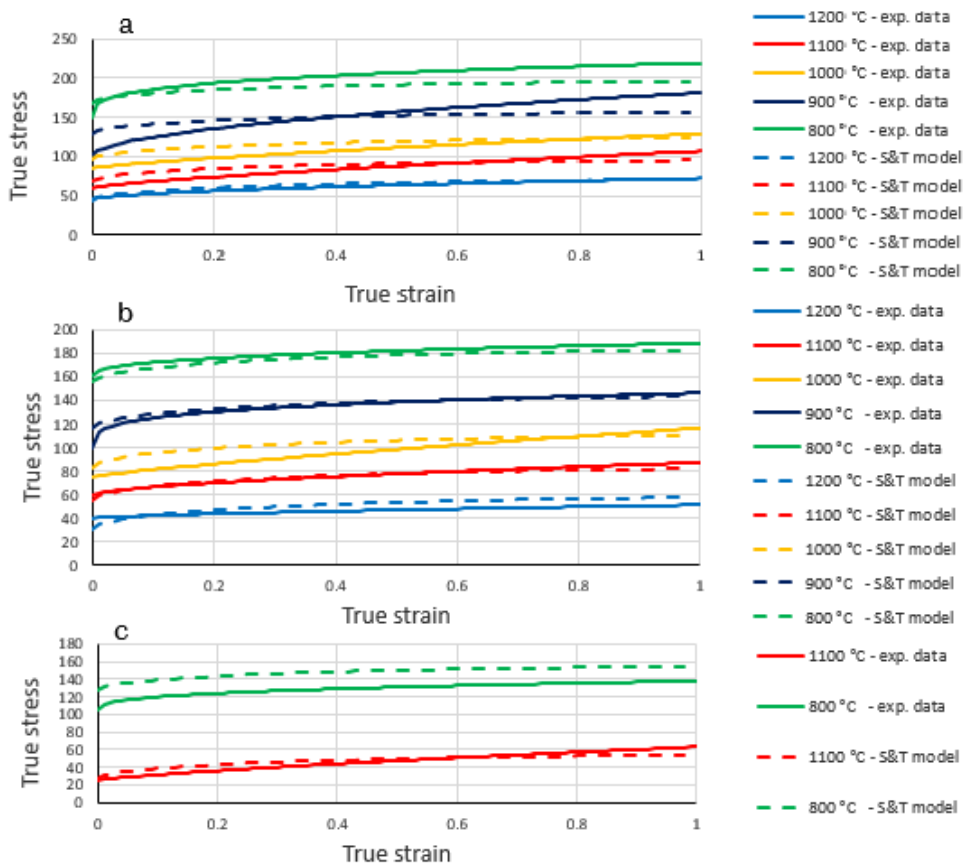
A least square technique was used to calibrate the Equation 5.1 with the Gleeble compression test data.  $Q$  and  $b$  were found to be 30 and 1.8 respectively.

A summary of the calibrated parameters is presented in Table 5.2:

**Table 5.2: Material model calibrated parameters**

$Q(MPa)$	$b$	$A (s^{-1})$	$\alpha(MPa^{-1})$	$n$	$\Delta H(\frac{KJ}{mol})$
30	1.8	$4.7 \cdot 10^9$	0.055	1.26	285

Figure 5.7 shows the comparison between the experimental data and the calibrated model for different temperatures and strain rates.



**Figure 5.7: Sellars & Tegart model comparison with the experimental data for different strain rates and temperatures (A, B, C stand for hardening curves obtained at strain rates of 25 s<sup>-1</sup>, 10 s<sup>-1</sup> and 1 s<sup>-1</sup> respectively).**



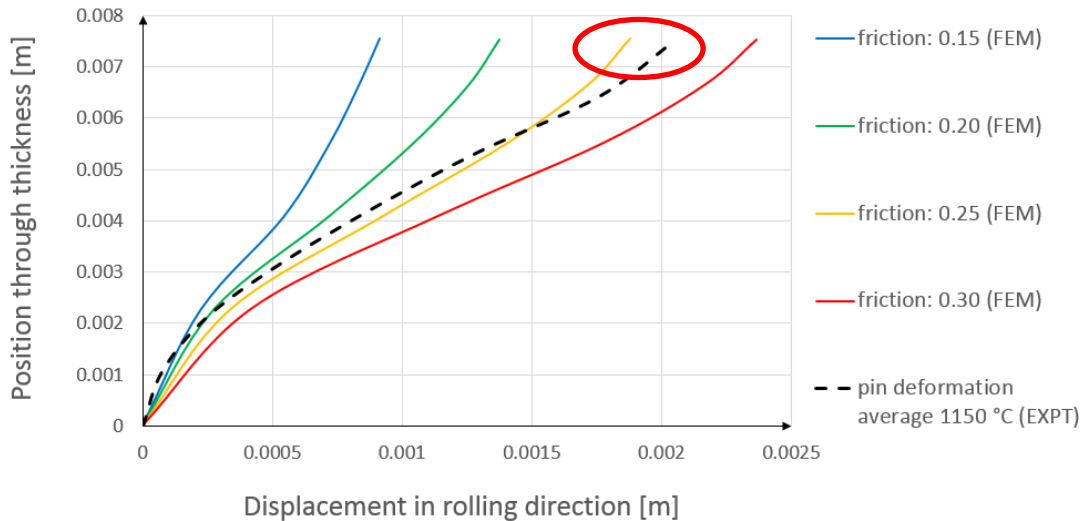
As noticeable from Figure 5.7, the quality of the experimental and numerical data match depends on the temperature and strain rate ranges. The fitting quality is more accurate for higher values of strain rate and temperatures. In fact, the curves related to temperatures above 900°C (represented with yellow, red and light blue colours) shows better quality than for temperature below 900°C. Similar considerations can be extended to the curves obtained at different strain rates, in fact, it can be observed that the quality of the fitting is better for strain rates of 10 s<sup>-1</sup> and 25s<sup>-1</sup>.

Overall, the outcome of the prediction of the material model is good considering that the ranges of strain rates and temperatures involved in the hot rolling process simulated are above 1s<sup>-1</sup> and above 900°C, respectively. The temperature of the surface in hot rolling processes can reach 900°C, in those cases, it is more appropriate to improve the fitting for lower temperatures, this can be done increasing the number of experimental measurement points for lower temperatures of the process considered.

#### **5.4.2 Macroscale model calibration of the strain pattern**

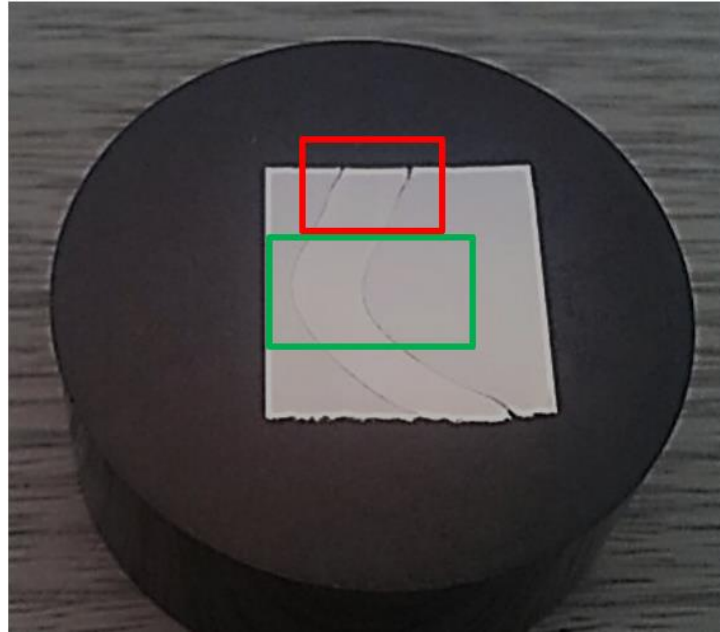
The validated material model was used to describe the thermomechanical behaviour of the slabs subjected to hot rolling. Before proceeding to the mesoscale modelling, the macroscale model was calibrated to ensure the accuracy of the predicted strain patterns observed during the rolling experiment. Calibration was carried out comparing the mesh longitudinal distortion pattern with the distorted pin inserted into the slab before the experiment. Similar procedures were carried out by Mukhopadhyay [74] and Boldetti [77]. Pins were measured at 8 different locations through the thickness of the slab. As the longitudinal strain pattern obtained is directly linked to the friction coefficient present in the contact between slab and roll, a series of models reproducing the process were run for different friction coefficients. Friction was adjusted until the longitudinal strain pattern of the model after rolling matched the average of the longitudinal pin distortion patterns. Figure 5.8

shows the average of the pin curvature and the longitudinal curvature of the mesh after rolling for different friction coefficients (only the top half slab is considered).



**Figure 5.8: Longitudinal displacement comparison between distorted experimental pins, and model mesh run at different friction coefficients.**

According to the comparison, the friction coefficient was calibrated to be 0.25. However, small differences were encountered at the surface between the pin distortion pattern and the model, as highlighted in red in Figure 5.8. The differences are due to the small gap between the pin and the housing at the end of the pin as highlighted in Figure 5.9. The gap shows that the pin may have deformed more than the normal, however, this effect was not encountered internally (as highlighted in green in Figure 5.9.), thus, the match is more accurate in the centre zone of the pin (Figure 5.8).



**Figure 5.9: Deformed pin after rolling, longitudinal RD-ND section, a small gap between pin and housing is highlighted in red.**

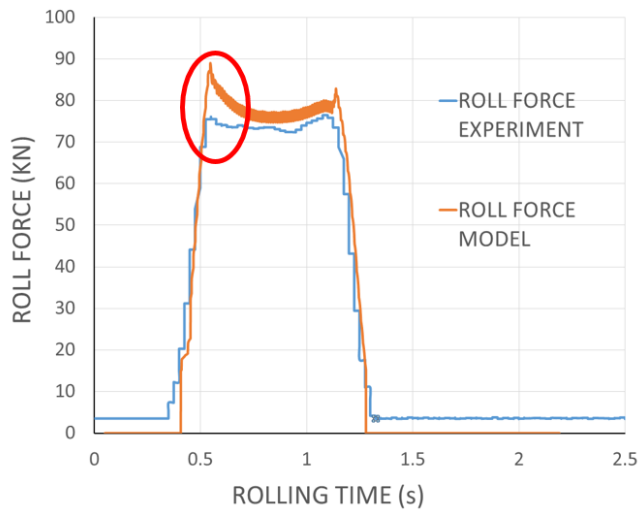
Once the friction coefficient was calibrated, the roll forces measured during the experiment were compared with the ones obtained from the model run at the specific friction coefficient calibrated ( $f=0.25$ ). This further comparison was used to ensure that the calibrated value of the friction coefficient and the heat transfer coefficient (HTC) provided by the industrial partner and used during the research carried out were reliable. In fact, the HTC is expected to play an important role in the roll force value measured during rolling.

According to the results, the friction coefficient is estimated to be 0.25. This value will be used hereafter for the lab mill simulations.

Figure 5.10 presents the roll force recorded during the experiment and the roll force measured from the model run with a friction coefficient of 0.25. Errors of about 5% are found between the experimental roll force measured and the model predictions. The model over-predicted the roll forces slightly.

The peak of the roll force predicted value observable at the rolling time of 0.5 sec (highlighted in red in Figure 5.10) is due to the initial impact between the slab and the roll as a consequence of the initial velocity imposed. Specifically, the strain rate sensitivity of the material model increases the strength of the

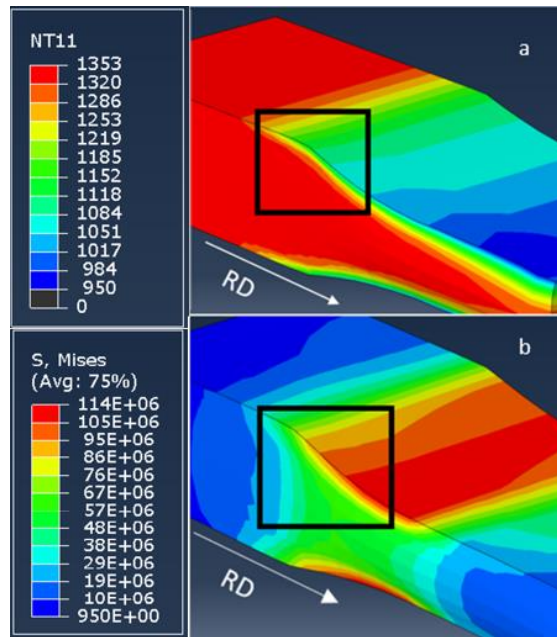
material during the first impact. However, this was only a transient condition and it is not expected to affect the defect evolution because involves the first contact only.



**Figure 5.10: Roll force comparison between experiments and simulations**

## 5.5 Macroscale model results

The results of the Mises stress and temperature field obtained from the calibrated macroscale model are presented in Figure 5.11. A gradient of temperature in the slab contact zone is shown in Figure 5.11a. This is a consequence of the initial difference in temperature between slab and roll which induced the heat transfer conduction between the roll and the slab during the contact. This gradient of temperature formed at the surfaces gradually changes the material properties through the slab thickness. A gradient of stress is also experienced in the slab, with higher values in the contact zone with the roll (Figure 5.11b).



**Figure 5.11: (a) Temperature (°K) and (b) Stress fields (Pa) of the slab in the contact zone.**

## 5.6 Mesoscale results

The multilevel approach requires a sub volume to be cut from the macroscale model. The boundaries of the mesoscale model obtained are then forced to deform accordingly to the node displacement field and temperature field results of the initial macroscale model.

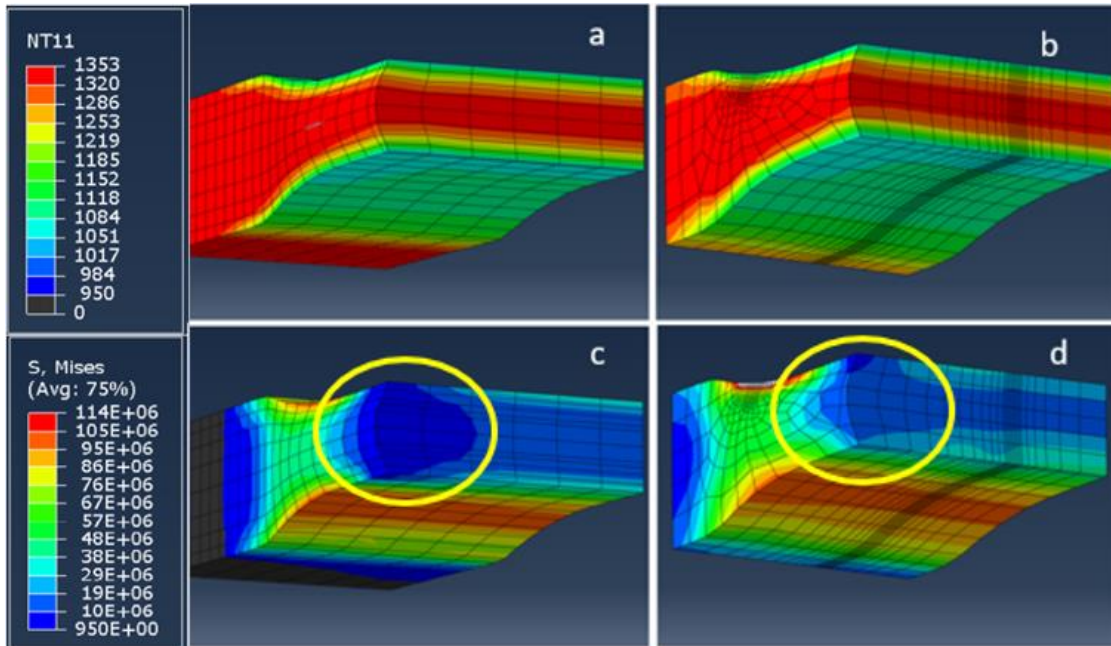
### 5.6.1 Mesoscale model quality check

The quality of the sub-modelling application must be checked by the user as there are not any built-in criteria present in the software to verify the reliability of the approach adopted.

To make sure the technique is adequately applied, a comparison of the stress and temperature fields between the mesoscale boundary surfaces and the macroscale model was carried out. The scope was to check if the presence of the defect on the surface of the meso-model slab had a negligible effect on the main variables measured at the boundary surfaces. A trial and error technique was used to identify the proper mesoscale dimension. It was found that a slab of a reduce length of 50mm in the rolling direction was large enough to guarantee

a proper quality of the multilevel modelling application for all the defects analysed.

Figure 5.12 shows the comparison of the temperature and the Mises stress measured at the bottom and front boundary surfaces of the mesoscale model (Figure 5.12b,d) with the temperature and Mises stress measured at the bottom and on the transversal section of the macroscale model (Figure 5.12a,c).



**Figure 5.12: Temperature ( $^{\circ}\text{K}$ ) field comparison between a) Macroscale model and b) Mesoscale model; Mises stress (Pa) comparison between c) Macroscale model and d) Mesoscale model, next to the boundary surfaces.**

Slight differences are present for the stress field as highlighted in yellow in Figure 5.12. Those inevitable deviations are due to the difference in meshes between macroscale and mesoscale models and relative mesh transition.

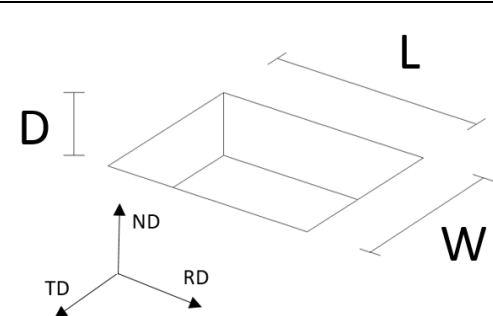
## 5.7 Defect behaviour during rolling

To analyse and validate the model prediction of the defect behaviour during rolling, five defects of different aspect ratios were selected from the list of all the cavities tested in the hot rolling experiment reported in chapter 3.1. Cavities were selected to represent middle values of L (10mm) and W (7mm) for

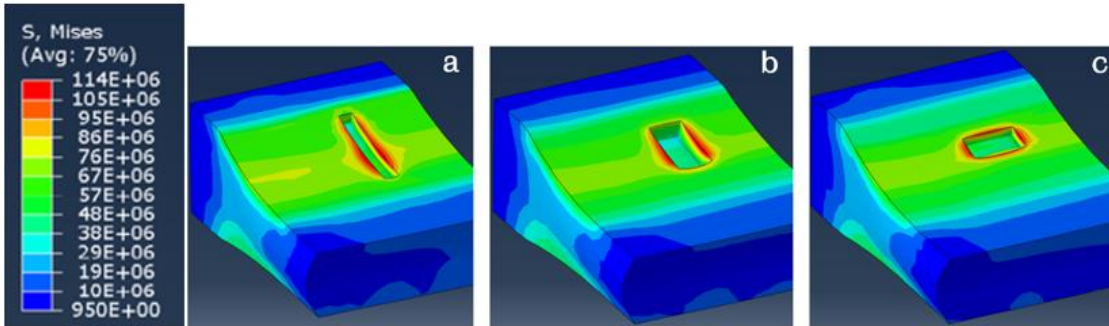
different depths (1mm, 3mm, 5mm), and the extreme combination L/W ratios for the middle value of depth (3mm).

The Table 5.3 shows the initial cavity geometry and dimension of the defects considered.

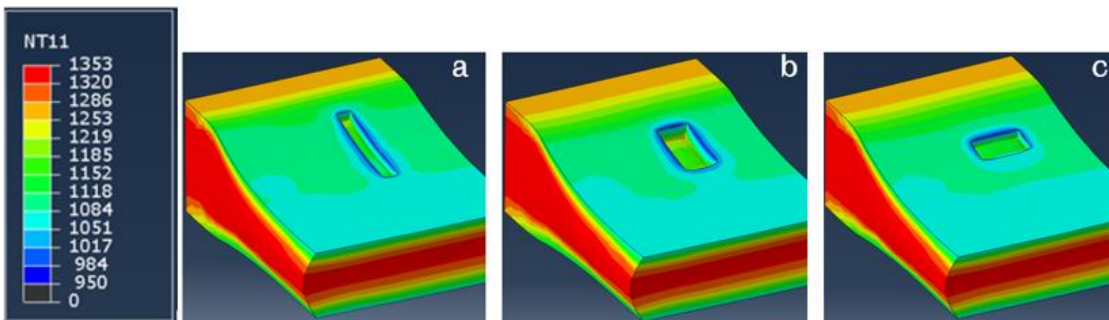
**Table 5.3: Cavity selection for the defect analysis and validation procedure.**

Defect N°	$L_i$ (mm)	$W_i$ (mm)	$D_i$ (mm)	
1- H1	10	7	1	
2- H2	10	7	3	
3- H3	10	7	5	
4- D2	4	11	3	
5- C2	17	3	3	

The behaviour of the defects D<sub>2</sub>, C<sub>2</sub>, and H<sub>2</sub> during rolling is analysed in terms of stress and temperature. The defects were selected to have the same initial depth (3mm), so the effect of different aspect ratio is directly comparable. Figure 5.13 and Figure 5.14 present a top view of the defects present in the slab subjected to hot rolling. Mises stress (Figure 5.13) and temperature (Figure 5.14) fields are reported for the same defects. Lower temperatures in the contact zone of the defect corners are observed, in particular, temperatures up to 100 °C lower than the average temperature in the contact zone are present. This is due to the presence of the cavity, in fact, the free edges of the defect sides cool faster than the rest of the slab because of the less material present. As a consequence, because of the hardening of the material due to the cooling and the accumulation of stresses due to the discontinuity of the contact in the defect sides, a peak of the stress field of about 200Mpa in the borders of the defect is also observable in Figure 5.13.



**Figure 5.13: Mises stress (Pa) field for the cavities  $C_2$  (a),  $H_2$  (b),  $D_2$  (c) during the rolling.**

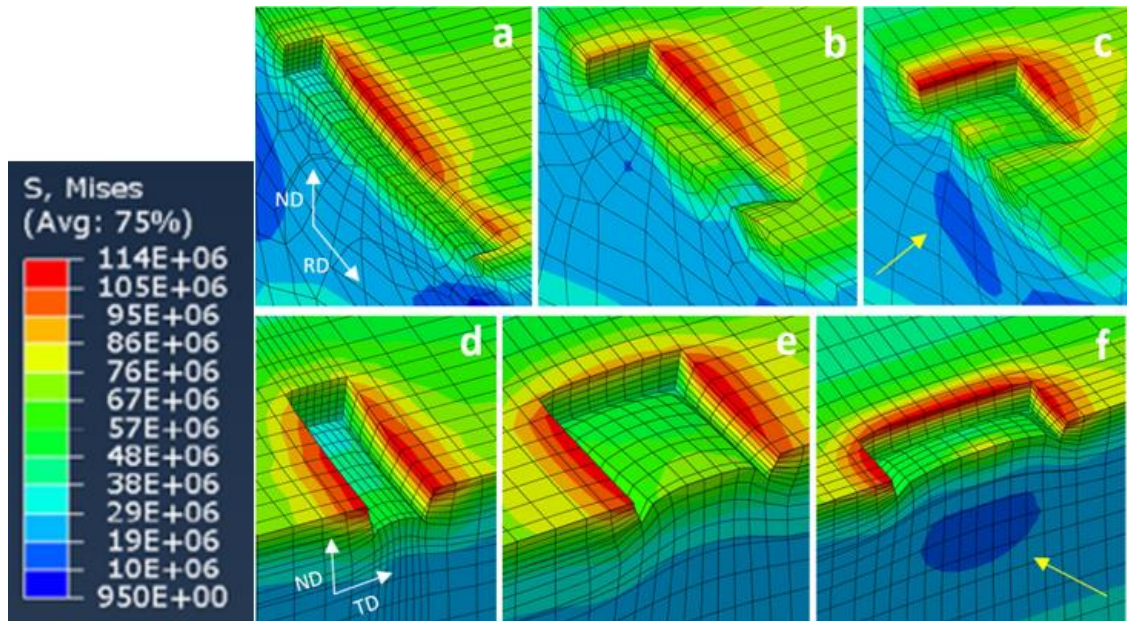


**Figure 5.14: Temperature ( $^{\circ}K$ ) field for the cavities  $C_2$  (a),  $H_2$  (b),  $D_2$  (c) during the rolling.**

The correlation between the stress field and the temperature field is clear comparing the gradients of stress and temperature on Figure 5.13 and Figure 5.14 respectively.

The stress field is also reported in Figure 5.15 for longitudinal (Figure 5.15a-c) and transversal (Figure 5.15d-e) sections of the defects considered. The main finding to emerge is the more bulging of material for the wider defect (Figure 5.15c, f) as expected. The spreading of the material reduced the stress level under the bottom surface of the defect because of the relaxation of the material. The zone at lower stress is highlighted with a yellow arrow in Figure 5.15f and Figure 5.15c.



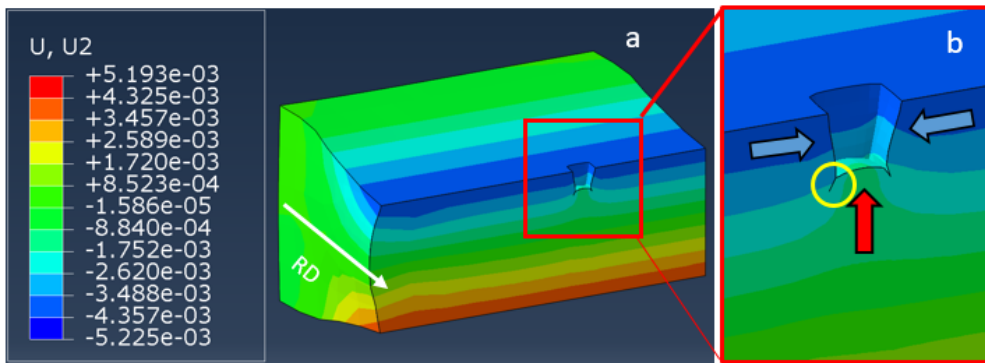


**Figure 5.15: Mises stress (Pa) field longitudinal sections for defects  $G_2$  (a),  $H_2$  (b),  $D_2$  (c), and transversal sections for defects  $G_2$  (d),  $H_2$  (e),  $D_2$  (f).**

To better understand the deformation mechanisms, Figure 5.16 presents the vertical displacement field during rolling in a transversal section of a generic defect (the rolling direction is indicated by a white arrow). It is worth noting that the cavity is affecting the displacement field and the vertical symmetrical deformation and shape of the defect (Figure 5.16b). The lack of material within the cavity leaves space to the bottom of the cavity to spread vertically during the thickness reduction applied by the rolling process. This effect is highlighted with a red arrow in Figure 5.16b.

The buckling of the lateral sides of the cavities generates a lateral spread of the material as highlighted with blue arrows in Figure 5.16b, this effect interacts with the bulging effect of the bottom surface of the defect as previously reported. As a result of this interactions, crevices are formed in the transversal section of the cavities during rolling as highlighted in yellow in Figure 5.16b.

This phenomenon is in agreement with the ones observed during the hot rolling experiment of slabs containing cavities reported in chapter 4.1 and discussed in chapter 7.1.1.

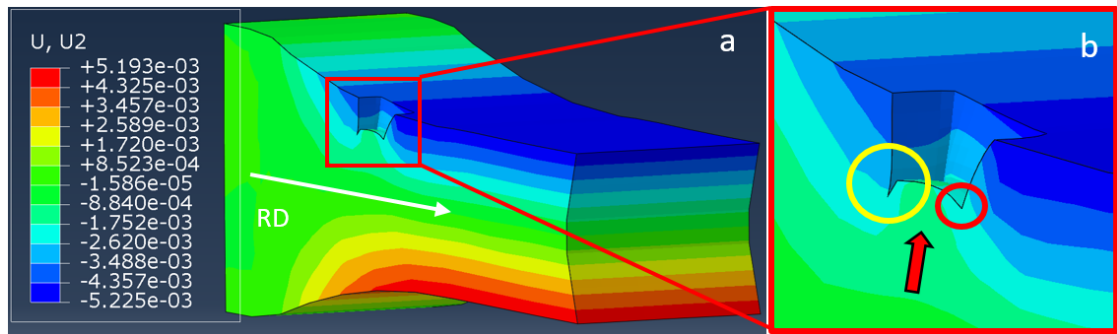


**Figure 5.16: Vertical displacement of a transversal section of the slab containing the defect**

The closure of the crevice is expected to be achieved for higher thickness reductions, or further rolling stands. Higher bulging effects could lead to the direct contact between the roll surface and bottom of the cavity. As a result, potential higher friction coefficients between roll and slab could be achieved.

Similar analysis was carried out in Figure 5.17 for a longitudinal section of the slab containing the same defect. It is worth to notice the spreading of the bottom surface within the cavity indicated with a red arrow in Figure 5.17b.

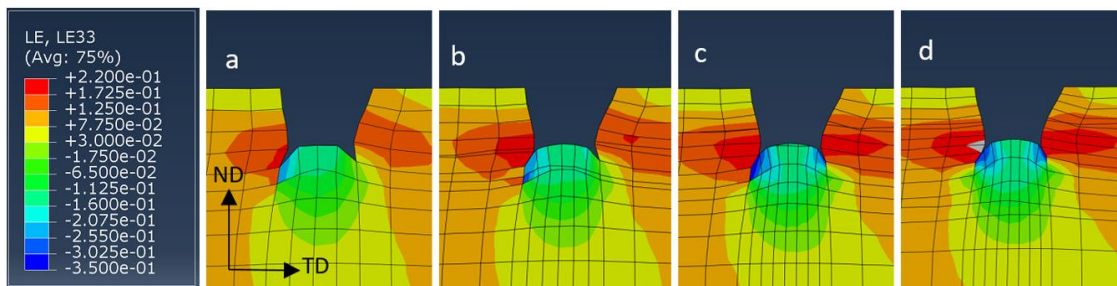
A crevice is forming between the back side and the bottom surface of the defect as highlighted with a yellow circle in Figure 5.17b. However, the crevice formed in the longitudinal section is less severe than the transversal crevices formed (presented in Figure 5.16b). It is worth to notice the front side opening during rolling due to the adhesion between the roll and the slab surface near to the defect side. This forces the front side of the defect to elongate opening the corner formed between the front side and the bottom of the cavity as highlighted in red in Figure 5.17b



**Figure 5.17: Vertical displacement field in a longitudinal cross-section of the slab containing a defect during rolling.**

### 5.7.1 Mesh dependence study

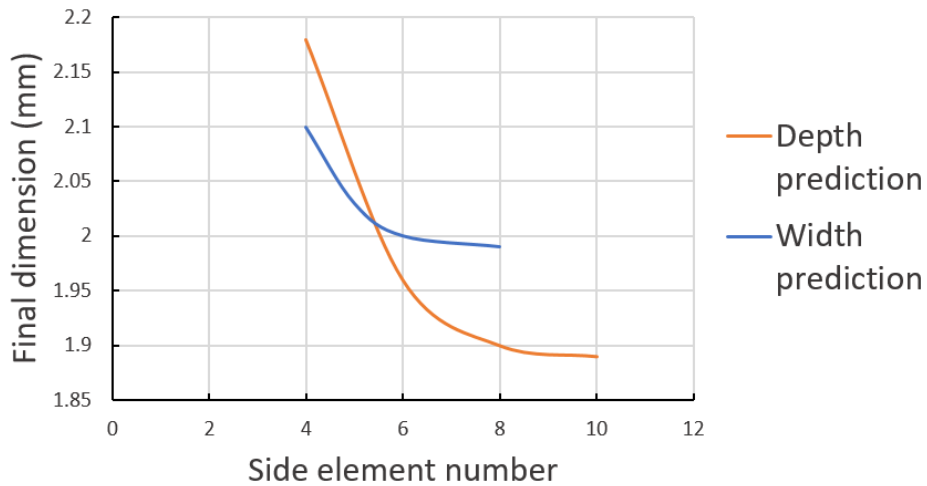
In order to check the mesh dependence of the results, a mesh convergence study was required. Figure 5.18 presents the transversal displacement pattern of a reference defect after being rolled for different mesh refinements.



**Figure 5.18: Defect evolution mesh dependence for different mesh refinement. The letters indicate different mesh refinements.**

Four different mesh cases were compared where the number of elements on the vertical side of the cavity were 4, 5, 6 and 8, while the element number on the bottom side of the cavity were 4, 6 and 8. As can be seen, coarse mesh prevent the bulging of the bottom of the cavity and the buckling of the lateral sides. A clear convergence on the strain pattern and on the defect final shape of the lateral sides of the defect when the number of elements is 6 at least (Figure 5.18c) is also observable.

A quantitative analysis can be carried out measuring the width and the depth of the cavity for different element number present on the sides. This analysis is presented in Figure 5.19.

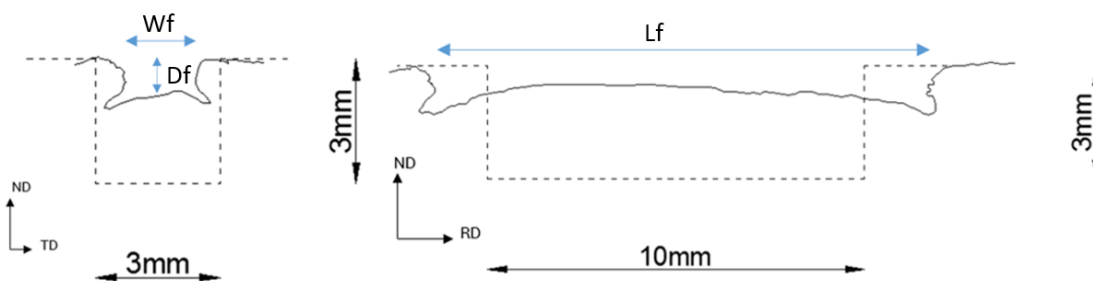


**Figure 5.19: Quantitative mesh dependence analysis**

As noticeable on Figure 5.19, the results of the prediction of width and depth of the defect converge for elements number higher than 6 and 8 on the lateral and bottom side of the cavity, respectively. For this reason, a total number of 6 on the vertical sides of the defects and 8 on the bottom sides of the defect is guaranteed for the cavities considered.

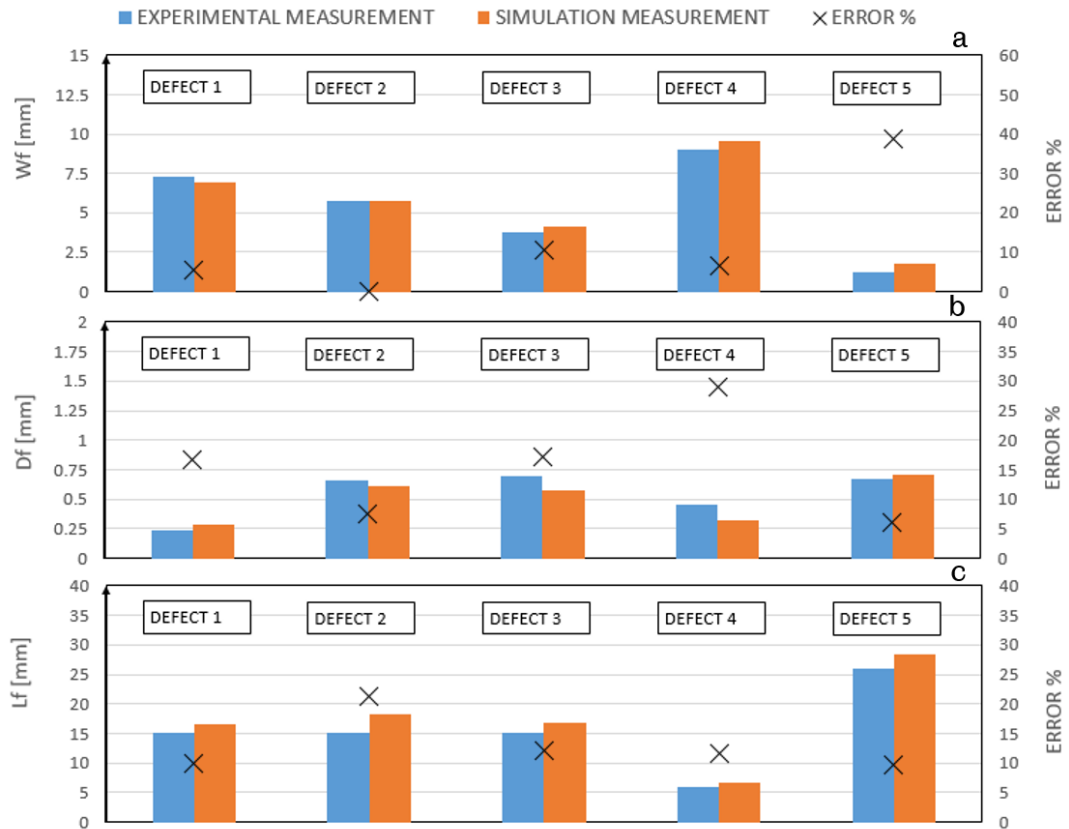
### 5.7.2 Validation

To validate the model and check the accuracy of the predictions, the final defect geometry was compared between the model and the experiment for the five defects considered. The measurement scheme adopted to determine the final width ( $W_f$ ), length ( $L_f$ ) and depth ( $D_f$ ) is presented in Figure 5.20 for a generic defect.



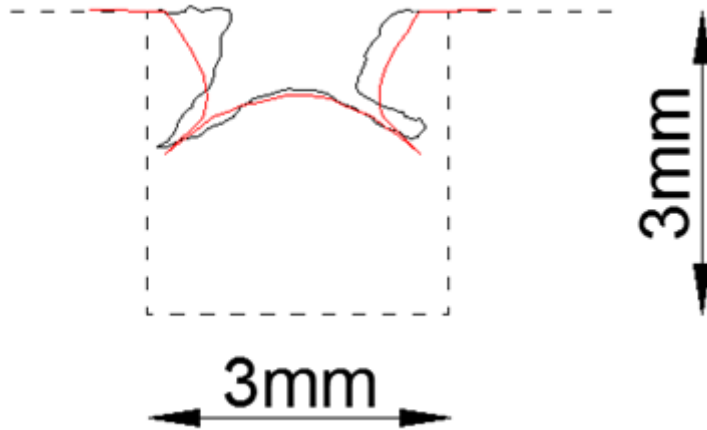
**Figure 5.20: Measurement scheme used for a generic defect to estimate the defect dimensions, transversal (left), and longitudinal (right) sections.**

Figure 5.21 presents three different series of comparison between the final width, depth and length predicted and the same measurements taken from the deformed cavities after the experiment. The error of the model prediction is reported in the secondary axis and it is indicated with a black cross.



**Figure 5.21: Comparison between measured and predicted values of (a) final width, (b) final depth and (c) final length, the error of the prediction is indicated with a black cross.**

The comparison of the measured final dimensions of the defects presented in the figure shows a good match for most of the defects, the worst case encountered was the width of the defect 5 in Figure 5.21a, with an error of 38.9% on the prediction. A comparison between the predicted and the observed transversal sections of the defect 5 is presented in Figure 5.22. As can be seen from the figure, the reason of such a large error is general the under prediction of the transversal buckling of the lateral sides of the cavity. The error measured is relatively large because of the small initial width of the cavity.

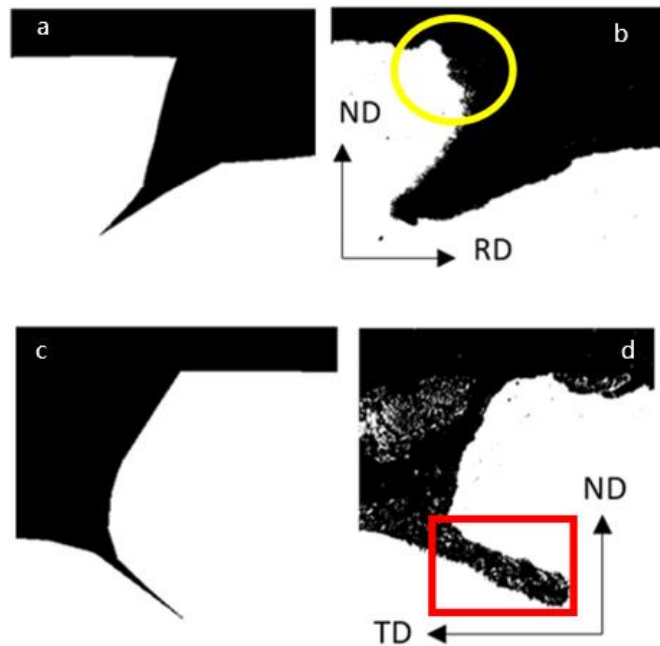


**Figure 5.22: Transversal section of defect C2 comparison between, the initial cavity shape (dashed line), the predicted (red line) and the observed (continuous black line) defects.**

In general, it is noticeable that the model is slightly over predicting the final length and the final width for most of the defects. The average of all the predicted dimensions errors is about 14%.

A geometrical comparison between the final defect conformation and the model prediction is reported in Figure 5.23 where transversal and longitudinal sections are compared. Figure 5.23 presents the final configuration of the defect C2, Figure 5.23a presents the model prediction of the longitudinal back section of the defect and it is compared with the micrograph of the same section (Figure 5.23b). A similar comparison is done between Figure 5.23c and Figure 5.23d for the transversal section of the same defect.

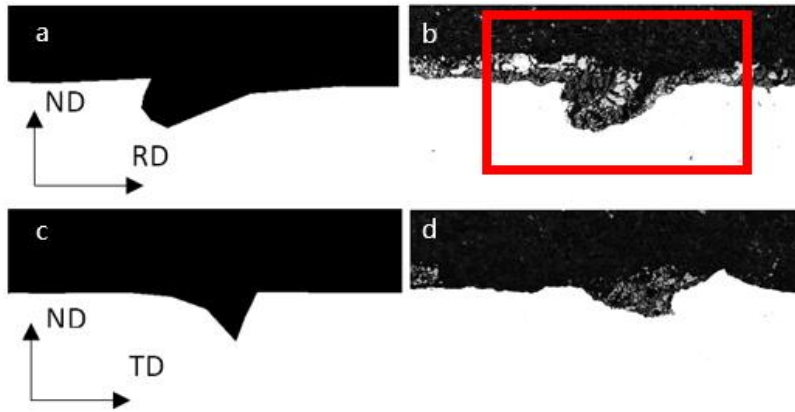
It is worth to notice the presence of oxide inside the defect and crevices formed during the deformation as highlighted in red in Figure 5.23d. This effect is not observable in the model as oxide layers were not simulated. Another interesting outcome is the difference in the shape of the corner in the top surface of the defect highlighted in yellow in Figure 5.23b. This was probably due to oxidation and consequent consumption of the metal during the heating. As a consequence, the cavity initial shape was different with respect to the expected milled initial cavity.



**Figure 5.23: C2 defect, longitudinal back section (a) simulated and (b) observed with the microscope; transversal section (c) simulated and (d) observed with the microscope.**

A similar comparison is presented in Figure 5.24 and Figure 5.25 for defect H1 and H2 respectively. Figure 5.26 present the transversal section comparison between the model and the micrographs. It is worth to notice the homogeneous oxide layer highlighted in red in Figure 5.24b, in this case, the match with the model prediction was very good. In transversal section presented in Figure 5.24d, the discontinuous presence of oxide between the inside and the outside of the cavity altered the final defect conformation.





**Figure 5.24: H1 defect, longitudinal back section (a) simulated and (b) observed with the microscope; transversal section (c) simulated and (d) observed with the microscope.**

With regards to the defect H2 presented in Figure 5.25, the buckling of the vertical sides is slightly under predicted in the transversal and longitudinal section, this effect is also observable for the defect C2 in Figure 5.23. However, the deformation mechanisms are in agreement.



**Figure 5.25: H2 defect, longitudinal back section (a) simulated and (b) observed with the microscope; transversal section (c) simulated and (d) observed with the microscope.**





**Figure 5.26: D2 defect, transversal section observed with the microscope (a) and simulated (b).**

The geometrical comparison between the model and the experiment are satisfactory as the model is reproducing the deformation mechanisms manifested during the defect evolution hot rolling experiment. Overall, the agreement of the cross-section shape between model and experiment is remarkable considering the very small size of the cavities considered.

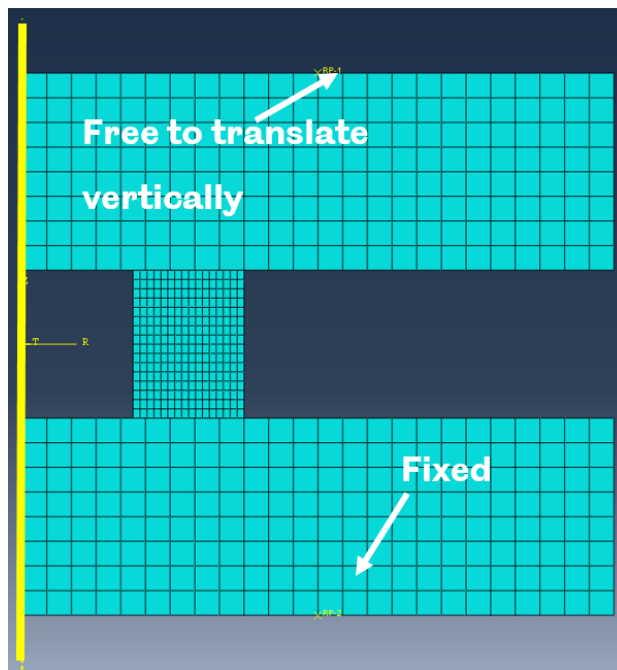
### **5.8 Isothermal hot ring compression test: Temperature dependence of friction for a real scale hot rolling process**

In order to obtain the calibration curves necessary to evaluate the friction coefficient present during the hot ring compression test carried out at different temperatures, a 2D axisymmetric model of the ring was developed using the Abaqus package. In this model, rings were compressed at different friction conditions and calibration curves were obtained for each of the frictional condition considered.

The axial symmetry of the ring was considered to simplify the model, the axisymmetric axis is represented in yellow in Figure 5.27. A homogeneous mesh of quadrilateral 4-node thermally coupled axisymmetric elements was used for the modelling of the rings, with the elements dimension being 0.375 mm and 0.281 mm in the vertical and transversal direction respectively. Bigger squared

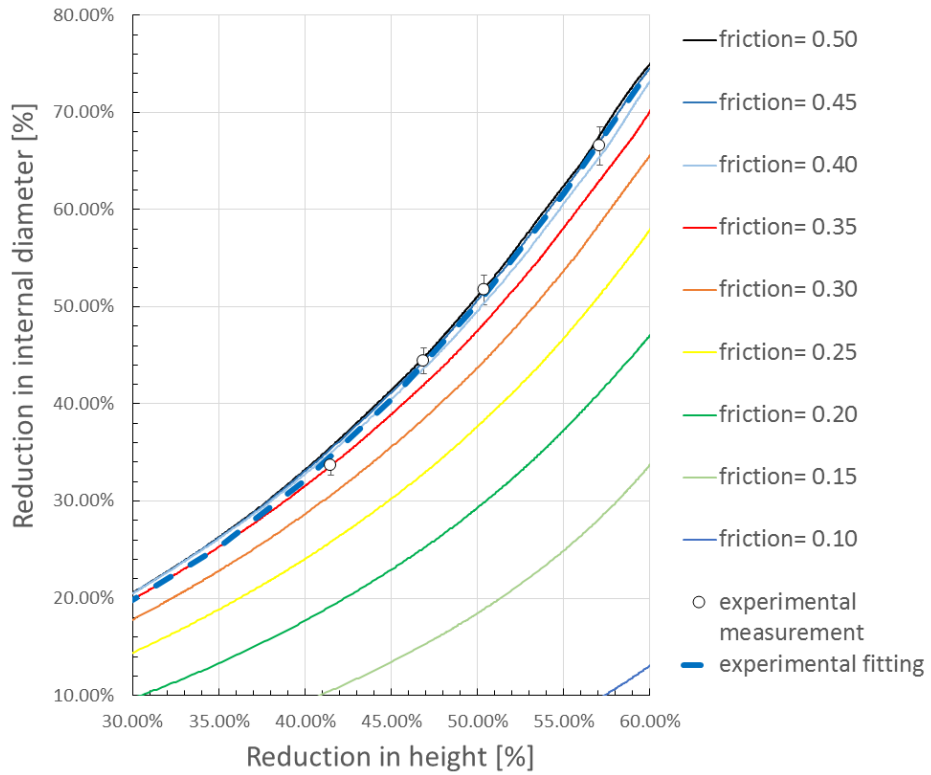
elements of 1 mm were used for the compression tools which were assumed to be rigid. The bottom tool was rigidly constrained to a fixed reference point, on the contrary, the top tool was constrained such that the only degree of freedom allowed was the vertical translational as shown in Figure 5.27.

Coulomb friction model was used to simulate the friction behaviour at different friction coefficients. The material was modelled using the Sellars and Tegart model for strain rate and temperature dependent materials. Details of the material model used can be found in chapter 5.1.

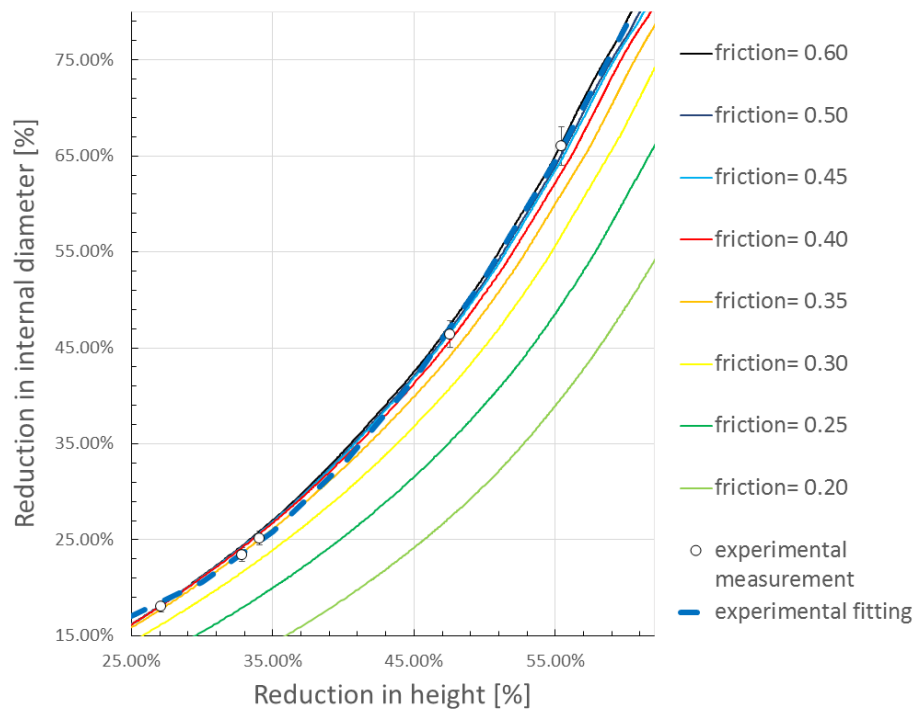


**Figure 5.27: Axisymmetrical model used to reproduce the hot ring compression test.**

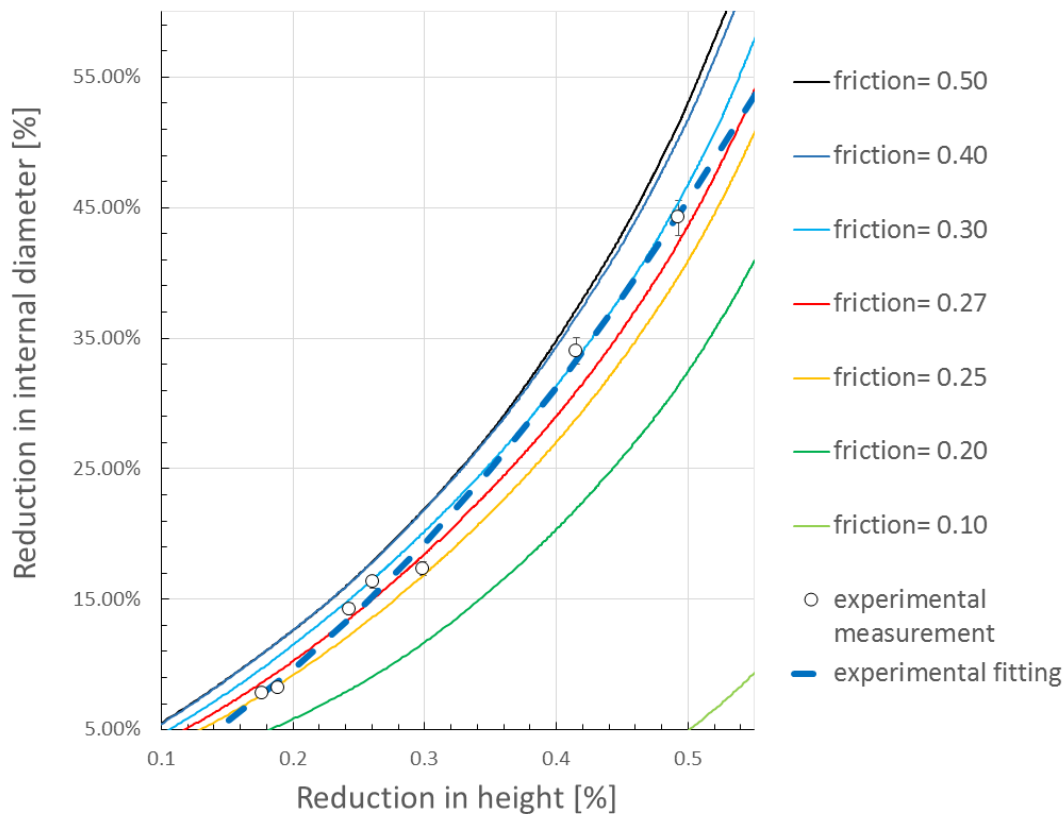
Curves representing the percentage of height reduction against the percentage of diameter reduction for various friction coefficients and temperatures obtained from the models are shown together with the experimental measurements. Three different graphs (Figure 5.28-28) are used to present the behaviour at three different temperatures (1050°C, 950°C and 850°C, respectively). Different colours are used to indicate the calibration curves obtained with different friction coefficients. Experimental ring measurements are indicated with white points in the graph, a blue dashed line is used to fit them.



**Figure 5.28: Friction calibration curves and experimental measurements for an isothermal compression test done at 1050 °C.**



**Figure 5.29: Friction calibration curves and experimental measurements for an isothermal compression test done at 950 °C.**



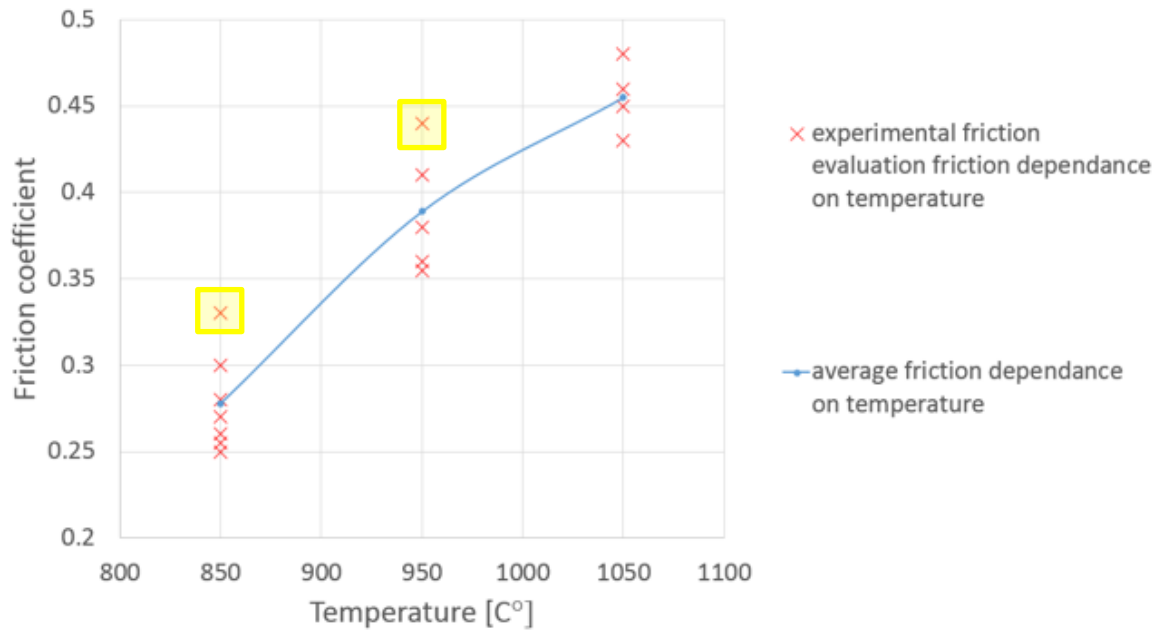
**Figure 5.30: Friction calibration curves and experimental measurements for an isothermal compression test done at 850 °C.**

The comparison between measurement and calibration curves indicates that the experimental points are following the curves trend. This confirmed that a constant friction was present during the compression.

Friction was estimated comparing the experimental fitting curve (dash line) with the calibration curves for each graph produced at different temperatures.

It is worth to notice that friction increases with temperature, in fact in the Figure 5.28 related to tests done at 1050 °C the fitting curve of the experiment coincides with the calibration curve of the modelling results with friction coefficients within a range of 0.4 and 0.5. The friction ranges obtained from the calibration curves at 950 °C (Figure 5.29) and at 850 °C (Figure 5.30) were 0.35-0.45 and 0.25-0.30 respectively. To better appreciate this trend, friction coefficients values estimated for each ring measured were plotted together for different temperatures in Figure 5.31. This was done to highlight relations between friction and temperature. A trend line is plotted revealing the dependence of the friction

on the temperature. Friction values which were excessively far from the average are highlighted by yellow boxes and relative rings are analysed in the discussion chapter 7.1.4.



**Figure 5.31: Friction coefficient measured at different temperatures.**

Overall, it is noticeable that there is almost a linear dependence between the friction coefficient and the temperature. Friction was measured ranging between 0.25 and 0.47, however, the average of the friction measured at 850°C, 950°C and 1050°C were 0.27, 0.38 and 0.45 respectively. The temperature dependent friction coefficient can be used to simulate the contact in a model reproducing a full-scale industrial hot rolling process where similar oxide thickness as the one encountered during the descaling experiment are present (this was done for a full-scale hot rolling process in chapter 6).

## 6 HOT ROLLING PROCESS MODEL

The results obtained from the laboratory mill presented in chapter 4 may be significantly different to the ones experienced from real scale hot rolling process. In fact, differences in term of roll diameter, thickness reduction, the velocity of the process and cooling rates between two processes can really affect the defect evolution during rolling.

Not to be neglected are the differences in the relative dimension of the defect with respect to the slab thickness and roll diameters between the lab mill and the real scale industrial process. In fact, the initial thickness of the slabs before the rolling in the specific hot rolling process considered is 70mm compared to the 25mm of the samples used in the experiments and in the models. Hence, considering an initial defect reference depth of 5mm, the ratio between the slab thickness and the defect depth is 14 and 5 for the real scale process and lab mill experiment, respectively.

With regards to the rolls, diameters of 1018mm are considered for the real scale industrial process which is about four times larger than the diameters of 223mm of the mills used in for the lab experiments and related simulations. Again, considering an initial defect reference depth of 5mm, the ratio between the mill diameter and the defect depth is 204 and 45 for the real scale process and lab mill experiment, respectively.

Differences in scale are expected to lead to different results despite the same thickness reduction ratio of 40% is applied for both the cases. For this reason, the modelling of the defect evolution in a real scale was essential.

The aim of modelling a real scale hot rolling process is to study the effects of different geometrical shapes of initial cavities and process parameter on the final defect severity. In this context, cavities of different geometries were studied to check the effect of the geometry on the deformation mechanisms and severity of the final feature generated. In addition, sensitivity studies of different rolling process parameters on the final defect severity were carried out and the results are presented in this chapter.

## 6.1 Methodology

A three-dimensional model reproducing a generic full-scale rolling process is presented. The model was produced following the same assumptions made for the laboratory mill hot rolling process simulations (chapter 5). Two additional simplifications were applied:

- Because of the larger thickness of the slab of the full-scale rolling process considered (70mm compared to 25mm of the lab mill experiments), the presence of the defect was assumed to have a negligible effect on the neutral plane of the slab. For this reason, the horizontal symmetry of the process was assumed, and only one roll and half of the slab were modelled.
- Considering the full width of the slab of the full-scale rolling process considered (about 1000mm) and assuming that defects are present in the central band of the slab, the effect of the lateral spreading of the material in the central zone of the slab can be neglected. Therefore, two vertical symmetries were introduced to the model. For this reason, defects are assumed centred in the slab in such a way that only half of the defect is modelled as shown in the mesoscale model presented in Figure 6.2.

### 6.1.1 Material model

The rolling mills and the slabs were modelled accordingly to the approaches used to model the lab rolling mill process (chapter 5). The mill was considered rigid and only the thermal degree of freedom was taken into account. The slab was modelled according to the Sellars and Tegart (S&T) [99] temperature-displacement coupled material model.

### 6.1.2 Loads, contact interactions and boundary condition

The load history for the rolling simulation consisted of three steps. In the first step, the slab which has an initial temperature of 1150°C was subjected to heat

loss due to radiation to the environment in order to reduce the surface temperature of about 100°C. The final surface temperature of 1050°C was the temperature measured at the top surface of the slab in the full-scale hot rolling process just before the rolling of the slab. In the second step, an initial velocity of 0.1m/s in the rolling direction was imposed to the slab; this was necessary to initiate the rolling deformation of the slab when the contact with the mill is reached. In the third step, an initial rotational velocity of 1m/s of the mill was defined. The combination of pressure and friction between slab and mill guaranteed the slab fed into the roll gap. The same load steps and interaction are used for the mesoscale model

With regard to the interactions between slab and roll, same approaches used for the lab mill model were applied for heat conduction and frictional model. The only difference between the two models is the value of the friction coefficient which is now assumed temperature dependent accordingly to the outcome of the isothermal ring test presented in chapter 5.8.

Equation 6.1 presents the Coulomb friction model used.

**Equation 6.1**

$$\tau = \min(\mu(T) \cdot p; \tau_{lim})$$

The friction coefficient dependence of temperature is based on the graph presented in Figure 5.31, a table was built where values of friction are presented for different temperatures. The code used this data to vary the friction coefficient in the contact according to the slab temperature.

### **6.1.3 Macroscale hot rolling model**

The macroscale model is made of two parts that are in contact each other, the rolling mill and the slab (squared toroidal roll and a rectangular cuboidal slab).

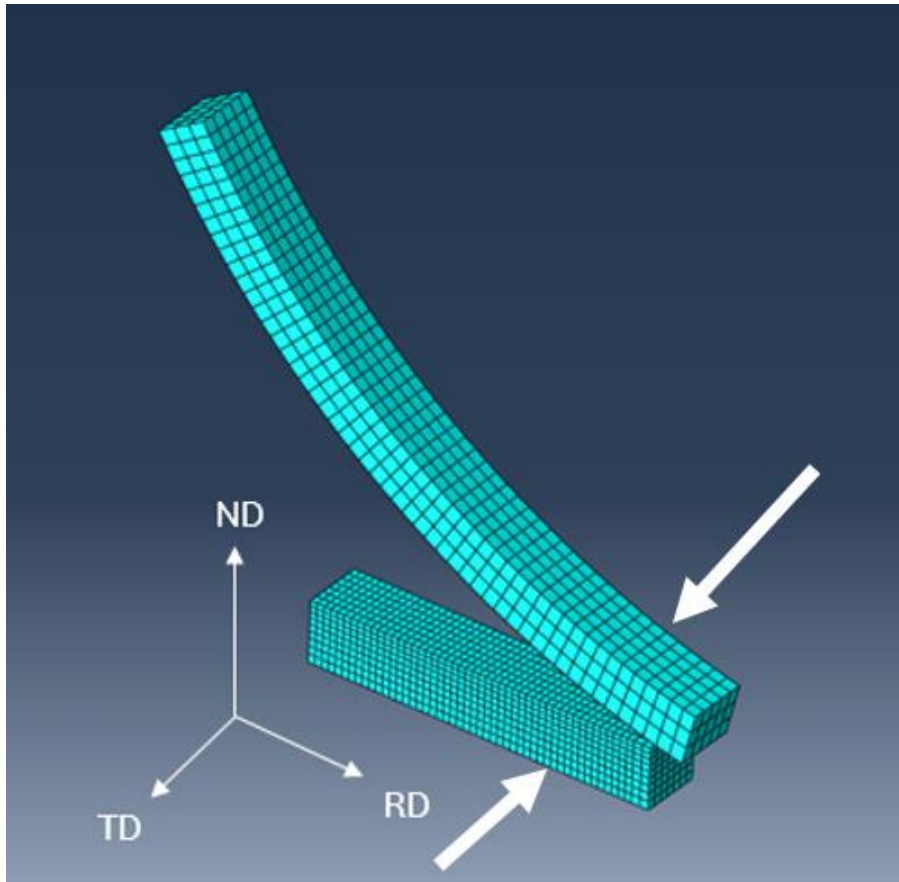
The main geometrical features of the parts considered are as follows:



-Roll diameter ( $d$ ): 1018 mm; Thickness in ( $th-i$ ): 70 mm; Thickness out ( $th-o$ ): 42 mm;

The rolling mill is a toroid with a squared section meshed with 8-node thermal stress coupled hexahedral linear elements. The radial thickness of the toroid is 30mm, sensitivity studies were carried out to ensure that the given thickness was enough to guarantee the proper internal heating during the contact.

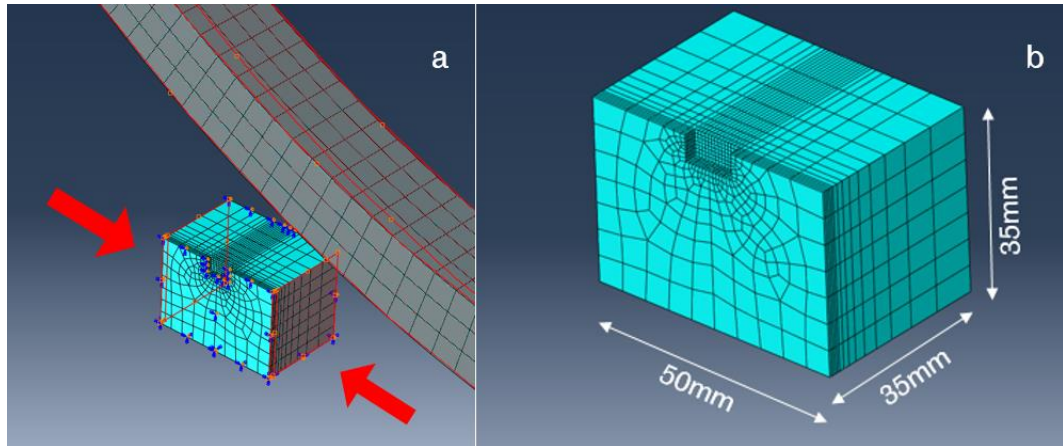
The length of the slab considered is only 200mm, for this reason, only an eighth of the mill is modelled to roll the full slab. A ratio of about 4 between the size of elements in the roll and the size of the elements in the strip is guaranteed in the contact zone. The element dimensions provided were obtained through a mesh convergence study. The elements dimension in the roll is 7mm in the transversal and tangential directions and 10 mm in the radial direction. The elements dimensions in the slab is 5mm in the transversal direction, 4mm in the rolling direction, a light transition between 5mm and 3mm in the normal directions of the elements is defined to better appreciate the strain deformations of the slabs in the contact zone. The slab is meshed with 8-node thermal stress coupled hexahedral elements. Reduced integration elements with a specific hourglass stiffness were used to avoid the shear locking effect. According to the Abaqus manual [100], hourglass stiffness is defined to be  $0.005G$ , where  $G$  is the shear modulus at specific temperature. Figure 6.1 presents the mesh used to simulate the macro scale model of the first stand of the hot rolling process. The vertical symmetric planes are indicated with two arrows:



**Figure 6.1: Hot rolling macroscale model**

#### **6.1.4 Mesoscale hot rolling model**

The mesoscale model is made of two parts in contact with each other, the slab subvolume containing the defect, and a portion of the roll which is assumed rigid. The mesoscale model mesh is presented in Figure 6.2. Figure 6.2a presents the two boundary surfaces of the mesoscale model where the solutions of the macroscale model were applied (as indicated by the red arrow and red surfaces). Figure 6.2b highlights the mesh used to represent a generic cubical defect. Hexahedral elements of about 0.6mm and 3.5mm are used on the defect surfaces and on sub model external faces respectively. The element dimensions are obtained from a mesh convergence study. A transition mesh is designed between the sub volume external face and the defect. As shown in Figure 6.2a, the results of the macroscale model were also applied to the rolling mill.



**Figure 6.2: Hot rolling mesoscale model, (a) boundary surfaces, and (b) submodel detail mesh scheme.**

A similar procedure to the one used for the lab rolling process was carried out to check the accuracy of the multilevel approach. It was confirmed that a reduced length of 50mm in the rolling direction was enough to guarantee that all the defect represented were not affecting the stress or the thermal field at the boundaries.

## **6.2 Process parameters study**

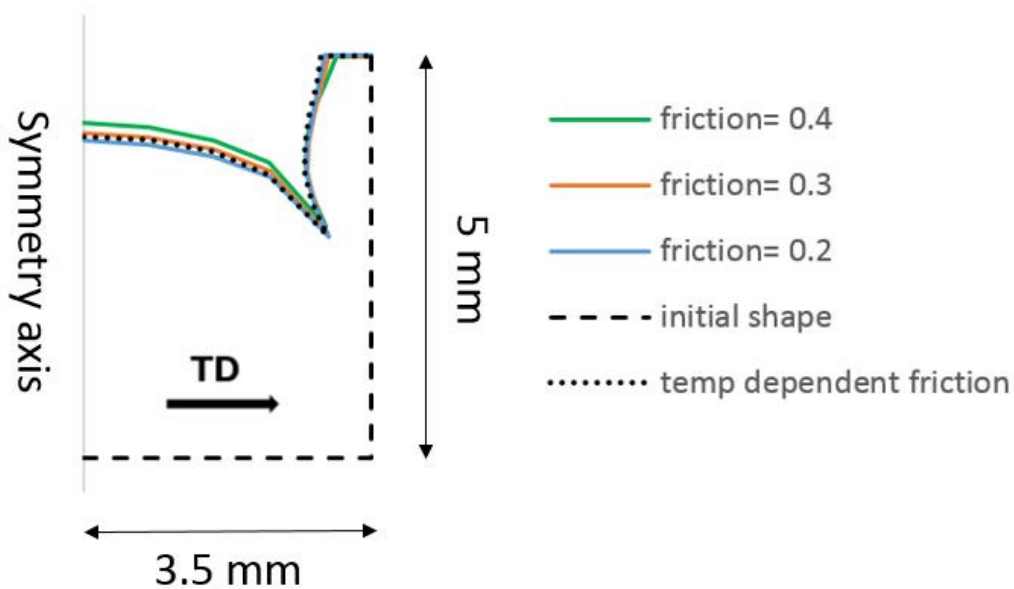
The effect of different process parameters including different friction coefficients, different initial temperatures of the material and different reduction ratio are compared for the same initial cavity. The dimension of the cubical initial cavity is defined as  $L=10\text{mm}$ ;  $W=7\text{mm}$ ;  $D=5\text{mm}$ , where the values for length and width are the mean values measured from the 3D scan of slabs containing defects as explained in (chapter 3.1).

### **6.2.1 Results**

Figure 6.3 presents the transversal section of the cavity before and after rolling for different friction coefficients present. The initial shape of the cavity is represented by a dashed line, the final shape of the defect is represented with different colours to indicate the different friction coefficients used during rolling. A pointed line is used to describe the shape of the defects when a

temperature dependent friction coefficient is used. For an accurate description of the temperature dependent friction coefficient used see chapter 4.8.2.

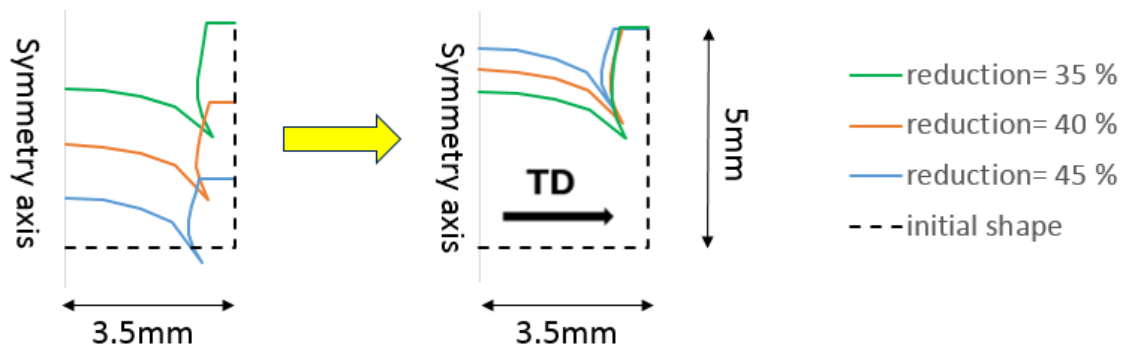
From the figure, it can be noticed that different values of friction during the rolling resulted in slight different final defect conformation. In particular, it seems that higher friction coefficients increase the buckling of the lateral sides and the bulging of the bottom surface of the defect. With regard to the results obtained using the temperature dependent friction coefficient, it is worth notice that the defect evolution is not altered substantially. In particular, the effect of the temperature-dependent friction is similar to the effect obtained with a coefficient of friction whose value is between 0.2 and 0.3.



**Figure 6.3 Effect of different friction coefficient on the final transversal section of the defect.**

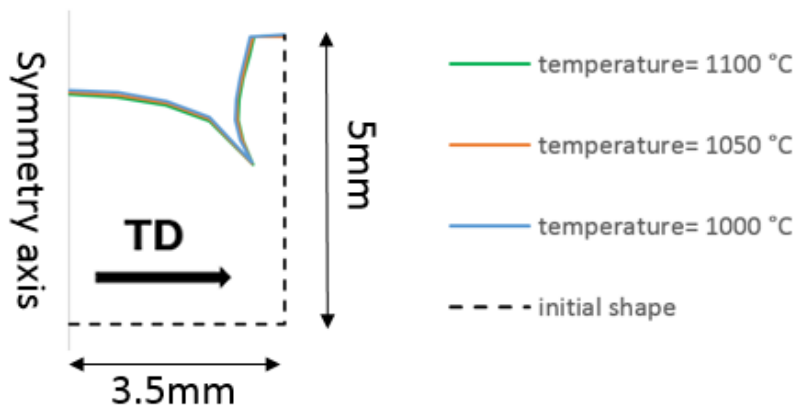
Figure 6.4 presents the effect of different rolling reduction ratios on the defect geometry evolution. The left side of the image presents the final defect transversal sections for different reduction ratio indicated by different colours used. On the right side of the image, the defects are aligned with respect to the top surface of the slab. This was done to compare the severity of the final configurations. From the image, it can be observed that more buckling of the lateral sides is present for higher thickness reductions. In addition, as expected,

the final depth of the defect decreases for higher thickness reductions of the slab.



**Figure 6.4 Effect of different reduction ratios on the final transversal section of the defect.**

Figure 6.5 presents the effect of different initial temperatures of the slab before the rolling, ranging between 1000°C and 1100°C. As can be seen from the figure, negligible differences were found between the cases taken into account.



**Figure 6.5 Effect of different slab initial temperatures on the final transversal section of the defect.**

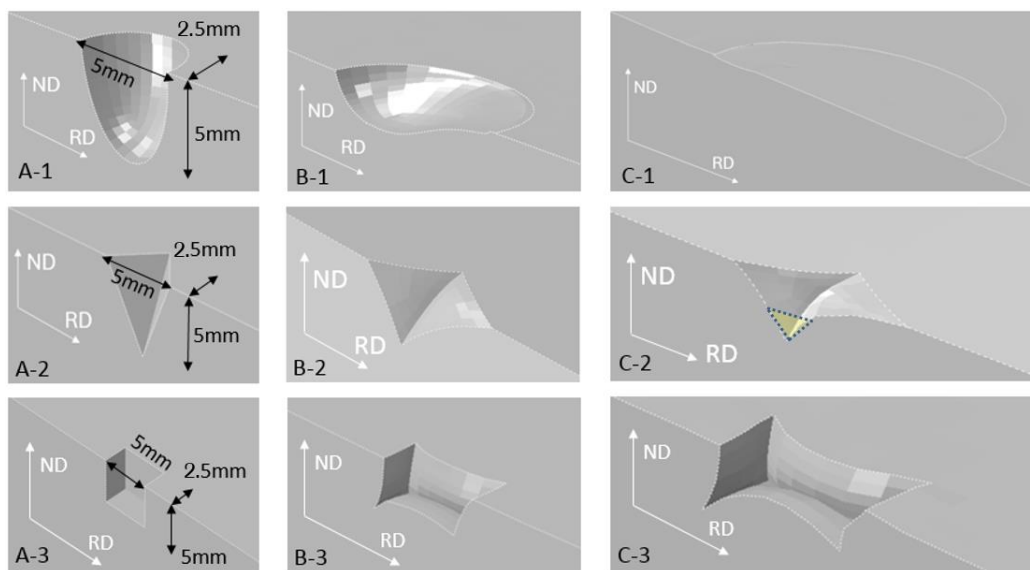
### 6.3 Geometrical study

The evolution of different initial geometrical features was analysed for constant process conditions. This was done to obtain further insight on the dependence of the geometrical shape of the cavity on the evolution mechanisms during the hot rolling process. The evolution of three different geometries including

pyramidal, spherical and cuboidal of same reference initial dimension were compared during rolling.

### 6.3.1 Results

Figure 6.6 presents the state of the cavity before, during and after the rolling. The process parameters are the same presented in (chapter 5). The defects had an initial reference depth, width and length of 5mm for all the geometries as indicated in Figure 6.6. This was done to avoid the effect of different aspect ratios on the defect evolution.

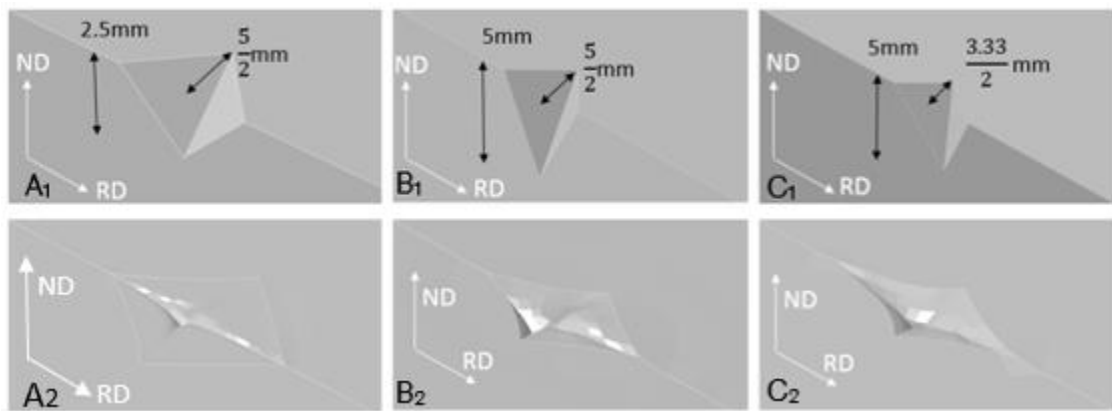


**Figure 6.6: Spherical, pyramidal and cuboidal defect cavities before (A), during (B) and after (C) hot rolling.**

As Figure 6.6 shows, different geometries evolved differently, in particular, the spherical and pyramidal cavities tend to be opened due to the elongation in the rolling direction (Figure 6.6-B<sub>1</sub>, and Figure 6.6-B<sub>2</sub>) and flattened due to the reduction in thickness (Figure 6.6-C<sub>1</sub>, and Figure 6.6-C<sub>2</sub>). A small crevice was formed in the bottom apex of the pyramid due to the lateral buckling of the sides as highlighted in Figure 6.6-C<sub>2</sub>. With regards to the cubical cavity, it is worth to notice the crevice formed in the longitudinal and transversal direction. As expected, the bulging of the material from the bottom of the defect, and the buckling of the lateral sides interact together generating irreversible critical

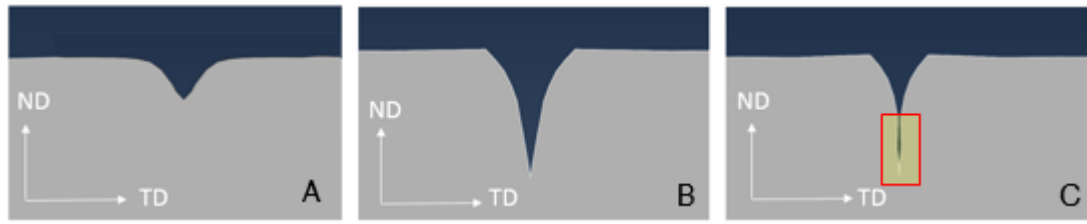
crevices. As a consequence of this, the cubical geometry is considered the most critical to be eliminated through rolling.

Further modelling involving the pyramidal and cubical initial geometry were carried out to further examine the crevice forming phenomenon. The effect of different depth to width aspect ratios of the pyramidal cavities was studied to identify the eventual threshold value of aspect ratio which ensures the complete opening of the defect. The Figure 6.7 presents the defects before ( $A_1; B_1; C_1$ ) and after the rolling ( $A_2; B_2; C_2$ ). Depth to width aspect ratio considered are as follows: 0.5 (defect A); 1 (defect B); 1.5 (defect C).



**Figure 6.7 Pyramidal defects of different aspect ratio before (longitudinal section) and after rolling (whole defect).**

As Figure 6.7 shows, the aspect ratio plays an important role in the final severity of the defect. The severity of the defects increases with the depth to width aspect ratio of the initial pyramidal cavities. This is noticeable comparing the final state of the defects. Higher depth to width aspect ratio resulted in more buckling of the lateral sides of the defects resulting in crevices formed in the bottom tip of the pyramid. To better show how the defect is deformed, the final transversal sections of the three pyramidal defects considered are compared in Figure 6.8. Defects A, B and C represent the pyramidal defect with an initial aspect ratio of 0.5, 1 and 1.5 respectively.



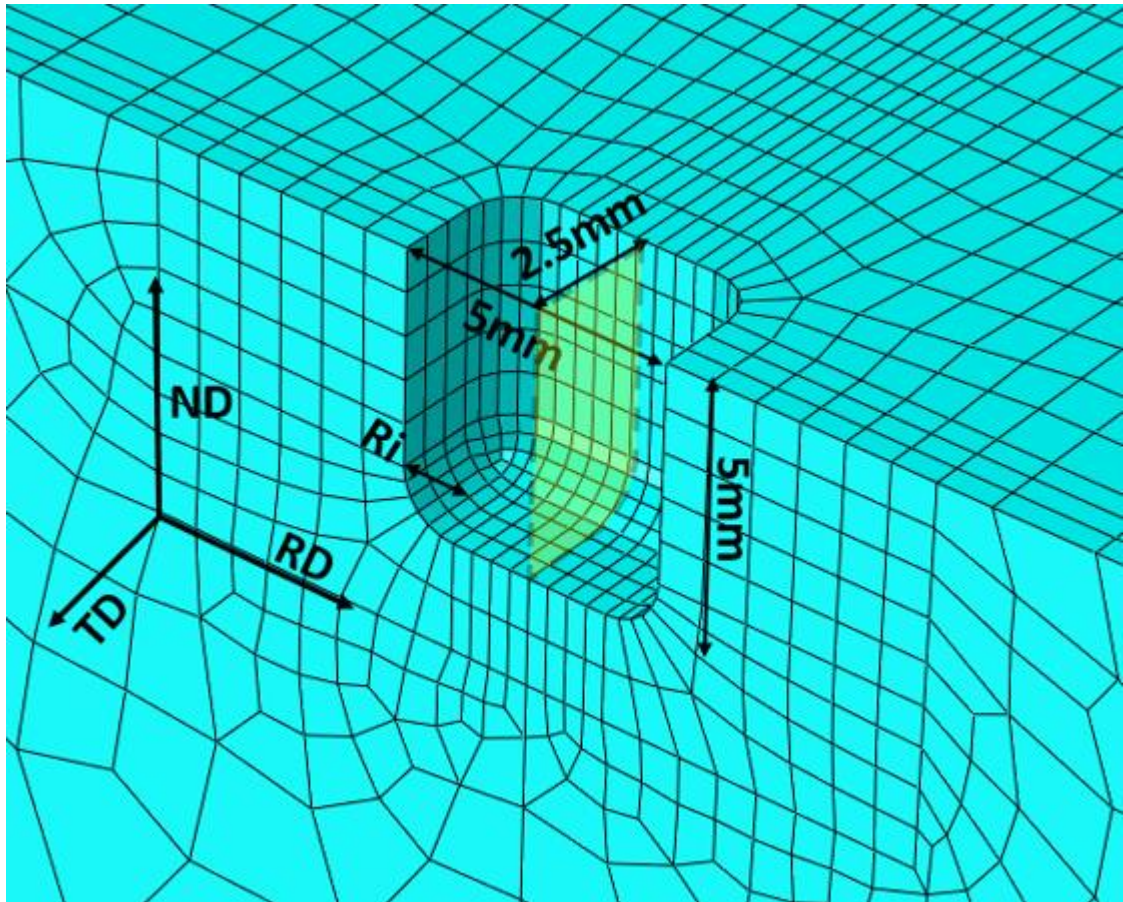
**Figure 6.8 Transversal section comparison of pyramidal defects of different initial aspect ratio.**

Lower aspect ratios resulted in more opening of the defects and flattening during rolling. In particular, the initial defect with an aspect ratio of 0.5 (defect A) was almost completely opened as shown in Figure 6.8-A and further reduction in thickness are expected to flatten the defect completely. Crevices are formed when the depth to width ratio was 2 as highlighted in Figure 6.8-C.

With regards to the cubical features, the same cubic cavity of 5mm used in the previous analysis was studied for different fillet radius of the corners. This was done to understand the role of the initial corner radius of the defect on the initiation of the folding of the surfaces and respective crevice forming.

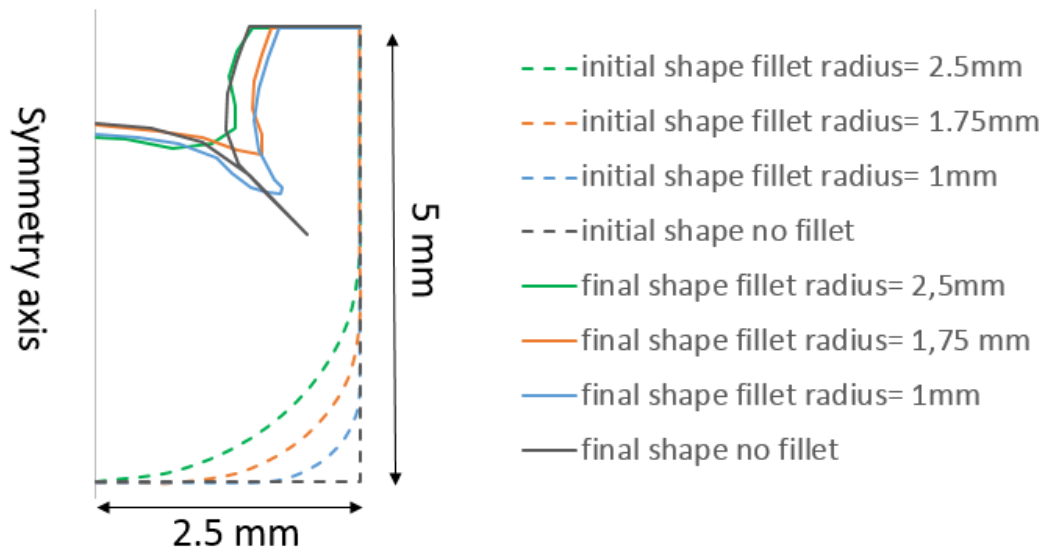
In this context, a transversal section of the defect was analysed for different fillet radius applied at the same cubical defect. Figure 6.9 shows the generic mesh used and the transversal section considered is highlighted in yellow. A minimum number of 6 elements are used to model the circular filled radius. It is important to notice that the fillet was applied on every corner of the cubical defect.





**Figure 6.9 Mesh scheme used to study the effect of different fillet radius on the final defect conformation.**

The Figure 6.10 shows a comparison between the initial cavity and the final defect transversal section for a constant hot rolling process and different initial fillet radius. The values of the initial radius were 1mm, 1.75mm, 2.5mm, and the cavity depth was 5mm for all the cases. The extreme case without the corners fillet was also compared. It is worth to notice the strong difference between the behaviour of the cavity with the filled corners and the extreme case of right angle cavity. When fillet is not present, the crevice is easily formed and high buckling and bulging of the lateral and bottom surface is manifested. As the fillet radius increase, the buckling and bulging are gradually reduced. In particular, for the case of a filled radius of 2.5mm (which was half of the cavity depth), the lateral buckling and the bottom bulging of the material is prevented and crevices are not formed.



**Figure 6.10 Effect of different fillet radius on the final transversal section of the defect.**

## 7 DISCUSSION

### 7.1 Experimental discussions

#### 7.1.1 Defect evolution during rolling discussion

The geometrical deformation trends reported in the previous section are discussed in this section and a regression equation is proposed to predict the final dimension of the defect in function of initial D, W and L dimensions.

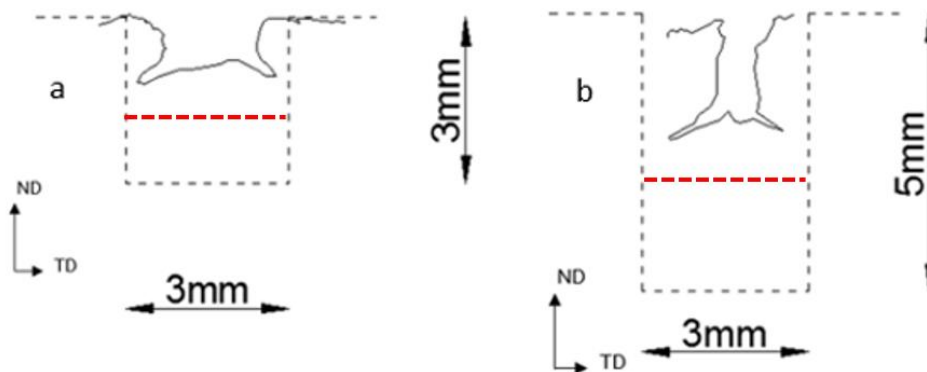
#### **Geometry analysis:**

The initial geometry of the surface cavities plays an important role in the evolution mechanisms during rolling affecting the final configurations. The observed deformation phenomena, in particular, the side wall buckling and removal of defects with a small initial depth, are in a good agreement with the literature [101] where a multi-pass rolling was implemented for cylindrical holes in strips of a low carbon steel. The reported results [24, 101] are mainly related to a multiple rolling processes that may not represent the principal step in the evolution of the surface defects, that being the first reduction.

The analysis of the micrographs in the transversal cross-section shows that cavities with the same initial width and increasing initial depth resulted in narrower final defects (Figure 4.4d-f). This is because deeper cavity sides are subjected to more buckling, as a result of this, the defect width is reduced. This phenomenon is presented in Figure 7.1 where the initial and final outlines of two cavities (B2 and B3) are compared, dashed and solid lines represents the initial and final transversal configuration respectively. The cavities were both machined to have an identical width, but B3 (Figure 7.1b) was 40% deeper than B2 (Figure 7.1c).

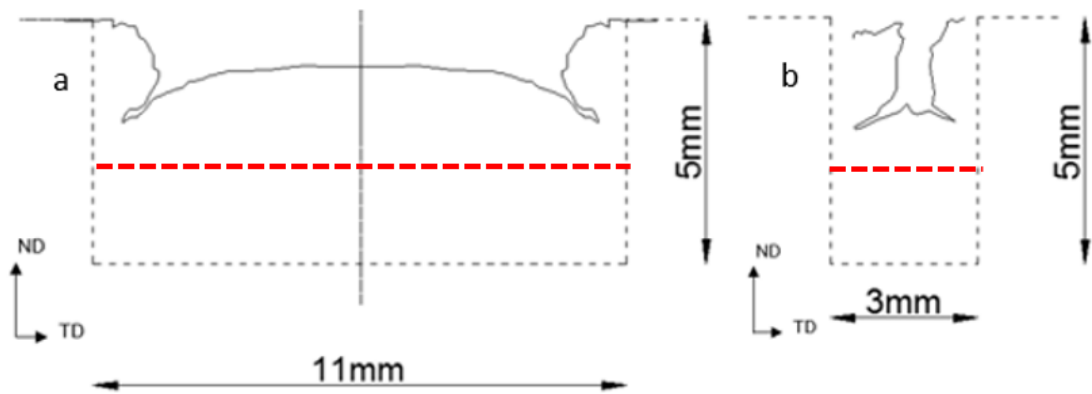
It is noticeable that the greater the depth to width ratio ( $D/W$ ) reduces the flow of the material from the bottom of the cavity upward the middle of the cavity (Figure 7.1b) forming a narrow final defect. Conversely, for a smaller  $D/W$  ratio, the material has more space available to spread towards the middle of the cavity

resulting in a more open final configuration (Figure 7.1a). Despite the reduced lateral spread of material for cavities with smaller initial depth, more deflection of the lateral is presented favouring the oxide detachment and removal from the side.



**Figure 7.1: Transversal sections of the defects (a) B2 and (b) B3 showing effect of the initial depth on the evolution mechanism. The black dashed line represents the initial cavity shape, the solid line is the final shape after rolling.**

In the case of a constant initial depth, a smaller depth to width aspect ratio results in shallower final defect (Figure 7.2). This is because the material at the middle section of the cavity base is less restricted by the side walls in a wider cavity (Figure 7.2a) resulting in a greater bulging effect of the bottom, and, as a consequence, a shallower final depth. This dependence is shown in Figure 4.8 where the changes in the measured final depth for the given initial depth is presented against the D/W ratio.

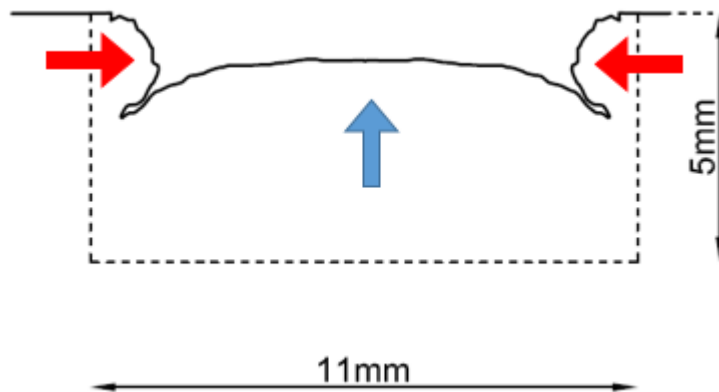


**Figure 7.2: Transversal section of the defects D3 (a), and B3 (b). The black dashed line represents the initial defect shape, the continuous line represents the final defect section after the rolling and the red dashed lines represent the theoretical 40% thickness reduction.**

Another important finding is that all the defects were reduced more than 50% in depth, in spite that the thickness reduction applied to the slab was only 40%. This is valid for both the measured depths parameters ( $D_f$  and  $D_{fc}$ ). This is shown in Figure 7.1 and Figure 7.2 where, the expected 40% reduction in depth of the defect is highlighted with red dashed lines. The reason for the more pronounced depth reduction of the defects in the shallower point ( $D_f$ ) is the bulging of the material from the bottom of the defect. The more pronounced depth reduction measured in the crevices ( $D_{fc}$ ) is related the transversal spreading of the material due to the buckling of the lateral sides of the defect. In fact, considering the high poisson ratio of about 0.4 of the material, the transversal elongation due to the spreading of the material is partially converted in a vertical contraction of the material near to the defect which reduces its depth.

The analysis of the area reduction in Figure 4.9 showed that deeper and wider cavities show the largest area reduction after deformation. This is due to the buckling of the side walls and the spreading of the material from the bottom towards the middle of the cavities. This happens because, during the compression, the material releases the accumulated stress by spreading or bulging towards the cavity. These effects are presented in Figure 7.3, where the

buckling of the lateral sides and the spreading from the bottom of the defect are indicated with red and blue arrows respectively.



**Figure 7.3: Buckling effect of the lateral sides (red arrows), and spreading effect of the material from the bottom of the defect (blue arrow). The continuous and the dashed lines represent the defect before and after rolling respectively.**

In addition, the comparison of the slopes of the trend lines representing the reduction in cross-sectional area against initial depth (Figure 4.9a) and initial width (Figure 4.9b) shows that an increase of the initial depth has a more pronounced effect in terms of percentage reduction of cross-sectional area than an increase of the initial width. This suggests that the buckling of the lateral sides has a more important effect on the reduction in cross-sectional area than the material bulging from the bottom of the cavity. In fact, the buckling of the lateral sides of the defects is a direct consequence of the compression applied by the roll during rolling, while the spreading of the material from the bottom of the cavity is an indirect response of the material to the compression which generates a material flow within the cavity.

The analysis conducted by measuring the buckling effect (Figure 4.7) and the percentage of area reduction (Figure 4.10) of the defects for different D/W aspect ratio show similar results. In fact, in both cases, higher D/W aspect ratio of the initial cavities resulted in higher values of buckling and area reduction value. Similar findings are also reported in the literature [101]. It seems that the

aspect ratio has a more pronounced effect in wider initial cavities, this is shown in Figure 4.7 by comparing the higher slope of the trend lines for wider initial defects. This effect is analogous to the one observed in Figure 4.10 where the percentage of area reduction is presented. This is a further confirmation of the strong dependency between area reduction and buckling of lateral sides of the defect.

### **Empirical model prediction of the final defects dimension**

A second order polynomial regression equation, as expressed in Ref [102], with three predictor variables (initial width, depth, and length) was used to correlate the initial cavity geometry to the final configuration. The calibrated equation can then be used to predict the final defect characteristics in function of the initial dimension. Equation 7.1 shows the general form of the proposed model wherein  $W_i$ ,  $D_i$  and  $L_i$  represent the initial width, depth and length, respectively.

#### **Equation 7.1**

$$Y = \beta_0 + \beta_1 \cdot W_i + \beta_2 \cdot D_i + \beta_3 \cdot L_i + \beta_4 \cdot W_i^2 + \beta_5 \cdot D_i^2 + \beta_6 \cdot L_i^2 + \beta_7 \cdot W_i \cdot D_i + \beta_8 \cdot W_i \cdot L_i + \beta_9 \cdot L_i \cdot D_i$$

The dependent variable  $Y$  was used to represent the final width, depth or length of the defect after rolling at a given condition. The regression coefficient  $\beta_0$  shows the intercept of the surface described by the regression equation. The linear and quadratic contributions of each predictor variable are the coefficients  $\beta_1$ – $\beta_6$ . Additionally, the last three coefficients ( $\beta_7, \beta_8, \beta_9$ ) determine the expected change in  $Y$  due to the interaction between initial geometrical parameters  $W_i$ ,  $D_i$  and  $L_i$ .

Figure 7.4 shows the effect of initial dimensional variables of the cavities on the measured final length and compares this to the model prediction. According to the figure, the final length is almost independent of the initial width and depth of the defects and it is mostly influenced by the initial length of the defect. Equation 7.2-4 show the developed functions to predict the final length, width, and depth, respectively. According to the given variables and the generic polynomial of Equation 7.1. The regression coefficients  $\beta_i$  were replaced by the terms  $a$  –

$g, m$  and  $n, o$  and the subscripts  $W, D, L$  indicate whether the parameters were used to predict the final length, width or depth of the defects respectively. The regression coefficients  $a$  to  $o$  were calibrated using the least square method to minimize the error between the measured and predicted results for each data point.

**Equation 7.2**

$$L_f = a_L + b_L \cdot W_i + c_L \cdot D_i + d_L \cdot L_i + e_L \cdot W_i^2 + f_L \cdot D_i^2 + g_L \cdot L_i^2 + m_L \cdot W_i \cdot D_i + n_L \cdot W_i \cdot L_i + o_L \cdot L_i \cdot D_i$$

**Equation 7.3**

$$W_f = a_W + b_W \cdot W_i + c_W \cdot D_i + d_W \cdot L_i + e_W \cdot W_i^2 + f_W \cdot D_i^2 + g_W \cdot L_i^2 + m_W \cdot W_i \cdot D_i + n_W \cdot W_i \cdot L_i + o_W \cdot L_i \cdot D_i$$

**Equation 7.4**

$$D_f = a_D + b_D \cdot W_i + c_D \cdot D_i + d_D \cdot L_i + e_D \cdot W_i^2 + f_D \cdot D_i^2 + g_D \cdot L_i^2 + m_D \cdot W_i \cdot D_i + n_D \cdot W_i \cdot L_i + o_D \cdot L_i \cdot D_i$$

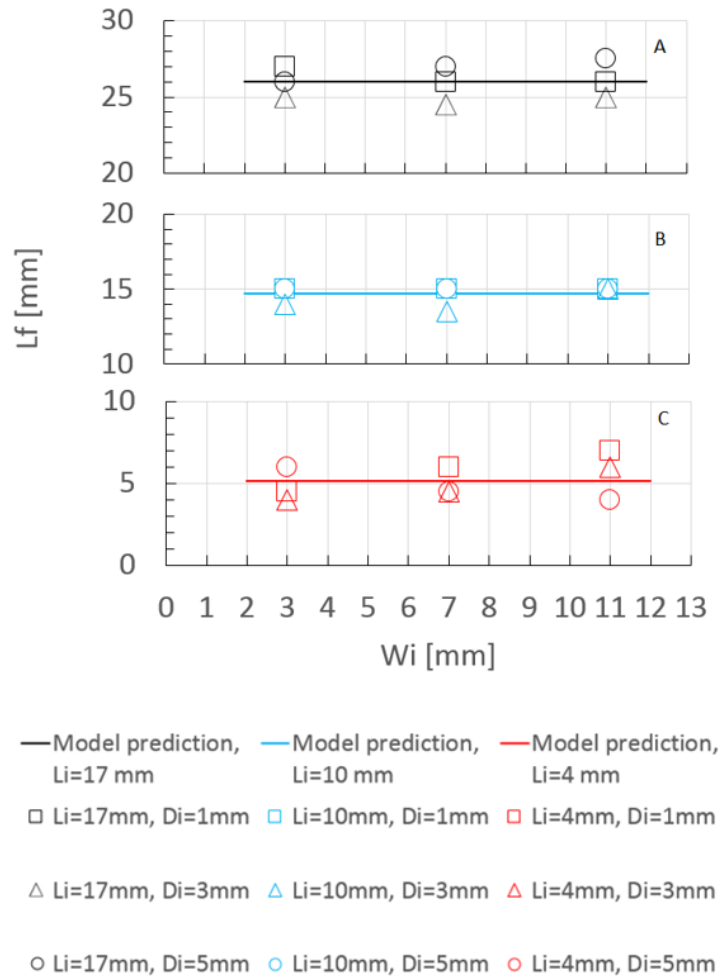
It was found that, for the prediction of the final length ( $L_f$ ), the coefficients associated with the initial depth and width of the cavities are several order of magnitude smaller than those related to  $L_i$  variable. This indicates that initial width and depth have a negligible effect on the final length of the cavities after deformation and this can be predicted using Equation 7.5:

**Equation 7.5**

$$L_f = a_L + d_L \cdot L_i + g_L \cdot L_i^2; \quad a_L = -1.1467; \quad d_L = 1.5726; \quad g_L = 0.0014$$

The solid lines in Figure 7.4 shows the predicted curves for the final length of defects with different initial width and depth values.





**Figure 7.4: Experimental measurement and prediction of the final length for defects with different initial depths and widths.**

A similar procedure was used to obtain the required functions to predict final width and depth values of the cavities. A least-square technique was applied to determine the regression coefficients and those with a negligible effect were excluded from the respective equations. The calibration process showed that the effect of the initial length on the evolution of the cavities can be ignored for the transverse (width) and normal (depth) directions. According to the least-square fitting results, the interactive summation terms (associated with  $m$ ,  $n$ , and  $o$ ) were found to be negligible compared with the other coefficients for the  $W_f$  function (Equation 7.6). It was also found that the quadratic terms have negligible effect in the prediction function for  $D_f$ . Consequently, a linear

function was obtained simply with different slopes depending on the initial depth of the defects (Equation 7.7).

**Equation 7.6**

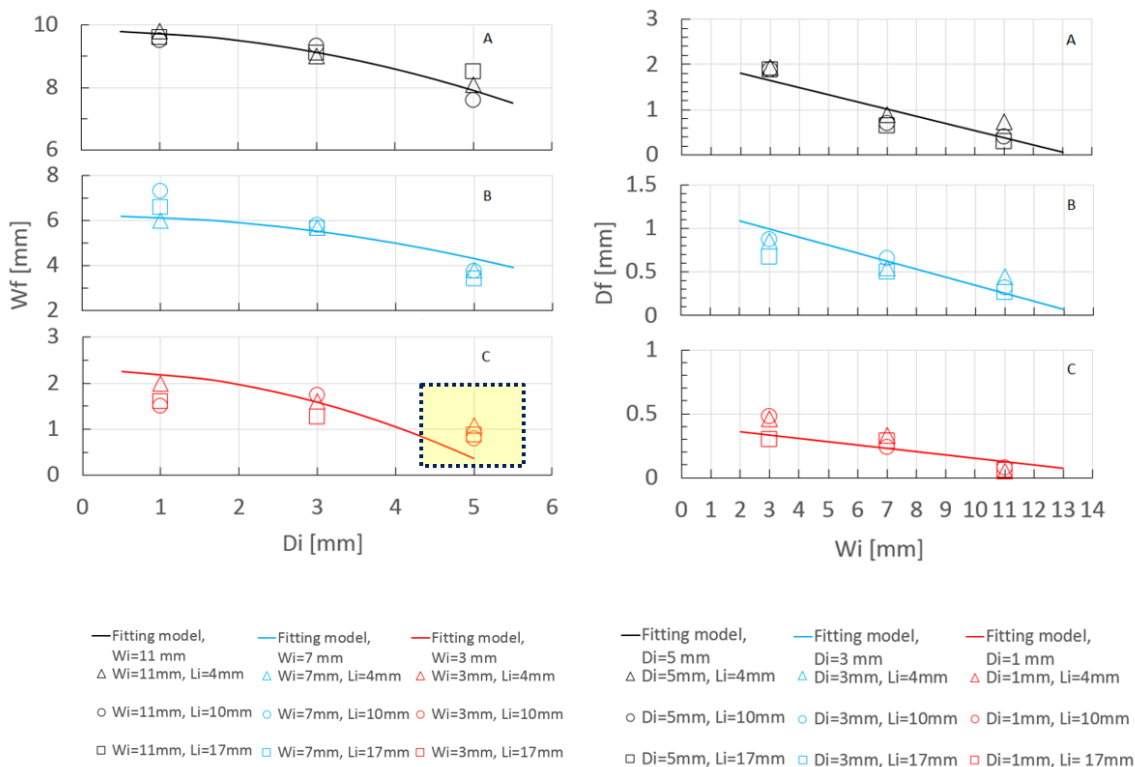
$$W_f = a_W + b_W \cdot W_i + e_W \cdot W_i^2 + f_W \cdot D_i^2 ;$$

$$a_W = -0.9334; \quad b_W = 1.1103; \quad e_W = -0.0761; \quad f_W = -0.0116$$

**Equation 7.7**

$$D_f = a_D + b_D \cdot W_i + c_D \cdot D_i + m_D \cdot W_i \cdot D_i = (a_D + c_D \cdot D_i) + (b_D + m_D \cdot D_i) \cdot W_i$$

$$a_D = -0.0204; \quad b_D = 0.4303; \quad c_D = 0.0075; \quad m_D = 0.0333$$



**Figure 7.5: Left) final width prediction, for different initial depths and lengths, Right) final depth prediction, for different initial widths and lengths.**

Figure 7.5 shows the effect of initial dimensional variables of the cavities on the measured final width (Figure 7.5-left) and final depth (Figure 7.5-right) and compares this to the model prediction. Overall, a good match is obtained between the model and the experimental values. However, the model is under-predicting the final width for short and deep cavities as it is highlighted in yellow in Figure 7.5c-left). This difference can be explained by the presence of oxide inside the cavities, visible in Figure 4.5. Taking in consideration the fact that the cavity is very narrow compared to the others (3mm), the oxide may have prevented the defect to be further reduced in width during the rolling. Considering the good match encountered, equations can be used to predict final defect dimension of known initial cavities dimensions.

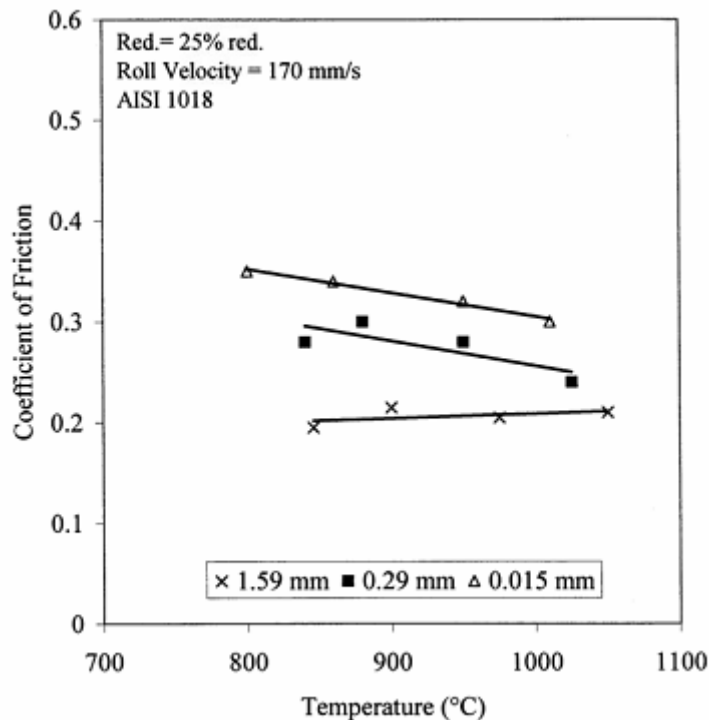
### **7.1.2 Slab distortion dependence on oxide thickness**

Oxide thickness was found to play an important role in the pin distortion during rolling. More distortion was present for thinner oxide layers as noticeable in Figure 4.14, this suggests that friction decrease with the oxide layer thickness. This outcome is in agreement with the research carried out by Munther & Lenard [50] and by Hara [75].

It is important to bear in mind that slabs with different oxide scale thickness were rolled at different temperatures (1100°C, 1050°C and 1000°C) so the effect of the temperature on friction was not separated from the effect of the oxide scale thickness. For this reason, it could be argued that the temperature could have played a role in the different deformation patterns because of the different mechanical resistance of the slabs subjected at different temperatures. However, this hypothesis is excluded because the slabs rolled at a higher temperature (*e.g.* 1100°C) showed lower pins distortion compared to the slabs rolled at lower temperatures (*e.g.* 1000°C) as shown in Figure 4.14. This proved that the effect of different frictions due to different oxide thickness present on the surface overcomes the effect of the different mechanical properties. In fact, for a given friction coefficient, slabs rolled at higher temperature should have

resulted in higher pin deformation distortion because of the lower mechanical properties.

Different test temperature could have affected the friction coefficient slightly, but, considering the large difference in oxide thicknesses tested (40  $\mu\text{m}$ , 230  $\mu\text{m}$  and 450  $\mu\text{m}$ ) and the reduced difference of about 50°C between the different thermal conditions tested, the effect of different temperature on friction is assumed to be negligible with respect to the effect of different oxide thickness applied. To justify this assumption, a graph presenting the effect of different temperatures and different oxide thicknesses on the friction coefficient is presented in Figure 7.6. The results are based on the experiments carried out by Lenard and Munther [50] on a mild/low carbon steel (AISI 1018). As noticeable from the graph, the friction coefficient is more sensitive to a variation of about 200  $\mu\text{m}$  in oxide thickness compared to a temperature variation of 50°C.

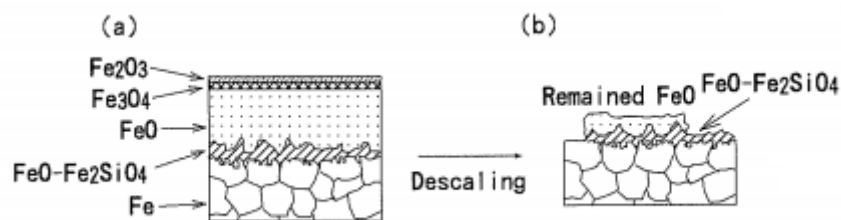


**Figure 7.6: Friction coefficient dependence on temperature and oxide scale thickness [50].**

Concluding, if temperature played a role in the friction coefficient during the experiment, it is realistic to assume that its effect is negligible compared with the effect of different oxide thickness for the ranges of temperature considered.

### 7.1.3 Oxide scale characterization after descaling

The oxide scales were not completely removed after the descaling. The slabs of silicon steel presented a final thickness of about 15  $\mu\text{m}$ . The poor descaling of silicon steels has been explained by different authors [10, 94, 103, 104]; the water spray impact effect is reduced by the existence of a eutectic compound  $\text{FeO-Fe}_2\text{SiO}_4$  in the scale/steel interface. This compound is much harder than the  $\text{FeO}$  scale, and it works as an anchor between the thick oxide layer consisting mainly of wüstite ( $\text{FeO}$ ) formed during the heating and the steel substrate (Figure 7.7a).



**Figure 7.7: Mechanism of scale formation and descaling in Si steel, before (a) and after (b) descaling [94].**

The water spray impact is effective in breaking the wüstite ( $\text{FeO}$ ), ferrite ( $\text{Fe}_2\text{O}_3$ ) and magnetite ( $\text{Fe}_3\text{O}_4$ ) oxides from the surface, but residual of wüstite can remain attached along with the fayalite ( $\text{Fe}_2\text{SiO}_4$ ) in the surface as observable in the general scheme in Figure 7.7b and in the micrographs of Figure 4.16.

With regards to the effectiveness of the descaling in holes of different aspect ratio, it is worth to notice that horizontal bottom surfaces of the cavities were better descaled than the vertical sides of the same cavities (Figure 4.17). This result might be explained by the fact that descalers standoff angles are set up to guarantee an optimum descaling of horizontal surfaces; the same angle may not be effective when the spray is applied on vertical surfaces (as the vertical sides of the defects).

The descaling is less effective in the cleaning of deeper cavities, in fact, holes with a depth of 2mm presented a better descaling than the deeper holes. This complicates the defect evolution and generation phenomena as deeper defects have a higher tendency to generate longer folding crevices (as shown in chapter 4.3) between the lateral sides and the bottom surfaces. Therefore, having more oxide available, deeper defects are likely to bury very large amounts of oxide during the deformation.

It is interesting to note that the bottom of the shallower cavities shows more consumption of the internal corner after heating and descaling compared with the deeper ones (Figure 4.17). A possible explanation may be the reduced oxygen content in the bottom of the deeper defect which has reduced the growth rate of the oxide thickness compared with the shallower defects.

#### **7.1.4 Temperature dependence of friction**

The analysis of the samples on Figure 4.21 demonstrated that rings compressed at similar thickness reduction ratio show different final diameters for different test temperature conditions (for example comparing rings a and b with rings e and f). As the deformation of the ring is strictly related with the friction coefficient, this observation may support the hypothesis of temperature dependence of friction. Most of the rings showed a relatively regular final circular shape, this may be an index of homogenous friction in the contact between tools and rings. In addition, the horizontal symmetry of the rings (Figure 4.20b) encountered suggests that the friction was similar for both the top and bottom surface. A stable value of friction between the surfaces and a similar value for both the surfaces are essential to obtain a reliable friction coefficient measurement.

According to with the Sofuoglu's suggestions [105], specific calibration curves taking into account the material type and the test condition were obtained. Calibration curves for the specific test conditions and material type used were produced by means of the FE model reported in 5.8.

It is worth to notice that the sensitivity of the ring internal diameter change to friction is reduced for higher friction values (Figure 5.28). This is because, for higher friction coefficients, the frictional forces approach the shear limit resistance of the material, when this happens, further increase of friction coefficient became negligible. Thereafter, it means that for higher friction values, fewer differences in ring deformation are noticeable, and more difficult and less reliable friction coefficients values will be determined.

Some experimental points were far from the average, those measurements (evidenced in yellow in Figure 5.31) coincide with some of the rings that remain attached at the tools after the compression. The sticking of the rings on the tools is expected to have affected the deformation, resulting in higher friction coefficient measurements.

Generally, the friction coefficient was found to increase with temperature. Previous studies evaluating friction in function of temperature report contradictory results. On one hand, Roberts [62, 106], Pawelski [107] and Underwood [108] studies reported that friction increases with temperature. On the other hand, Wusatowski [109] and Rowe [110] reported empirical equations suggesting that friction decreases with the temperature. Lenard [63], suggested that since the tests were carried out on different materials, a possible explanation of the contradictory results may be the difference in the chemistry of the material considered. For this reason, the only way to verify the reliability of this outcome is comparing the results of previous studies carried out on similar silicon steel alloys.

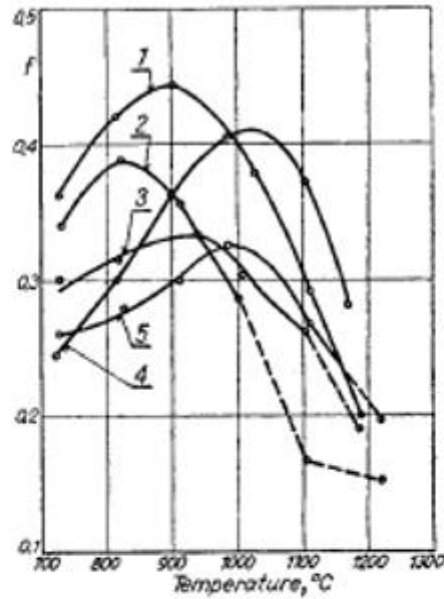
The only study which reports information about the frictional state at different temperatures for electrical steels the Hara's research [75]. In the experiment, the distortion of pins inserted in the slab was compared for slabs rolled at two different temperature: above (1473 °K) and below (1373 °K) the eutectic transformation of the compound  $\text{FeO}/\text{Fe}_2\text{SiO}_4$  which is 1450 °K. Lower distortion of the pins was observed for the higher temperature. For this reason, friction was assumed to decrease with temperature.

This behaviour was due to the liquid lower scale which flows freely and it is squeezed out to the contact with the mill, this liquid is supposed to reduce the friction. However, the explanation given by Hara is limited to the liquid to solid transition of the subscale for high temperatures close to the eutectic transformation temperature of the FeO/Fe<sub>2</sub>SiO<sub>4</sub> compound. For this reason, these findings cannot be extended to lower ranges of temperatures as the temperatures of the ring test carried out.

Integrating the results obtained from the Isothermal ring tests carried out with the results presented by Hara, the outcome is that friction increases with temperature until the eutectic temperature of the wustite/fayalite is reached. Above this temperature, the liquid lower scale acts as a lubricant during the contact, and friction decreases with temperature.

An extensive research carried out by Pavlov and Kuprin [111] where different alloys were analysed during rolling at different temperatures was reported in Wusatowski's book [109]. The Figure 7.8 clearly shows that friction increases with temperature until a certain value of temperature is reached. A change of trend is noticeable for higher values of temperature.





Steel grade	Composition, %							
	C	Mn	Si	S	P	Ni	Cr	Cu
30HGSA	0.21	0.96	1.12	0.028	0.013	8.50	—	—
H18N9	0.12	0.85	0.37	0.012	0.018	8.50	17.98	—
EJ94	0.79	13.8	0.65	0.025	0.03	3.20	0.20	—
St10	0.12	0.43	0.27	0.032	0.016	0.13	0.12	—
St20	0.17	0.40	0.35	0.040	0.014	0.12	0.10	0.20
St40	0.43	0.67	0.33	0.027	0.020	0.16	0.14	0.20
A12	0.12	0.69	0.24	0.184	0.018	—	—	—
A20	0.21	0.65	0.21	0.154	0.016	—	—	—
A40	0.43	1.32	0.29	0.246	0.026	—	—	—

**Figure 7.8: Variation of friction coefficient with temperature for different steels, and chemical analysis of the tested steels: St20 (1), A20 (2), 30HGSA (3), H18N9 (4), EJ94 (5) [64].**

Lenard experiments on the effect of temperature on friction coefficients [63] reported analogous results. In particular, it was reported that increasing temperature first cause increasing of frictional forces until a maximum value is reached followed by a significant drop. Possible explanations of this behaviour were not reported in the literature. However, adhesion or sticking between rings and tools may have been facilitated when oxide gets softer as the temperature increase resulting in higher friction coefficients. This is valid until the subscale became liquid; above the transition temperature, the liquid acting as a lubricant reduces the friction coefficient drastically.

A note of caution is due here since the test were carried out isothermally. Certainly, the isothermal condition of the test is not reproducing the real contact condition between roll and slab during the rolling. The non-isothermal test is usually not recommended when the heat transfer behaviour of the process is not well known [89]. In fact, when there is a great gradient of temperature between the sample and the environment, the heat transfer greatly affects the deformation of the rings. Therefore, it is not possible to obtain accurate calibration curves unless the heat transfer between ring and tools is well modelled. As the HTC is strictly dependent on the oxide thickness which is not a stable value, the non-isothermal ring tests were avoided in this research.

However, even if the test were carried out isothermally, the experiment provided an interesting dependence of the friction on the temperature of the oxide scale present between the parts in contact. The results of the ring test experiments will be implemented in the frictional model of the process as it is assumed to be more realistic than a constant friction coefficient.

## **7.2 Numerical discussions**

The multilevel approach was successfully applied and the quality check showed positive results. In fact, the presence of the defect in the mesoscale model is not altering the stress field nor the temperature field at the boundaries as presented in Figure 5.12. A difference of about 30% of the stress field is observed in the slab corner as highlighted in yellow in Figure 5.12. However, this difference was due to the mesh dependence and cannot be avoided as mesh transition is needed in the model. Additionally, the distortion is far from the defect, for this reason, it is not considered to be critical. The comparison of the stress and temperature fields in the other boundary surfaces is good.

The macroscale model was calibrated varying the friction coefficient in order to minimise the difference in the strain pattern between the model and the pin distortion measured.

A friction coefficient of 0.25 was obtained from the calibration and the model was used to estimate the roll force present during rolling. The comparison

between the roll force measurements and roll force prediction shows a good match with an error of 5% in the steady state. This is because the heat transfer coefficient adopted for the simulations is pertinent to industrial standard hot rolling processes where thinner oxide layers are present due to the more effective descaling procedure used (high-pressure water spray). On the contrary, in the experimental procedure carried out, the oxide was removed by a scraper resulting in inhomogeneous and thicker layers. Since oxide layers behave as a thermal barrier [52, 112], the thicker scales could have slightly reduced the heat transfer during the process slowing down the cooling of the slab resulting in softer material and consequent lower roll forces. A higher error of the roll force prediction is present at the first contact due to the strain rate sensitivity of the material model. The high velocity imposed to the slab to initiate the rolling bite of the slab resulted in the strengthening of the material in the contact point. This difference is not considered critical as it is only present during the initial rolling transition state.

The validation of the mesoscale model was carried out by comparing the predicted and measured final configurations of 5 cavities selected to cover specific aspect ratios and dimensions.

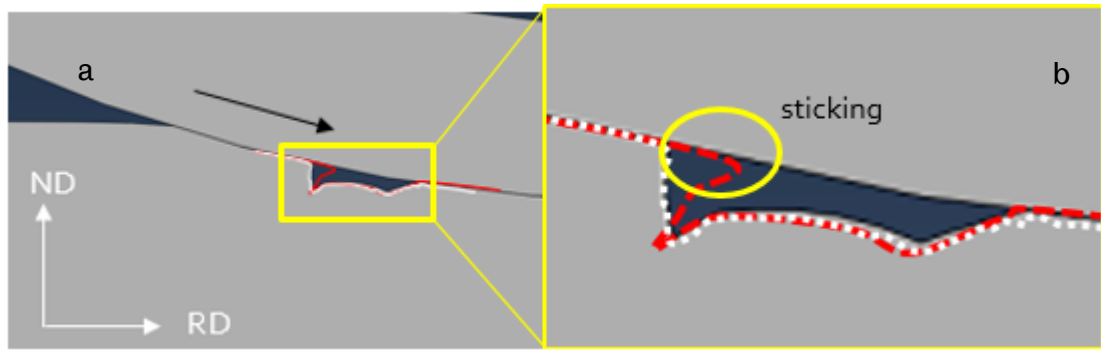
The average errors of the prediction encountered is 12.9%, 12.3% and 15.3% for the length width and depth respectively. Length and width are slightly overpredicted in general, this is due to the fact that the model is generally underpredicting the buckling of the lateral sides. In fact, the buckling of the lateral sides and relative transversal spreading of material is identified to be the main cause of defect width reduction during rolling.

A possible explanation of this phenomena may be the fact that the Coulomb friction model used to define the contact was probably excessively simple to simulate such a complex contact condition. In fact, anisotropic friction behaviours could have played a role during the experiment resulting in lower elongation and higher narrowing of the defect in the longitudinal and transversal section respectively. In addition, sticking between roll and slab could have occurred where discontinuities of oxide were present increasing the buckling of

the lateral sides. Moreover, the material consumption of the initial surface of defects due to the oxidation of their surfaces could have also played a role, resulting in different initial cavity geometries before the rolling which was not considered during the modelling. It must also be said that a finer mesh would have resulted in a slightly more pronounced buckling of the lateral sides as shown on 5.7.1.

For what concerns to the deformation mechanisms observed, it is worth to notice that a crevice forming phenomenon was observed in both transversal and longitudinal sections of the defects due to the buckling of the vertical sides of the cavities during rolling. Similar mechanisms were experienced during the defect behaviour experiment carried out; more details and further explanations regarding the defect behaviour mechanisms are presented in chapter 4.

In general, the transversal section deformation behaviour is better simulated by the model. A possible explanation is that the effect of possible sticking phenomena manifested during the experiment between slab and roll when discontinuities of oxide are present (which are not taken into account in the contact model) may have a more pronounced effect in creating a longer crevice in the longitudinal direction due to the rotation of the roll and the absence of slipping with the slab. The result of this theoretical sticking between slab and roll is schematically presented in Figure 7.9 where a longitudinal section of a defect during the deformation is presented. As shown in the figure, if slipping is not permitted, the end of the defect may be constrained to deform remaining attached at the roll Figure 7.9b. The result could be a more critical crevice formed as indicated in red. This may be less critical in the transversal direction, because the effect of possible sticking between slab and roll may only increase slightly the buckling of the lateral side walls of the cavity.



**Figure 7.9: Theoretical effect of sticking between the roll and back side of the defect. White pointed line present the case where no sticking is present, the red line present the hypothetical case where sticking between slab and roll is present the longitudinal back end of the cavity.**

The model produced can be used as a tool to predict the mechanisms of defect evolution of different defect geometries and dimensions. In addition, the model can be used to carry out a sensitivity analysis of the final defect severity to different process parameters (as friction, temperature, velocity, material properties, reduction ratios etc.). The understanding of the defect evolution mechanisms and the sensitivity of process parameters can be useful in the industry to prevent or reduce the defect formation.

The friction coefficient is found to affect the defect evolution during rolling. In particular, higher friction coefficients reduced the slipping between the top surface of the slab and the roll increasing the barrelling of the lateral sides of the roll and the bulging of the bottom surface of the defect. A similar effect was also observed by Naizabekov [47], in his study, defects were found to be more reduced in depth as the friction coefficient increases. A possible explanation may be the fact that lower slipping of the contact surface of the slab forces the material to flow within the cavity (through more bucking of the lateral sides and more bulging of the bottom surface) as a result of the vertical deformation imposed by the rolling.

One interesting finding is the defect evolution when the temperature dependent friction coefficient was used. The cavity present in the slab rolled with a temperature dependent friction coefficient seem to behave as a cavity subjected

to a constant friction coefficient ranging between 0.2 and 0.3. This is noticeable in Figure 6.3 comparing the pointed line (representing the defect final transversal section) and the coloured lines (representing defects subjected to different friction coefficients). This is because as friction decreases with temperature (according to the temperature-dependent friction model used), the cooling of the slab may have lowered the friction coefficient substantially.

Figure 6.4 shows the effect of different reduction ratio on the defect evolution, large differences between the cases studied were found. As expected, higher reduction ratio resulted in more deformation. Consequently, more buckling of the lateral sides, bulging of the bottom surface, and longer crevices are formed for higher thickness reduction ratios. The figure suggests that the buckling of the lateral sides of the defect is initiated for all the three reduction cases. Therefore, further thickness reduction applied by the successive rolling stand are expected to increase the severity anyway.

Figure 6.5 presents the effect of different initial temperatures of the slab on the defect evolution during rolling. It is worth to notice the negligible effect of the temperature on the final defect shape. This is due to the reduced ranges of the temperatures applied. Temperatures lower than 1000°C were avoided because they can lead to very high roll forces, and higher temperature was avoided because they are not suitable for electrical steel production.

The most interesting finding is the effect of the geometry on the defect evolution. In particular, spherical cavities were found to be easier flattened during rolling. In fact, they are less inclined to form crevices due to the dome shape resistance to deformation, the elongation imposed leaves space for the bottom of the cavity to spread vertically and reduce the depth as shown on Figure 6.6-B2, the result is a full opening and flattening of the defect. The pyramidal cavities are opened in the rolling direction and reduced in depth, however, the apex of the pyramid can be critical for pyramids with a high depth to width aspect ratio. This is because barrelling of the lateral sides is facilitated when their slope is closer to the vertical. When this happens, crevice may form and oxide can be trapped irreversibly as a result of the closing of the apex of the

pyramid as highlighted in yellow in the longitudinal section presented in Figure 6.6-C2 and in the transversal section presented in Figure 6.8-C. Pyramidal defects with a depth to width aspect ratio lower than 0.5 are found to be easily flattened during the rolling, and critical crevices start forming for depth to width aspect ratios higher than 1.

The cubical cavity was confirmed to be the most critical geometrical shape, in fact, compared with the other geometries, in cubical cavities crevices are easily formed due to the folding of the lateral sides with the bottom surfaces of the defects due to the buckling. As expected, crevices were formed longitudinally and transversally. Further discussion on the behaviour of cubical defects is discussed in (chapter 4).

The most relevant outcome observed was found during the analysis of the effect of different fillet radius on the final defect severity presented in Figure 6.10. The effect of the filling of the corners on the defect deformation is found beneficial. The amount of material in the corners and the circular shape, acting as a retaining wall reduces the buckling of the lateral sides and prevents the crevice formation in the corners. This effect is more evident for higher fillet radius.

Contrarily to the expectations, dimensional parameters of the initial cavities including depth, length and width were found less important than the initial geometrical shape and aspect ratios. In fact, the initial geometry is the parameter which mostly determines the deformation mechanism of the cavity. Once the mechanism of deformation is activated, the aspect ratio plays a role in reducing or increasing the severity of the final defect.

## 8 CONCLUSIONS AND FUTURE WORK

The designed experimental methodology proposed where three control parameters (D, L and W) are used to describe the defect evolution during rolling provided a better insight into the cavity evolution mechanisms present during rolling compared with the previous research studies where only cylindrical cavities with two control parameters were used [37]. The results obtained showed that the key geometrical parameters of the initial cavities that predominantly determine the final defect dimension and severity are the initial width and depth. In particular, the interaction between the bottom surface and the cavity lateral sides of the initial features plays a key role, with wider initial cavities forming shallower final defects, and deeper initial cavities forming narrower final defects. The buckling of the lateral sides of the cavities was identified to be the root cause of oxide scale entrapments within the cavity and this effect was found to increase with the initial cavity depth. Deeper initial cavities result in a more pronounced buckling whereas those initially with a depth of up to 1 mm were essentially eliminated.

The rolling experiment was also useful to identify the effect of different oxide thickness on the frictional behaviour. Particularly, it was found that friction decreases along with the oxide thickness. However, the effect of oxide thickness was not completely separated from the effect of temperature, to avoid this issue is recommended to evaluate the effect of oxide thickness on friction by means of isothermal ring compression tests on rings having different oxide thicknesses.

Isothermal ring compression tests were found effective in determining the effect of temperature on friction for a fixed oxide thickness of about 15  $\mu\text{m}$ . However, further research and additional tests are needed to verify the dependence encountered. This value was determined through a specific descaling experiment whose set-up was defined according to a specific industrial hot rolling process. The results show a clear relation between friction and temperature, in particular, friction increase with temperature.



The results of the hot rolling experiments were successfully employed to calibrate and validate a model reproducing the lab mill rolling process.

Similarly, the stress-strain curves of a Gleeble compression test carried out at different temperatures and strain rates were successfully used to calibrate a material model where stress levels are defined in function of temperature and strain rates. The Sellars and Tegart model used was found very effective for the higher values of strain rate and temperatures. The contact frictional conditions of the model were calibrated with a reverse procedure where the distortion pin displacement patterns were used as a reference. The friction coefficient was varied during the simulations to match the longitudinal distortion patterns. A constant friction coefficient of 0.25 was determined from the calibration. A multilevel approach was then applied to reproduce the evolution of different surface cavities under hot rolling; the mesoscale models obtained were successfully validated through comparison between the predicted and measured dimension of the final defects. The errors in the predictions were found to be of 12%. Differences may be due to the excessive simplicity of the friction model used to simulate the thermal and frictional effect of the oxide scale that separates the mill and the slab during the contact.

The calibrated material model and contact conditions were used to produce a full-scale hot rolling process. The model was then used to test the effect of different geometries and process parameters on the final defect conformation and severity. The study shows that while spherical cavities are easily flattened and opened during rolling, cuboidal and pyramidal cavities can generate critical crevices that depend on the initial aspect ratio. In pyramidal defects, crevices are present for depth to width aspect ratios higher than 2. With regards to the cubical defects, a parametric study involving cavities with different fillet radius corners was carried out. The results show that the fillet of the angles between the bottom surface and lateral surfaces can greatly affect the defect severity, in fact, the buckling of the lateral sides associated with the defect generation is prevented for a larger radius.

Concluding, what makes an initial feature critical is primarily the initial geometry and the sharpness of the corners. Then, for a given shape, deeper and narrower initial shapes are more likely to generate crevices resulting in more critical final defects. For given cavities, sensitivities studies show that friction is the main parameter affecting the defect severity during rolling. Higher friction coefficients result in shallower final defect and more buckling of the lateral sides.

Although the model produced positive results, it requires some improvements. To obtain more precise predictions of the defect behaviour, more complex frictional models taking into account possible sticking phenomenon and anisotropic friction values, are needed. In addition, further research focusing on the modelling of the oxide scale inside cavities of different aspect ratios could be very effective in fully describing the subsurface defect formation phenomenon typical of laps and slivers.

The model produced only involves the first rolling stand of a generic hot rolling process which remains the most important as this is where the first deformation of the defect occurs. However, the same approach can be applied in series, to reproduce a multi pass hot rolling process, including multiple rolling stands. This approach could be effective in describing the defect evolution through all the rolling stands. It would be then desirable to find the range of process parameters that would lead to the defect flattening, and the dangerous range of parameters not leading to the defect closure.

## 9 REFERENCES

- [1] S. Celotto *et al.*, "Lamination Surface Defects in Grain Oriented Electrical Steel," *Tata Steel internal report*, vol. 31, no. 0, 2014.
- [2] W. Sun, "A study on the characteristics of oxide scale in hot rolling of steel," pp. 228-228, 2005.
- [3] Y. Houbaert and U. Gent, "Hot Rolling of High-Silicon Steel : Scale Growth and its Plastic Deformation."
- [4] L. Suarez, J. Schneider, and Y. Houbaert, "High-Temperature Oxidation of Fe- Si Alloys in the Temperature Range 900-1250 ° C Supported by The British Library - " The world ' s knowledge " Supplied by The British Library - " The world ' s knowledge ", vol. 276, 2008.
- [5] T. Onishi, S. Nakakubo, and M. Takeda, "Calculations of Internal Oxidation Rate Equations and Boundary Conditions between Internal and External Oxidation in Silicon Containing Steels," vol. 51, no. 3, pp. 482-487, 2010.
- [6] F. Wang, L. Ning, Q. Zhu, J. Lin, and T. A. Dean, "An investigation of descaling spray on microstructural evolution in hot rolling," pp. 38-47, 2008.
- [7] N. Jin, S. Zhou, and T. S. Chang, "Identification of impacting factors of surface defects in hot rolling processes using multi-level regression analysis," *Transactions of the North American Manufacturing Research Institute of SME*, vol. 32, no. 2, pp. 557-564, 2004.
- [8] M. Takeda, T. Onishi, S. Nakakubo, and S. Fujimoto, "Physical Properties of Iron-Oxide Scales on Si-Containing Steels at High Temperature," vol. 50, no. 9, pp. 2242-2246, 2009.
- [9] R. Y. Chen and W. Y. D. Yuen, "Oxide-Scale Structures Formed on Commercial Hot-Rolled Steel Strip and Their Formation Mechanisms," vol. 56, no. 1, pp. 89-118, 2001.
- [10] L. Suárez, P. Rodríguez-calvillo, Y. Houbaert, and R. Colás, "Oxidation of ultra low carbon and silicon bearing steels," *Corrosion Science*, vol. 52, no. 6, pp. 2044-2049, 2010.
- [11] E. J. Song, D. W. Suh, and H. K. D. H. Bhadeshia, "Oxidation of silicon containing steel," vol. 39, no. 8, pp. 599-604, 2012.
- [12] "Influence of Temperature and Oxygen Content of Oxidation Atmosphere on Initial Oxidation of Si Containing Steels," vol. 99, no. 3, pp. 214-220, 2013.
- [13] Y. H. Li and C. M. Sellars, "Comparative investigations of interfacial heat transfer behaviour during hot forging and rolling of steel with oxide scale formation," vol. 81, pp. 282-286, 1998.
- [14] C. Grenier, P. O. Bouchard, P. Montmitonnet, and M. Picard, "Behaviour of oxide scales in hot steel strip rolling," *International Journal of Material Forming*, vol. 1, no. SUPPL. 1, pp. 1227-1230, 2008.

- [15] E. J. Song, D. W. Suh, and H. K. D. H. Bhadeshia, "Oxidation of silicon containing steel," *Ironmaking & Steelmaking*, vol. 39, no. 8, pp. 599-604, 2012.
- [16] M. Takeda, T. Onishi, S. Nakakubo, and S. Fujimoto, "Physical Properties of Iron-Oxide Scales on Si-Containing Steels at High Temperature," *Materials Transactions*, vol. 50, no. 9, pp. 2242-2246, 2009.
- [17] H. L. Yu, K. Tieu, C. Lu, G. Y. Deng, and X. H. Liu, "Occurrence of surface defects on strips during hot rolling process by FEM," *International Journal of Advanced Manufacturing Technology*, vol. 67, no. 5-8, pp. 1161-1170, 2013.
- [18] M. Atkinson, L. Kavanagh, D. McCutcheon, P. S. Cox, and R. Shultz, "Steel Industry Technology Roadmap," no. December, 2001.
- [19] X. M. P. C. Z. Hong and P. Zhu, "Research on Forming Reasons and Prevention Measures of Longitudinal Surface Cracks on Csp Thin Slab," *Gang Tie Fan Tai (Iron Steel Vanadium Titanium)*, vol. 25, no. 2, pp. 57-61, 2004.
- [20] C. Genzano, L. P. Reda, and J. Madias, "Minimization Of Surface Defects On Bars And Wire Rod Originated In Billet Casting," no. 1, pp. 386-395.
- [21] D. Zhou, J. Fu, D. Liu, Y. Kang, Z. Wang, and Y. Wang, "Forming mechanism and preventive measures of the surface crack in thin strip produced by CSP," *Journal of University of Science and Technology Beijing (China)*, vol. 24, no. 4, pp. 403-406, 2002.
- [22] Y. Z. Zhu, J. Rao, Z. Zhu, Z. D. Xiang, and Z. F. Wu, "Surface inclusions and their evolution on strip rolled on CSP line and in following cold rolling process," vol. 36, no. 7, 2009.
- [23] P. K. Tripathy, S. Das, M. K. Jha, J. B. Singh, A. M. Kumar, and A. K. Das, "Migration of slab defects during hot rolling," vol. 33, no. 6, pp. 477-483, 2006.
- [24] M. J. Merwin, "Evolution of Artificially Induced Slab Imperfections Through Hot and Cold Rolling," ed. Cleveland, Ohio: The Iron & Steel Technology Conference and Exposition, 2007, pp. 68-80.
- [25] S. Shainu *et al.*, "Study on Slab Surface Defects and Generation of FeO Type Slivers in Hot Rolled Coils," *Tata Steel Limited Jamshedpur*, 2008.
- [26] Shiro Kobayashi, Soo-Ik Oh, and T. Altan, "Metal Forming and the Finite-Element Method," ed: Oxford Series on Advanced Manufacturing, 1989.
- [27] M. Pietrzyk and J. Lenard "Thermal-Mechanical Modelling of the Flat Rolling Process," ed, 1991.
- [28] X. Shangwu, L. Xianghua, W. Guodong, P. A. F. Martins, J. Sihai, and Y. Jianguang, "Three-dimensional thermo-mechanical finite element simulation of the vertical–horizontal rolling process," *Journal of Materials Processing Technology*, vol. 110, no. 1, pp. 89-97, 2001.

- [29] X. Shangwu, J. M. C. Rodrigues, and P. A. F. Martins, "Three-dimensional modelling of the vertical – horizontal rolling process," vol. 39, pp. 1023-1037, 2003.
- [30] X. Shangwu, J. M. C. Rodrigues, and P. A. F. Martins, "Simulation of plane strain rolling through a combined finite element–boundary element approach," *Journal of Materials Processing Technology*, vol. 96, no. 1–3, pp. 173-181, 11/1/ 1999.
- [31] L. M. Galantucci and L. Tricarico, "Thermo-mechanical simulation of a rolling process with an FEM approach," *Journal of Materials Processing Technology*, vol. 92-93, pp. 494-501, 1999.
- [32] S. X. Zhou, "An integrated model for hot rolling of steel strips," vol. 134, pp. 338-351, 2003.
- [33] P. Montmitonnet, J. L. Chenot, C. Bertrand-Corsini, C. David, T. Lung, and P. Buessler, "A Coupled Thermomechanical Approach for Hot Rolling by a 3D Finite Element Method," *Journal of Engineering for Industry*, vol. 114, no. 3, pp. 336-344, 1992.
- [34] S. S. Ali, "Finite Element Analysis of Evolution of Defects During Rolling," vol. 2, no. 10, pp. 1937-1943, 2013.
- [35] M. E. Buldg, "INCLUSIONS IN CONTINUOUS CASTING OF STEEL," pp. 26-28, 2003.
- [36] A. Kainz, S. Ilie, E. Parteder, and K. Zeman, "From Slab Corner Cracks to Edge-Defects in Hot Rolled Strip – Experimental and Numerical Investigations," *Metal Forming*, no. finishing mill, pp. 861-867, 2008.
- [37] C. J. Lee S.-L, "Deformation analysis of surface defect on hot rolling by 3-D FEM simulation," *Revue de Metallurgie. Cahiers D'Informations Techniques*, vol. 105, no. 3, pp. 127-135+III-IV, 2008.
- [38] S. Moir and J. Preston, "Surface defects - evolution and behaviour from cast slab to coated strip," *Journal of Materials Processing Technology*, vol. 125, pp. 720-724, 2002.
- [39] I.-h. Son, J. Lee, Y.-h. Lee, D.-l. Lee, and Y.-t. Im, "FE simulations of deformation behavior with surface defects in wire rod rolling," vol. 10, no. 1, pp. 71-78, 2007.
- [40] B. G. Thomas, M. S. Jenkins, and R. B. Mahapatra, "Investigation of strand surface defects using mould instrumentation and modelling," vol. 31, no. 6, pp. 485-494, 2004.
- [41] G. R. Johnson and W. H. Cook, "A constitutive model and data for metals subjected to large strains, high strain rates and high temperatures," ed, 1983, pp. 541-547.
- [42] C. M. Sellars and W. J. McTegart, "On the mechanism of hot deformation," vol. 14, ed, 1966, pp. 1136-1138.

- [43] F. Garofalo, "An empirical relation defining the stress dependence of minimum creep rate in metals," *Trans.AIME*, vol. 227, pp. 351-356, 1963.
- [44] J. J. J. Uvira J.L, "Hot compression of Armco iron and silicon steel," *Transactions of the Metallurgical Society of AIME*, vol. 242, no. October 1967, pp. 1619-1926, 1968.
- [45] Y. U. Hai-liang, L. I. U. Xiang-hua, and W. Guo-dong, "Analysis of Crack Tip Stress of Transversal Crack on Slab Corner During Vertical-Horizontal Rolling Process by FEM," vol. 15, no. 3, pp. 19-26, 2008.
- [46] H.-I. Yu, X.-h. Liu, and X.-j. Ren, "Behaviour of Longitudinal Cracks on Slab Surfaces in V-H Rolling Processes," vol. 2, no. 7, pp. 537-544, 2008.
- [47] A. Naizabekov, V. Talmazan, and A. Yerzhanov, "Analysis Of Surface Defects Of " Dent " And " Pin - Hole " Types Formation Process During Cold Rolling," Brno, Czech Republic.
- [48] H.-I. Yu, X.-h. Liu, H.-y. Bi, and L.-q. Chen, "Deformation behavior of inclusions in stainless steel strips during multi-pass cold rolling," vol. 9, pp. 455-461, 2008.
- [49] H. Utsunomiya, S. Doi, K.-i. Hara, T. Sakai, and S. Yanagi, "CIRP Annals - Manufacturing Technology Deformation of oxide scale on steel surface during hot rolling," vol. 58, pp. 271-274, 2009.
- [50] P. A. Munther and J. G. Lenard, "The effect of scaling on interfacial friction in hot rolling of steels," vol. 88, pp. 105-113, 1999.
- [51] C. D. Roberts, "Mechanical principles of rolling," *Iron Steelmaker*, vol. 24, pp. 113-114, 1997.
- [52] M. Krzyzanowski, J. H. Beynon, and D. C. J. Farrugia, *Oxide Scale Behaviour in High Temperature Metal Processing*.
- [53] J. G. Lenard, "An Experimental Study of Boundary Conditions in Hot and Cold Flat Rolling," no. 1, pp. 279-282, 1990.
- [54] J. G. Lenard and L. Barbulovic-nad, "The Coefficient of Friction During Hot Rolling of Low Carbon Steel," vol. 124, no. October, pp. 840-845, 2002.
- [55] B. K. Chen, P. F. Thomson, and S. K. Choi, "Temperature distribution in the roll-gap during hot flat rolling," *Journal of Materials Processing Technology*, vol. 30, no. 1, pp. 115-130, 1992/02/01 1992.
- [56] S. L. Semiatin, E. W. Collings, V. E. Wood, and T. Altan, "Determination of the interface heat transfer coefficient for non-isothermal bulk-forming processes," *Journal of Engineering for Industry*, vol. 109, no. 1, pp. 49-57, 1987.
- [57] M. Pietrzyk and J. G. Lenard, "A study of heat transfer during flat rolling," *International journal for numerical methods in engineering*, vol. 30, no. 8, pp. 1459-1469, 1990.

- [58] C. O. Hlady, J. K. Brimacombe, I. V. Samarasekera, and E. B. Hawbolt, "Heat transfer in the hot rolling of metals," *Metallurgical and Materials Transactions B*, vol. 26, no. 5, pp. 1019-1027, 1995// 1995.
- [59] Z. Malinowski, J. G. Lenard, and M. E. Davies, "A study of the heat-transfer coefficient as a function of temperature and pressure," *Journal of materials processing technology*, vol. 41, no. 2, pp. 125-142, 1994.
- [60] K. Murata, "Heat Transfer Between Metals in Contact and Its Application to Protection of Rolls.(Synopsis)," *Trans. Iron Steel Inst. Jpn.*, vol. 24, no. 9, 1984.
- [61] N. Yukawa, Y. Nakashima, T. Ishiguro, and E. Abe, "Modeling of heat transfer coefficient of oxide scale in hot forging," *Procedia Engineering*, vol. 81, no. October, pp. 492-497, 2014.
- [62] R. W.L., *Cold rolling of steel*. M. Dekker, 1978.
- [63] J. G. Lenard, "The Effect of Temperature on the coefficient of friction in flat rolling," vol. 40, pp. 4-7, 1991.
- [64] Z. Wusatowski, *Fundamentals of Rolling*. Oxford University Press, 1960.
- [65] F. Wang and J. G. Lenard, "An Experimental Study of Interfacial Friction-Hot Ring Compression," *Journal of Engineering Materials and Technology*, vol. 114, no. 1, pp. 13-18, 1992.
- [66] G. W. Rowe, "An introduction to the principles of metalworking," 1965.
- [67] E. Siebel and W. Lueg, "Investigations Into the Distributions of Pressure at the Surface of the Material in Contact with the Rolls," *Mitt. KW Inst. Eigef.*, vol. 15, pp. 1-14, 1933.
- [68] F. A. R. Al-Salehi, T. C. Firbank, and P. R. Lancaster, "An experimental determination of the roll pressure distributions in cold rolling," *International Journal of Mechanical Sciences*, vol. 15, no. 9, pp. 693-710, 1973.
- [69] J. G. Lenard and Z. Malinowski, "Measurements of friction during the warm rolling of aluminum," *Journal of Materials Processing Technology*, vol. 39, no. 3, pp. 357-371, 1993/11/01 1993.
- [70] G. T. van Rooyen and W. A. Backofen, "A study of interface friction in plastic compression," *International Journal of Mechanical Sciences*, vol. 1, no. 1, pp. 1-27, 1960/01/01 1960.
- [71] J. G. Lenard, "Tribology in Metal Rolling Keynote Presentation Forming Group F," 1979.
- [72] L. Lai-Seng and J. G. Lenard, "Study of Friction in Cold Strip Rolling," *Journal of Engineering Materials and Technology*, vol. 106, no. 2, pp. 139-146, 1984.
- [73] Y. Hatamura and T. Yoneyama, "Measurement of Actual Stress and Temperature on the Roll Surface During Rolling : Measurement of Temperature and Heat Flux Distribution on the Roll Surface in Cold

- Rolling," *JSME international journal. Ser. 3, Vibration, control engineering, engineering for industry*, vol. 32, no. 4, pp. 676-680, 1989.
- [74] A. Mukhopadhyay, I. C. Howard, and C. M. Sellars, "Development and validation of a finite element model for hot rolling using ABAQUS/STANDARD," *Materials Science and Technology*, vol. 20, no. September, pp. 1123-1133, 2004.
- [75] K. Hara, H. Utsunomiya, R. Matsumoto, and T. Sakai, "Influence of scale on hot rolling characteristics of Si-bearing steel sheets," *Journal of Physics: Conference Series*, vol. 379, no. 1, p. 012043, 2012.
- [76] G. T. Van Rooyen and W. A. Backofen, "Friction in cold rolling," *J. Iron Steel Inst*, vol. 186, pp. 235-244, 1957.
- [77] C. Boldetti, C. Pinna, I. C. Howard, and Gutierrez, "Measurement of deformation gradients in hot rolling of AA3004 C," *Experimental Mechanics*, vol. 45, 2005.
- [78] A. T. Male and M. G. Cockcroft, "A method for the determination of the coefficient of friction of metals under conditions of bulk plastic deformation," *J. Inst. Of Metals*, vol. 93, no. 2, 1966/05/01 1964.
- [79] V. A. M. Cristino, P. A. R. Rosa, and P. A. F. Martins, "Surface roughness and material strength of tribo-pairs in ring compression tests," *Tribology International*, vol. 44, no. 2, pp. 134-143, 2// 2011.
- [80] P. A. R. Rosa and P. A. F. Martins, "The Role of Interfaces in the Evaluation of Friction by Ring Compression Testing," no. July, 2015.
- [81] F. Martín, M. J. Martín, L. Sevilla, and M. A. Sebastián, "The Ring Compression Test: Analysis of Dimensions and Canonical Geometry," *Procedia Engineering*, vol. 132, pp. 326-333, 2015/01/01 2015.
- [82] R. S. Hartley, T. J. Cloete, and G. N. Nurick, "An experimental assessment of friction effects in the split Hopkinson pressure bar using the ring compression test," *International Journal of Impact Engineering*, vol. 34, no. 10, pp. 1705-1728, 10// 2007.
- [83] Y. Zhu, W. Zeng, X. Ma, Q. Tai, Z. Li, and X. Li, "Determination of the friction factor of Ti-6Al-4V titanium alloy in hot forging by means of ring-compression test using FEM," *Tribology International*, vol. 44, no. 12, pp. 2074-2080, 11// 2011.
- [84] H. Sofuoglu, H. Gedikli, and J. Rasty, "Determination of Friction Coefficient by Employing the Ring," vol. 123, no. July, 2001.
- [85] E. Rajesh and M. Sivaprakash, "Analysis of friction factor by employing the ring compression test under different lubricants," vol. 4, no. 5, pp. 1163-1171, 2013.
- [86] C. Hu, H. Ou, and Z. Zhao, "An alternative evaluation method for friction condition in cold forging by ring with boss compression test," *Journal of Materials Processing Technology*, vol. 224, pp. 18-25, 10// 2015.

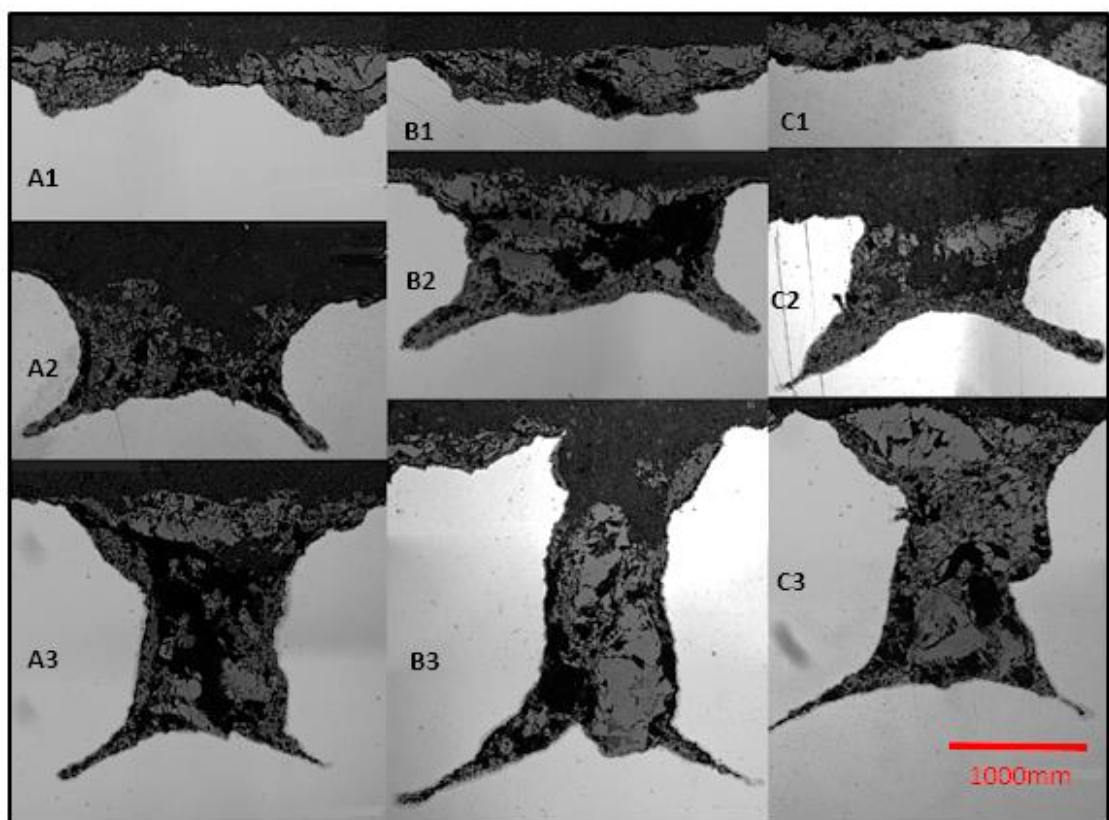


- [87] J. B. Hawkyard and W. Johnson, "An analysis of the changes in geometry of a short hollow cylinder during axial compression," *International Journal of Mechanical Sciences*, vol. 9, no. 4, pp. 163-182, 1967/04/01 1967.
- [88] K. Andersson, S. Kivivuori, and A. S. Korhonen, "Effect of the heat-transfer coefficient in ring-compression tests," *Journal of Materials Processing Technology*, vol. 62, no. 1, pp. 10-13, 1996/11/01 1996.
- [89] J. D. Pollard, A. Watford, and M. Jackson, "The Modelling Of Ring Tests At Elevated Temperatures For The Determination Of Friction In Ti-6Al-4V Forgings," vol. 15.
- [90] J. Paidassi, "The kinetics of the air oxidation of iron in the range 700-1250-degrees-C," *Acta Metallurgica*, vol. 6, no. 3, pp. 184-194, 1958.
- [91] S. Taniguchi, K. Yamamoto, D. Megumi, and T. Shibata, "Characteristics of scale/substrate interface area of Si-containing low-carbon steels at high temperatures," *Materials Science and Engineering: A*, vol. 308, no. 1-2, pp. 250-257, 6/30/ 2001.
- [92] E. M. Levin, C. R. Robbins, and H. F. McMurdie, "Phase diagrams for ceramists," 1974.
- [93] T. Amano *et al.*, "Hardness of oxide scales on Fe-Si alloys at room-and high-temperatures," vol. 522, pp. 469-476: Trans Tech Publ.
- [94] T. Fukagawa, H. Okada, and Y. Maehara, "Mechanism of Red Scale Defect Formation in Si-added Hot-rolled Steel Sheets," *ISIJ International*, vol. 34, no. 11, pp. 906-911, 1994.
- [95] D. Farrugia, A. Richardson, and Y. J. Lan, "Advancement in understanding of descalability during high pressure descaling," vol. 622, pp. 29-36: Trans Tech Publ.
- [96] N. J. Silk, "The practical aspects of hydraulic de-scaling," *Steel Times International*, vol. 25, no. 7, p. 38, 2001.
- [97] D. C. J. Farrugia and C. S. Fedorciuc-Onisa, Maurice, "Investigation into mechanisms of heat losses and mechanical descalability during high pressure water descaling," ed. Verlag Stahleisen MbH Sohnstrabe 65, D-40237, Dusseldorf, Germany: Steel research international, 2008, pp. 397-402.
- [98] P. Rodriguez-Calvillo, M. Perez-Sine, J. Schneider, H. Hermann, J. M. Cabrera, and R. Kawalla, "Effect of the Si and Al Content in Ferritic Electrical Steels on the Flow Behaviour and Dynamic Softening in Hot Rolling," *Materials Science Forum*, vol. 762, pp. 747-752, 2013.
- [99] C. M. Sellars and W. J. M. Tegart, "Hot Workability," *International Metallurgical Reviews*, vol. 17, no. 1, pp. 1-24, 1972.
- [100] "Abaqus, 6.13, Documentation manual," ed: Abaqus, 2013.

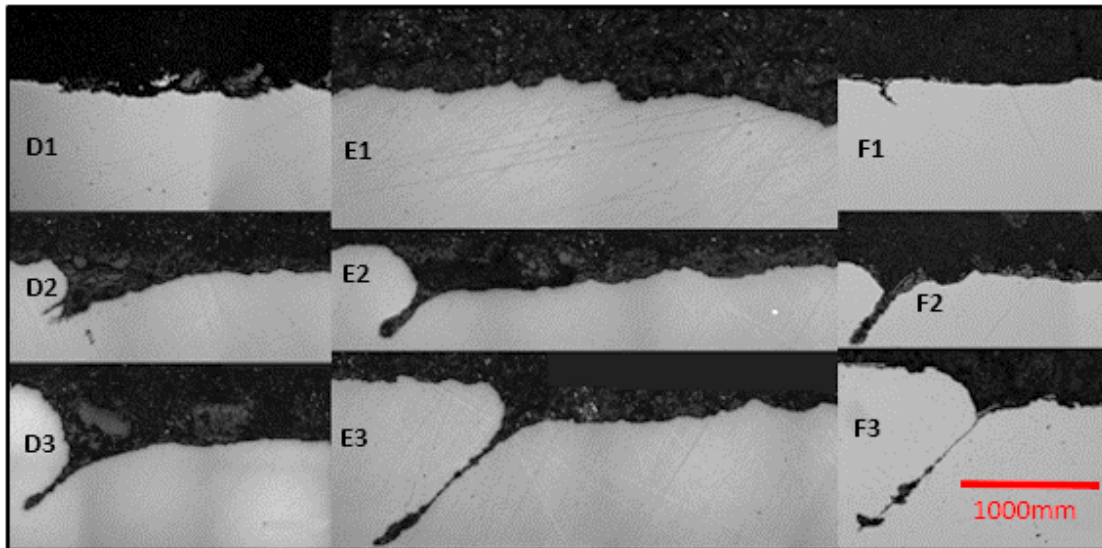
- [101] Lee S.-L and C. J., "Deformation analysis of surface defect on hot rolling by 3-D FEM simulation," *Revue de Metallurgie. Cahiers D'Informations Techniques*, vol. 105, no. 3, pp. 127-135+III-IV, 2008.
- [102] D. C. Montgomery, "Design and analysis of experiments," John Wiley & Sons, Inc, 2013.
- [103] R. Y. Chen and W. Y. D. Yuen, "Oxidation of low-carbon, low-silicon mild steel at 450-900°C under conditions relevant to hot-strip processing," *Oxidation of Metals*, Article vol. 57, no. 1-2, pp. 53-79, 2002.
- [104] H. Okada, T. Fukagawa, H. Ishihara, A. Okamoto, M. Azuma, and Y. Matsuda, "Prevention of red scale formation during hot rolling of steels," *ISIJ International*, Article vol. 35, no. 7, pp. 886-891, 1995.
- [105] H. Sofuoglu and J. Rasty, "On the measurement of friction coefficient utilizing the ring compression test," *Tribology International*, vol. 32, no. 6, pp. 327-335, 6// 1999.
- [106] W. L. Roberts, *Hot rolling of steel*. CRC Press, 1983.
- [107] O. Pawelski, W. Rasp, and C. Hoerster, "The ring compression test as simulation test for the investigation of friction in hot metal forming," *Steel Res.*, vol. 60, no. 9, pp. 395-402, 1989.
- [108] L. R. Underwood, *The rolling of metals: theory and experiment*. Chapman & Hall, 1950.
- [109] Z. Wusatowski, *Fundamentals of rolling*. Elsevier, 2013.
- [110] G. W. Rowe, "Principles of industrial metalworking processes," *Edward Arnold(Publishers) Ltd., 25 Hill St., London W 1 X 8 LL. 1977 Edition, 407 p(Book)*. 1977.
- [111] Pavlov.I.M. and Kuprin.S., *Sbornik XXXIII*. Moscow, 1955.
- [112] J. G. Lenard, "A study of the heat-transfer coefficient as a function of temperature and pressure," vol. 41, pp. 125-142, 1994.

**APPENDIX 1: Micrographs of the transversal section of the defects after rolling.**

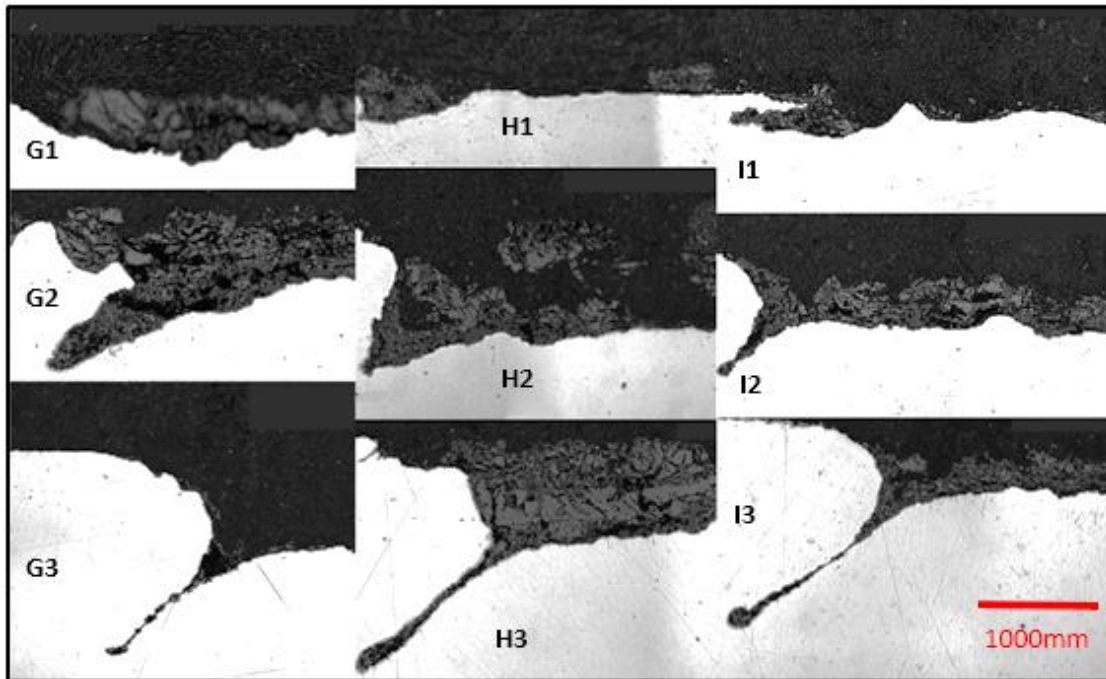
The transversal section of the defects after rolling is presented in Figure 0.1, Figure 0.2 and Figure 0.3 organised groups of different initial widths. Figure 0.1 presents the transversal section of all the defects with an initial width of 3mm, Figure 0.2 and Figure 0.3 present the transversal section of defects with an initial width of 11mm and 7mm respectively. Because of the wider dimension, only one side of the transversal section of the defect is presented in Figure 0.2 and Figure 0.3.



**Figure 0.1: Transversal section of the defect with an initial width of 3mm.**



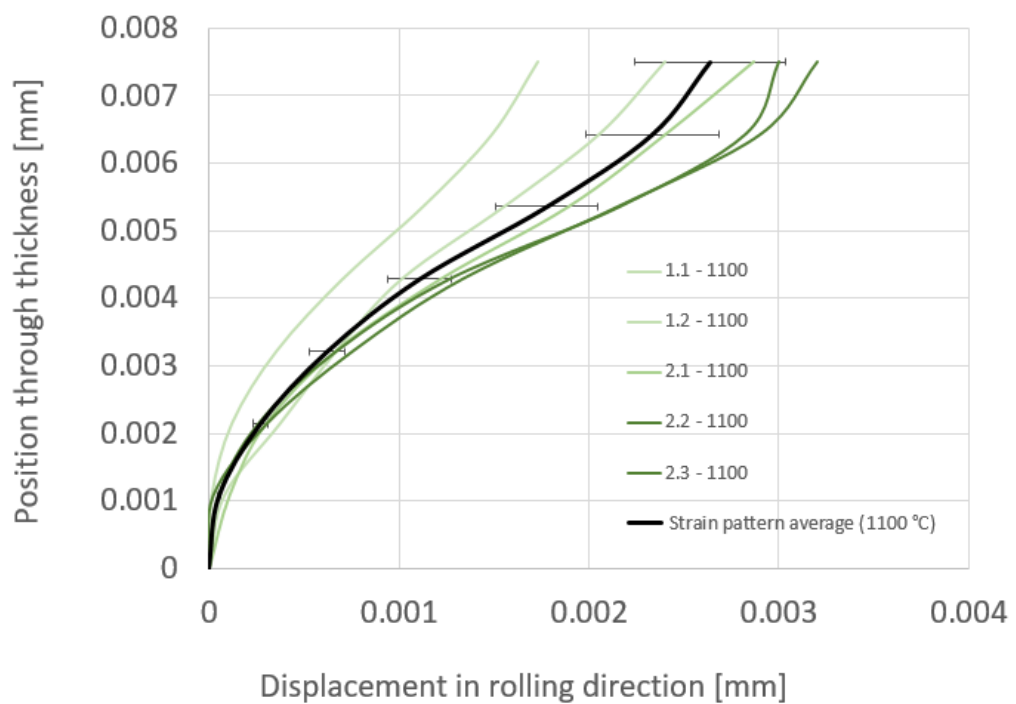
**Figure 0.2: Transversal section of the defect with an initial width of 11mm.**



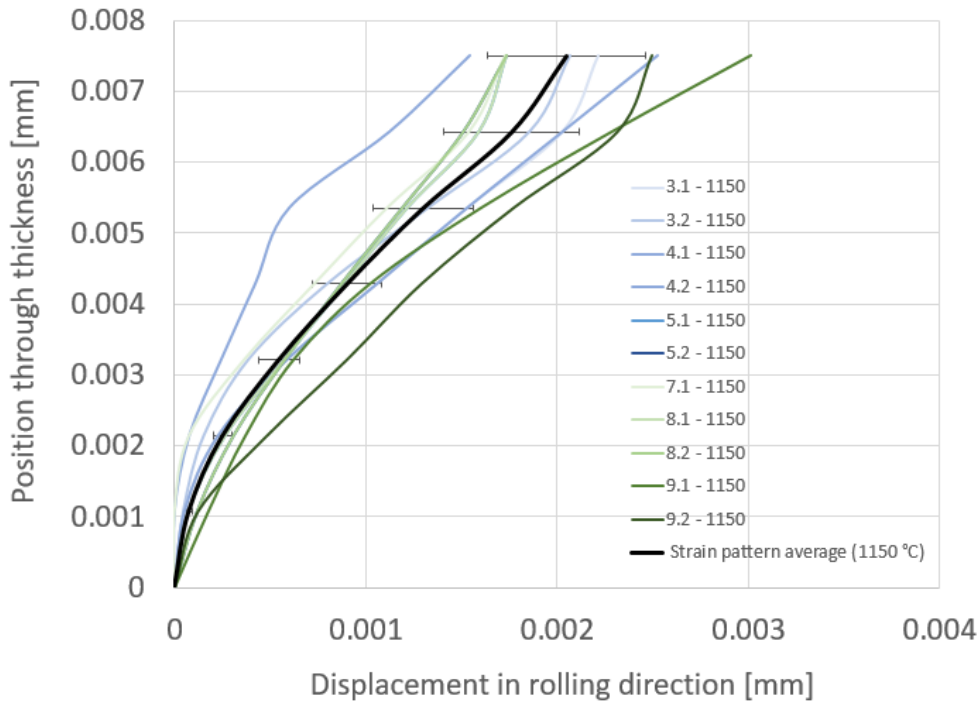
**Figure 0.3: Transversal section of the defect with an initial width of 7mm.**

## APPENDIX 2: Pin distortion measurements.

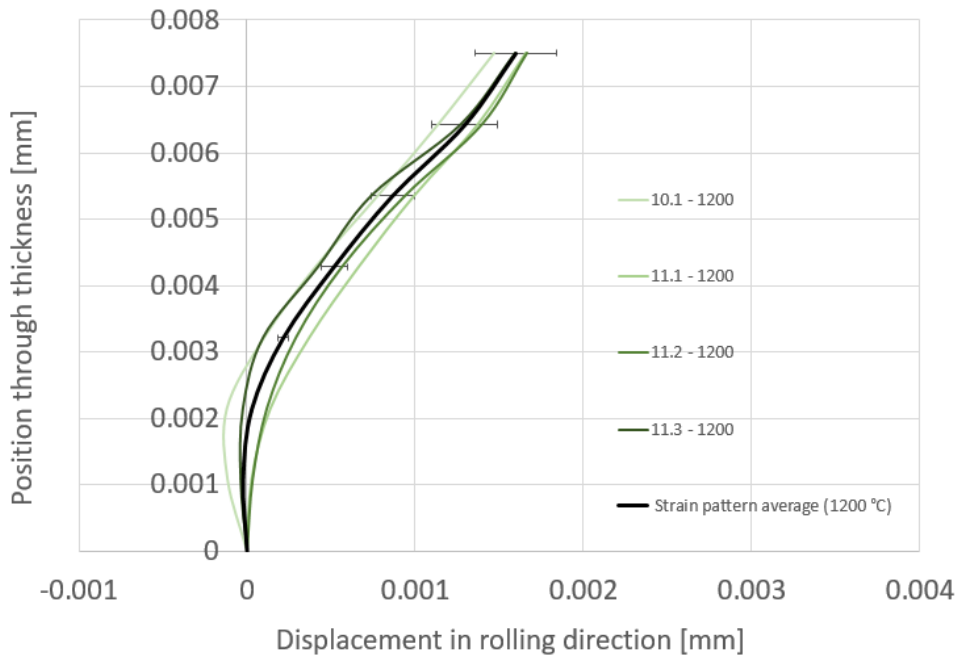
After the polishing of the samples, pins were inspected and measured, Figure 0.4, Figure 0.5 and Figure 0.6 represent the pin distortion pattern for slabs heated at 1100°C, 1150°C and 1200°C respectively. Each pin presented is indicated with two numbers, the first number indicates the slab code, the second number indicates the pin number. For example, the code 9.2 indicates the pin number 2 of the slab number 9.



**Figure 0.4: Pin distortion pattern for slabs heated at 1100°C for different slabs and pins.**



**Figure 0.5: Pin distortion pattern for slabs heated at 1150°C for different slabs and pins.**



**Figure 0.6: Pin distortion pattern for slabs heated at 1200°C for different slabs and pins.**